A novel method for electron energy measurement: Cyclotron Radiation Emission Spectroscopy

Jared Kofron

A dissertation
submitted in partial fulfillment of the
requirements for the degree of

Doctor of Philosophy

University of Washington

2015

Reading Committee:

R.G. Hamish Robertson, Chair

Leslie J Rosenberg

Gray A. Rybka

Program Authorized to Offer Degree:
Department of Physics

University of Washington

Abstract

A novel method for electron energy measurement:
Cyclotron Radiation Emission Spectroscopy

Jared Kofron

Chair of the Supervisory Committee:
Doctor R.G. Hamish Robertson
Department of Physics

A prototype spectrometer - the first of its kind - has been constructed at the University of Washington to demonstrate a new technique for β-decay studies called Cyclotron Radiation Emission Spectroscopy (CRES). The conversion spectrum of ^{83m}Kr has been measured to a precision of 25 eV. Conclusive observation of the K, L, M, and N series electrons demonstrates the range and generality of the technique. Future upgrades to the prototype are suggested, with an outlook toward a detector resolution of 1 eV.

TABLE OF CONTENTS

LIST OF FIGURES

: Vectors are denoted by bold face type instead of arrows. For example, $\mathbf{a}$ instead of $\vec{a}$.

: In lieu of the usual cross product notation $\vec{a} \times \vec{b}$, I use a wedge as in $\mathbf{a} \wedge \mathbf{b}$.

: Kinetic energy is denoted K to avoid confusion with T. An alternate title for this thesis would be "A study in irony: T is the most useful letter, but in practice you can't use it because it's also the most used".

: For consistency, all frequencies are given in Hz. The angular frequency ω is not used.

: The boosted cyclotron frequency is denoted f_c. The zero-energy limit of the cyclotron frequency is f_0 in all cases.

DEDICATION

For my parents and my family. You raised me to be analytical, to be a critical thinker, and above all to be a member of a community. Without your bottomless love and endless support none of this would be possible.

For my grandmother. Thanks for all the dead bugs in the mail when I was a kid. You stoked the fire of curiosity underneath me, and helped me to become who I am today.

For my grandfather, who set an example of excellence and grit that I always admired.

For Jean. You are a wellspring of love, understanding, and nurturing. You were my rock while I was writing this thesis. I couldn't have done it without you.

For the Lerners. You have encouraged and loved me from day one, literally.

For my friends. Thanks for always being there.

ACKNOWLEDGMENTS

A great number of people have been instrumental in making this research productive and successful - this is my humble attempt to thank them all adequately, which is a task perhaps even more daunting than this document itself.

First, I must gratefully acknowledge Hamish Robertson, my advisor, for his enormous and irreplacable role in shaping my graduate career. I could not have asked for a better scientist, mentor, and friend during my time at the University of Washington. Without his brilliant insight, endless encouragement, and effortless support, this document and the research it contains would be entirely impossible - and for that I am eternally grateful.

I would also be remiss if I did not thank Gray Rybka from the bottom of my heart - his patience and willingness to share his wisdom are always exemplary, and he is as good a companion after work as he is a coworker in the lab.

Ben LaRoque, my spiritual successor and carrier of the slow control torch - I have always been impressed with your grit. I wish you the best of luck in the future and have no doubt that you will succeed at your task.

Matt Sternberg and Martin Fertl have been great coworkers as well as role models for me. I thank you both for your help, your counsel, and your example. Also, Martin, I will always remember that you cleared that desk off in your office for me to work at.

Peter Hirtle, Jim Greenwell, and Ron Musgrave in the UW Physics Machine Shop were enormously helpful. Without their craftsmanship and expertise, I would not have been able

to build Project 8.

I would also like to thank the entire CENPA staff, from the administrators to the electronics shop. You provide a nurturing and supportive atmosphere without which the department simply would not be what it is.

Chapter 1

INTRODUCTION

1.1 The problem of β-decay

In the early 20^{th} century, a great many scientists had turned their attention to the newly discovered phenomenon of radioactivity - the spontaneous emission of free particles by atomic nuclei. Three known types of radiation existed, and were categorized according to the amount of material required to stop the emitted particles. α radiation was stopped by even thin sheets of material, β radiation required somewhat more, and γ radiation required a great deal of shielding to stop. The theory of the nucleus at the time included the quantization of energy levels in the nucleus - a theory which was borne out by experimental results which showed that the energies of α and γ particles were monoenergetic for a given nuclear transition.

In 1914, Chadwick discovered using a magnetic spectrometer that the energy spectrum of β particles was in fact not discrete, but continuous. The observed spectrum spanned the range from a kinetic energy of nearly zero up to the so-called "endpoint" energy E_0, equal to the energy difference between the excited nuclear states which gave rise to the radioactivity. The scientific consensus, spearheaded by Lise Meitner, was that a discretized nuclear energy spectrum could not give rise to the observed continuous energy spectrum of daughter particles. It was suggested that experimental error was to blame, and that energy loss processes must be accountable for the difference - after all, it was well known that the penetrating power of β particles was small compared to γ radiation.

Unmoved by this explanation, Ellis and Wooster constructed an experiment designed to measure the *total* energy output of a radioactive sample of known activity[20]. The experiment consisted of a very thick shield of lead surrounding a radioactive sample of the isotope

^{210}Bi (known at the time as "Radium E") with a precisely calibrated activity. The design, which would now be called a bomb calorimeter, was such that the temperature of the lead shielding could be monitored accurately and the *total* energy liberated from the nucleus per unit time thereby measured. Their conclusion was dramatic: despite the known ^{210}Bi endpoint energy of 1.05 MeV, the average energy per disintegration was only 390 keV.

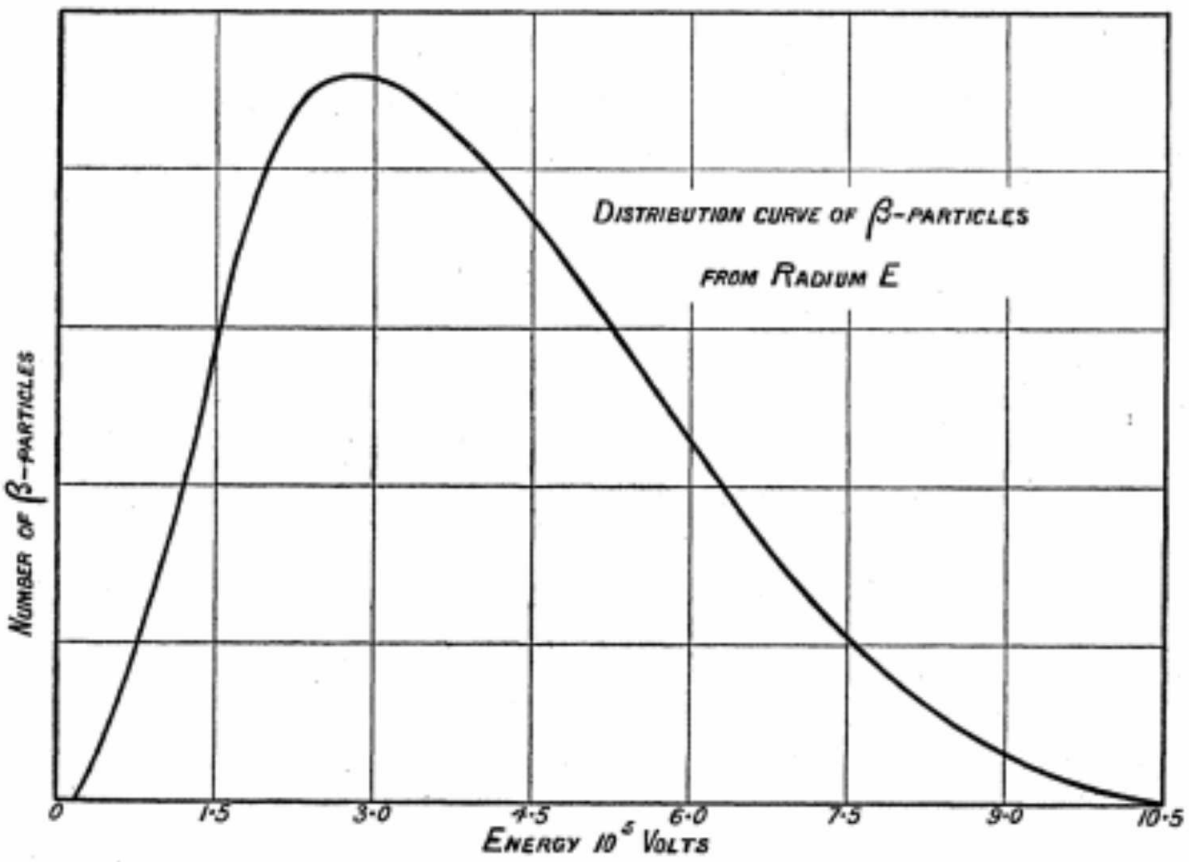

Figure 1.1: The β-decay spectrum as presented [19] by Ellis and Wooster in 1927.

In another development, both ^{6}Li and ^{14}N were observed to obey Bose statistics, in disagreement with the spin $\frac{1}{2}$ prediction from Rutherford's model of the nucleus as being composed of protons and electrons [39]. At this point, with the evidence mounting, the situation for β-decay was dire. Indeed, some prominent scientists began to question (even

Bethe!) the very idea that energy and angular momentum should be conserved in β-decay as a possible explanation[22]. Wolfgang Pauli, echoing the spirit of the time, penned a famous letter in 1930 in which he proposed a "desperate remedy" - he postulated the existence of a new particle[37] which could restore sanity to β-decay.

Pauli called this new particle the *neutron*, and postulated that it should be very light (perhaps even massless) and electrically neutral - so as to escape detection - and should carry spin 1/2. If the model of β-decay were altered so that a neutron was emitted along with an electron in every β-decay, then both spin statistics and energy conservation could be salvaged. This idea was greeted with deep skepticism[1] - at the time, the only known particles were the proton, the electron, and the photon. Indeed, the neutral particle that would permanently take the name *neutron* was not discovered until 1932 [12], despite being a constituent particle of the nucleus under such intense scrutiny. When Enrico Fermi submitted a manuscript to Nature in the year 1934[46], showing that the now accepted continuous energy spectrum of β-decay was predicted by Pauli's theory, it was rejected on the grounds that it was "too remote from reality"[13].

Now, the neutrinos and antineutrinos have become commonplace - a central pillar in our understanding of nature and first class citizens of the Standard Model of Particle Physics. Countless experiments have been performed to determine their properties and probe the consequences of their existence, but a conundrum observed in Fermi's original paper persists to this day.

1.1.1 Neutrino Mass

Fermi[46] deduced the functional form of the energy distribution for β-decay in terms of the mass μ of the neutrino, which he took to be a free parameter. As he noted in his seminal paper, if the mass of the neutrino is not identically zero, the phase space which is available to the outgoing β particle is modified to account for the rest mass of the neutrino. Naturally,

[1] Perhaps even by Pauli himself, although perhaps his use of the word "desperate" truly reflects the caution of a great scientist.

this effect is most pronounced near the endpoint of the spectrum, where the neutrino is emitted nearly at rest and the energy of the outgoing electron takes its maximum value of $E_{\max} = E_{\text{trans}} - m_e - m_\nu$, with E_{trans} equal to the energy difference between the nuclear states involved in the decay. In particular, in the event that a neutrino should have non-zero rest mass, the endpoint of the β-decay spectrum is altered by a shift in energy precisely equal to m_ν. Experimental evidence from β-decay spectroscopy was (and is) in excellent agreement with the hypothesis that m_ν is precisely zero.

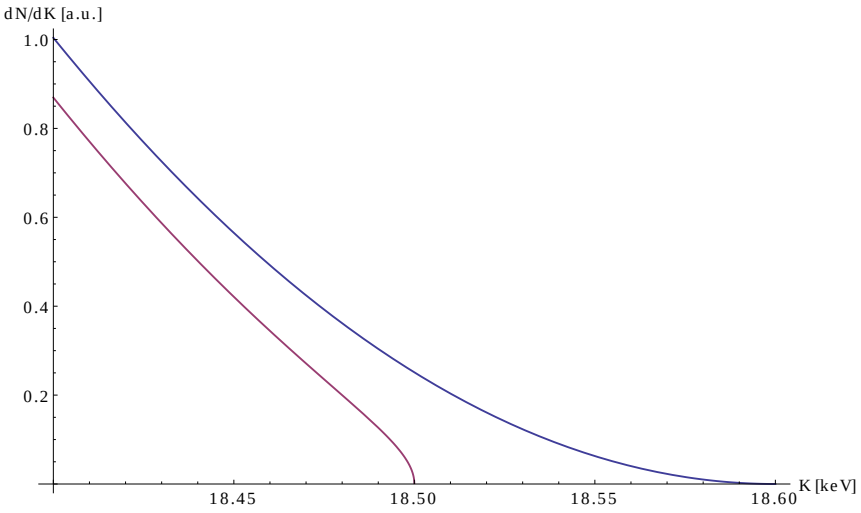

Figure 1.2: The effect of a massive neutrino on the β decay spectrum near the endpoint of ^{3}H. Shown in red is the observed spectrum for a (very) massive neutrino of $m_\nu \approx 100\,\text{eV}$. Note that the endpoint changes from 18.6 keV to 18.5 eV, and additionally the shape of the spectrum is different.

The case for a massless neutrino was bolstered in 1958 in a fantastic experiment by Goldhaber et al[26], in which it was demonstrated that neutrinos are particles of definite helicity. For neutrinos to satisfy this property, they must be of exactly zero mass - otherwise it is always possible to find a frame which is moving faster than the neutrino. In such a frame, $p \to -p$, but σ does not change, so that under this transformation the helicity of the particle changes sign and is therefore cannot be invariant. While this property is strictly speaking only true for relativistic neutrinos, this seeming contradiction was nonetheless a

source of great confusion.

Experiments probing the composition of neutrinos emitted from the core of the sun, as well as from nuclear reactors and accelerators, have demonstrated beyond a doubt that the mass of the neutrino cannot possibly be exactly zero. The eigenstates $\nu_{e,\mu,\tau}$ that diagonalize the weak interaction are not the same as the eigenstates that describe the propagation of free neutrinos $\nu_{1,2,3}$, and as a consequence neutrino interactions may violate lepton family number conservation over sufficiently long distance scales - a phenomenon known as neutrino oscillations. This phenomenon is strictly forbidden for massless neutrinos, providing definitive evidence for their nonzero mass. The "oscillation bound", which may be obtained from measured values of $\delta_{i,j} = m_i^2 - m_j^2$ and the fact that m_i^2 is positive definite, provides a definite lower bound[33] of $\langle m_i \rangle \geq 20\,\mathrm{meV}$.

Cosmological observations[25] have also placed a (strongly model dependent) bound on the sum of neutrino masses: $\sum m_i \leq 0.39\,\mathrm{eV}$. While both of these limits are scientifically both meaningful and well motivated, they still do not comprise a *direct* measurement of the mass of the neutrino. Oscillation experiments can only measure squared differences, $\Delta m_{ij}^2 = m_i^2 - m_j^2$. The cosmological bounds are predicated upon the effect of neutrino densities on the clumping of galaxies and large-scale structure in the universe, and therefore can only measure the *sum* of the neutrino mass eigenstates in a highly model dependent fashion. These limits therefore constitute a measure of the possible *scale* of the neutrino masses, which must be distinguished from a measurement of m_ν.

Hereafter, the "neutrino mass" will refer to the incoherent sum over neutrino mass eigenstates, appropriately weighted by the PMNS (Pontecorvo-Maki-Nakagawa-Sakata) matrix U_{ij} which describes the relationship between the mass and flavor eigenstates:

$$m_\beta = \sqrt{\sum_i |U_{ei}|^2 \, m_i^2} \tag{1.1}$$

Where m_i is the mass of the i^{th} mass eigenstate, and m_β is the parameter which appears in the expression for the phase space in β-decay. The value of this parameter is quite small,

and therefore the corresponding phase space distortion is extremely difficult to detect. In the most optimistic case, according to our present understanding the endpoint energy will be only 0.39 eV different from the massless case, which is a very small difference indeed - less than 1ppm of the mass of the electron.

1.2 State of the art spectrometers

The family of spectrometers which are currently considered the state of the art are the MAC-E (Magnetic Adiabatic Collimation - Electrostatic) type which has been successfully utilized in experiments such as those at Mainz and Troitsk. The MAC-E spectrometer (as shown below in Figure 1.2) relies on the fact that the magnetic moment $\mu = v_\perp^2/2B$ of an electron in a magnetic field is a conserved quantity[34], and therefore the transverse energy of the electron is proportional to B. By adiabatically transporting electrons from a high field region to a low field region, the transverse energy of the electron may be converted to longitudinal energy[2]. An electrostatic potential that is maximal at the plane where the magnetic field is a minimum then repels particles for which $T < eU$, creating a high-pass filter for electron kinetic energies. The electrons are then magnetically re-focused onto a detector for counting. Because the discriminating apparatus is a high-pass filter, the spectrum which is measured is the integral of the β-decay spectrum.

The Mainz experiment used as its source of β-decay electrons a thin film of molecular tritium $^3H_2$ cryopumped onto a graphite substrate. While multiple settings were chosen for different runs, the resolution of the spectrometer was about 4 eV on average ($B_a/B_s = 2.56 \times 10^{-4}$) at an analyzing potential of $U = 18\,690$ V. In 2005 the final results from the second phase of the Mainz experiments were published [30] and a neutrino mass bound obtained of $m(\nu_e) \leq 2.2\,\mathrm{eV/c^2}$(95%C.L.).

[2]This is the opposite of the magnetic mirror effect, in which the longitudinal energy of the particle is converted to transverse energy to restrict the motion of a particle along the direction of the inhomogenous field.

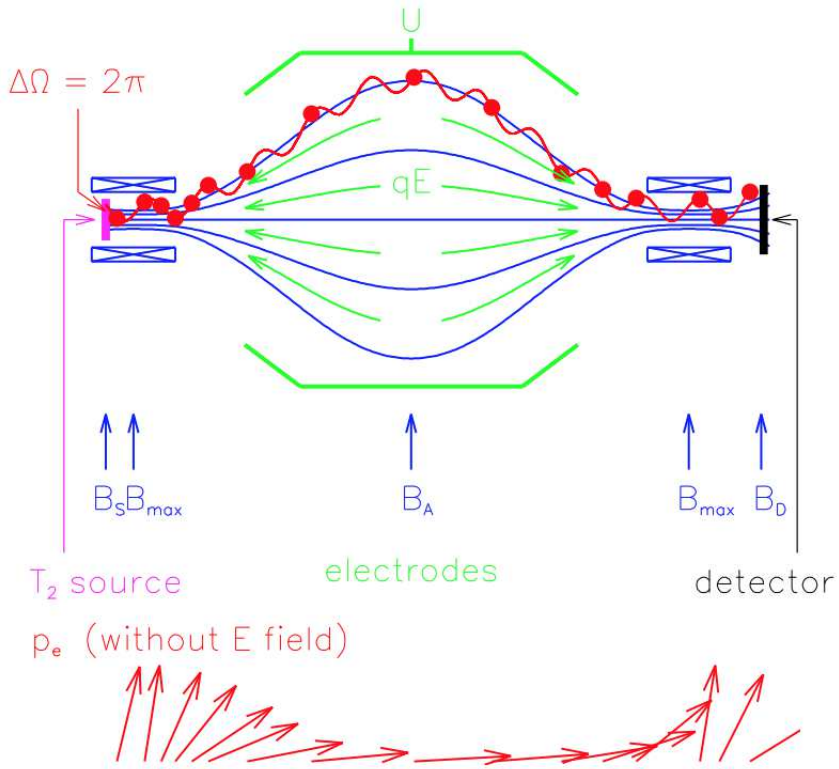

Figure 1.3: The principle of operation of a MAC-E type electron spectrometer. Electrons that are admitted to the spectrometer at the left hand side are adiabatically transported through a region of low magnetic field at the midplane of the vessel. At the midplane, an analyzing potential U reflects electrons that have a kinetic energy less than eU, thereby creating a high-pass filter[18].

The Troitsk experiment was also based on a MAC-E spectrometer, but utilized a different source design. Originally pioneered in the LANL tritum β-decay experiments, the Windowless Gaseous Tritium Source (WGTS) has no substrate on which the source resides. As a consequence, systematic errors due to solid state effects and interactions between outgoing electrons and the substrate are eliminated. A combined analysis[3] of the data from the Troitsk experiment taken between the years 1994 and 2004 yields an upper bound comparable to the Mainz result of $m(\nu_e) < 2.05\,\mathrm{eV}(95\%\mathrm{C.L.})$.

An improvement of roughly one order of magnitude over these limits is expected from the upcoming KATRIN experiment[47], with an ultimate spectrometer resolution of 0.93 eV and a corresponding sensitivity to $m(\nu_e)$ of 0.2 $\mathrm{eV/c^2}$ expected after 3 years.

In 2009, a suggestion was made to the Physics community by Monreal and Formaggio [32] that the dynamics of an electron in a magnetic field could be used to develop a spectroscopic technique with entirely different systematics from the electrostatic spectrometers, and with the potential for improved resolution as well. A motivation of this method is below, beginning with a consideration of the effect of special relativity on charged particle motion in a magnetic field.

1.3 Relativistic cyclotron motion

The relativistic equation of motion for an electron in a constant, uniform magnetic field $\mathbf{B}$ is given by the usual Lorentz force law:

$$\frac{d\mathbf{p}}{dt} = e\mathbf{v} \wedge \mathbf{B} \tag{1.2}$$

Where $\mathbf{p}$ is the relativistic momentum $\mathbf{p} = \gamma m\mathbf{v}$. Because there is no electric field present and the magnetic field may do no work, the magnitude of $\mathbf{v}$ must remain constant[3], as will γ. Therefore, we may collect terms on the right hand side of Equation 1.2:

$$\begin{aligned}\dot{\mathbf{v}} &= \mathbf{v} \wedge \left(\frac{e\mathbf{B}}{\gamma m}\right) \\ &= \mathbf{v} \wedge \omega_c \hat{\mathbf{B}}\end{aligned}$$

As we shall see shortly, the term $\omega_\mathbf{c}$ may be identified with the relativistic form of the familiar cyclotron frequency.

Take $\hat{\epsilon_\mathbf{3}}$ be the direction of the magnetic field, such that $v_3 = \mathbf{v} \cdot \hat{\epsilon_\mathbf{3}}$ is the component of the velocity along the direction of the field. Then it may be shown that the equations of

[3]Neglecting losses due to radiation, which will be treated subsequently.

motion 1.2 reduce to:

$$\mathbf{v_1} = ve^{-i\omega_c t}\hat{\epsilon_1} \tag{1.3}$$

$$\mathbf{v_2} = -ive^{-i\omega_c t}\hat{\epsilon_2} \tag{1.4}$$

So that we can write:

$$\mathbf{v}\left(t\right) = v_{\parallel}\hat{\epsilon_3} + \omega_c r_c\left(\hat{\epsilon_1} - i\hat{\epsilon_2}\right)e^{-i\omega_c t} \tag{1.5}$$

In the usual Cartesian coordinates, where $\epsilon_{1,2,3}$ correspond to $\hat{\mathbf{x}}$, $\hat{\mathbf{y}}$, and $\hat{\mathbf{z}}$, we see that the motion in the plane normal to the magnetic field is circular, with the frequency of the motion in the $\hat{\epsilon_1}$, $\hat{\epsilon_2}$ plane equal to precisely:

$$f_c = \frac{1}{2\pi}\omega_c = \frac{1}{2\pi}\frac{eB}{\gamma m} \tag{1.6}$$

with the most general motion being a helical path for $v_3 \neq 0$.

1.3.1 Radiation

The form of Equation 1.5 makes it clear that the acceleration of the electron is nontrivial. As will any accelerated charge, an electron in cyclotron motion radiates power in the form of electromagnetic radiation. The total electromagnetic power radiated by a relativistic accelerated charge may be obtained from a result by Lienard[28]:

$$P = \frac{e^2}{6\pi\epsilon_0 c}\gamma^6\left[(\dot{\beta})^2 - (\beta \wedge \dot{\beta})^2\right]$$

For the motion described by Equation 1.5, the exact solution is given by

$$P\left(\gamma,\theta\right) = \frac{1}{6\pi\epsilon_0}\frac{e^4}{m_e^2 c}B^2\left(\gamma^2 - 1\right)\sin^2\theta \tag{1.7}$$

Where $\theta = \tan^{-1}v_{\perp}/v_{\parallel}$ is the pitch angle of the electron w.r.t the magnetic field.

1.4 Cyclotron Radiation Emission Spectroscopy

The results of the previous section may be distilled into a series of observations regarding the radiation emitted by an electron undergoing cyclotron motion.

- The cyclotron frequency of an electron as derived in Equation 1.5 is independent of its pitch angle. This is a crucial point - if this was not the case, a measurement of the cyclotron frequency would not be an independent measure of energy.

- When relativistic effects are considered, the cyclotron frequency of an electron is not independent of its energy, but instead is modified by a factor of γ^{-1}.

- The total power radiated by such an electron scales with the square of the magnetic field strength B.

- As the Lorentz boost factor approaches 1, the total power radiated decreases as $\left(\gamma^2 - 1\right)$.

The above considerations form the basis for a novel spectrometric technique for mildly relativistic electrons.

Let us first consider the contrived case in which energy loss is exactly zero, so that the cyclotron frequency of the electron is a constant of the motion. Let f_0 be the zero energy limit of the cyclotron frequency f_c, $f_0 = (2\pi)^{-1}eB/m_e$, and take K to be the kinetic energy of the electron in question. Then

$$\begin{aligned} \frac{\omega_0}{\omega_c} = \frac{f_0}{f_c} =& \gamma = 1 + \frac{K}{m_e c^2} \\ & \therefore K = m_e c^2 \left(\frac{f_0}{f_c} - 1 \right) \end{aligned} \tag{1.8}$$

Consequently, if the magnetic field strength B is known exactly, a measurement of f_c may be used to obtain the kinetic energy of an electron up to the uncertainty in a combination of the fundamental constants m_e, c, and e.

Under the assumption that the only energy loss mechanism is cyclotron radiation, the cyclotron frequency of the electron will become explicitly time dependent, and evolves according to the total cyclotron power loss P_c. An expression for the time derivative of f_c

may be obtained straightforwardly:

$$\dot{f}_c(t) = \frac{df_c}{dt} = \frac{df_c}{dK}\frac{dK}{dt} = \frac{f_c}{2\pi\gamma m_e c^2} \cdot P_c \tag{1.9}$$

Where we have identified $\dot{K}$ as equal and opposite to the loss in energy due to cyclotron radiation. If only the instantaneous kinetic energy of the electron is of interest, no modification need be made to the expression in Equation 1.8. On the other hand, should the initial kinetic energy be the object (as in a β-decay spectrum measurement), the expression is still correct in the case of nonzero energy loss if the substitution $f_c \to f_c|_{t=0}$ is made.

The essential substance of cyclotron radiation spectrometry is now plain. If the cyclotron frequency of a relativistic electron in a magnetic field can be measured accurately and precisely, then the kinetic energy of that electron can also be measured. Naturally, factors arise which confound such a measurement, and many questions of fundamental import have been neglected which will be addressed. However, it is worthwhile to address the (perhaps most) basic question of feasibility before tackling the more difficult technical issues.

1.5 On feasibility

It is reasonable to suspect that some fundamental aspect of the measurement technique which is suggested in the above discussion may be fatally flawed. In fact, previous authors familiar with the science of observing the dynamics of trapped electrons have suggested that a direct observation of the cyclotron radiation from a single electron may be too difficult to pursue[9]. The technique of measuring K via a measurement of f_c, called Cyclotron Radiation Emission Spectrometry (hereafter CRES) may be reduced on its face to a single goal:

The initial kinetic energy of an electron is to be inferred via a measurement of its cyclotron frequency at the moment it enters (or is created in) a known magnetic field.

1.5.1 Emitted power

Let us first consider the question of the detection of electromagnetic power radiated by an electron in cyclotron motion. If the total power emitted by the electron is below the threshold of detection, a CRES measurement of its kinetic energy is infeasible. If the magnetic field is taken to be 1 T, and an electron energy which is comparable to the endpoint energy for ^{3}H of kinetic energy 20 keV, the total power emitted into free space as calculated from Equation 1.7 is roughly 1.2 fW. By way of comparison, consider the fact that a typical received power in a terrestrial Global Positioning System (GPS) antenna is about 200 aW - almost a full order of magnitude smaller.

However encouraging, the signal power taken by itself is not meaningful - we must also understand the noise performance of the system so that we can estimate the achievable signal-to-noise ratio ($\mathcal{S}$). In the Rayleigh-Jeans approximation to the Boltzmann blackbody distribution, the total thermal noise power scales simply with the frequency interval (bandwidth) $\nu = f_{\max} - f_{\min}$ in question: $P_n = k_B T \nu$. Therefore, to make a statement about the achievable $\mathcal{S}$, it is necessary to first understand the bandwidth of the signal we wish to observe.

1.5.2 Bandwidth, resolution and observation time

Existing state of the art electron spectrometers such as the MAC-E (Magnetic Adiabatic Collimating Electrostatic) type employed by the KATRIN experiment are able to achieve an energy resolution of about 1 eV. Because the energy measurement that is performed in a CRES experiment is actually derived from a measurement of frequency, the necessary frequency resolution which is required for a CRES experiment to be competitive with a traditional spectrometer is a parameter of interest.

Recall the expression for the kinetic energy K of an electron given a measurement of its relativistic cyclotron frequency f_c:

$$K = m_e c^2 \left(\frac{f_0}{f_c} - 1 \right) \tag{1.10}$$

Assume for the present argument that the magnetic field is known exactly, or at least that the uncertainty in the magnetic field is entirely negligible. Then computing the statistical uncertainty on the kinetic energy is straightforward:

$$\begin{aligned}\sigma_T =& \left| \left(\frac{\partial K}{\partial \omega_\gamma} \right) \sigma_{\omega_\gamma} \right| \\ =& \sigma_{\omega_\gamma} \cdot m_e c^2 \frac{\omega_0}{\omega_\gamma^2} \\ =& \frac{\sigma_{\omega_\gamma}}{\omega_\gamma} \left(K + m_e c^2 \right) \\ =& \gamma m_e c^2 \frac{\sigma_{\omega_\gamma}}{\omega_\gamma} \end{aligned} \tag{1.11}$$

To compete with the 1 eV resolution of the MAC-E spectrometer at an electron energy of 20 keV, the necessary (fractional) frequency uncertainty is $\sigma_{f_c}/f_c \approx 2 \times 10^{-6}$. If the magnetic field is 1 T, then $f_c\,(K = 20\,\text{keV}) \approx 26\,\text{GHz}$, and the necessary frequency uncertainty is 50 kHz. Compared to modern frequency measurements which are routinely performed to a part in 10^{12}, this is an entirely undaunting requirement.

How does this requirement on frequency uncertainty inform the design of a possible CRES experiment? Early work on communication theory led to the discovery of a time-frequency uncertainty principle[24] in exact correspondence to that derived from considering the canonical commutation relations[4] in quantum mechanics:

$$\Delta t \Delta f \geq \frac{1}{4\pi} \tag{1.12}$$

This uncertainty relation implies that if we wish to localize the cyclotron frequency of our electron to an interval of size $\Delta f \approx 50\,\text{kHz}$, we must observe it for an interval of time that is no less than 2 µs.

This somewhat simplistic view of the issue neglects the fact that due to energy loss, f_c is *changing* with time. A more thorough treatment will appear below, but to soothe this

[4]The astute reader will recall that there is a minimum-uncertainty wavepacket in quantum mechanics, and wonder at this point about a minimum-uncertainty signal. It indeed does exist in the form of a wavepacket-like object which Gabor called a logon [24]. It is simply a wavepacket in another form.

concern we may satisfy ourselves with a simple argument. If we seek only to localize f_c to a frequency bin 50 kHz wide, it is then sufficient to ensure that power loss will not change its frequency by more than the width of the bin in the observation time which is required to establish that width:

$$\frac{1}{2\pi}\frac{df_c}{dt}\cdot\Delta t < 50\,\mathrm{kHz}$$

At a field strength of 1 T, $\dot{f}_c$ as derived in Equation 1.9 is approximately $300\,\mathrm{Hz\,\mu s^{-1}}$, and therefore our constraint is handily satisfied with a safety factor of almost two orders of magnitude.

1.5.3 Signal to noise

Any electronic component adds noise power to the signal at its input. A convenient parameterization of this added noise is in terms of the so-called "noise temperature" of the component, which is defined as the temperature of a matched resistor which would deliver the same noise[5]. If a blackbody source of noise at temperature T_r is matched to the input of an amplifier with noise temperature T_a, then the output noise power will be equal to $k_B G\nu\,(T_r + T_a)$, where k_B is Boltzmann's constant, and ν is the bandwidth under consideration[6]. We can therefore determine the maximum achievable SNR $\mathcal{S}$ for a given system of noise temperature T_r:

$$\mathcal{S} = \frac{P_c}{k_B \nu T_r} \tag{1.13}$$

A perhaps more convenient parameterization for the current discussion eliminates the bandwidth in favor of the total radiated energy of the electron. It is clear from the expression above that the minimum possible bandwidth is desirable from an experimental standpoint because the resulting $\mathcal{S}$ is maximized. The bandwidth is related in a simple manner to the total observation time - $\mathcal{S} = \mathcal{T}_{\mathrm{obs}}^{-1}$. In that amount of time, the electron will radiate a total energy that is equal simply to $E_{\mathrm{rad}} = P_c \mathcal{T}_{obs}$. Rearranging Equation 1.13 in favor of the

[5]The noise temperature of a component, while in general depending on the physical temperature, may be wildly different from its actual temperature T

[6]Stated alternatively, a real amplifier with noise temperature T_a contributes $k_B T$ $\mathrm{W\,Hz^{-1}}$ of real noise power to its output.

total radiated energy, we see that $\mathcal{T}_{\text{obs}}$ is eliminated and $\mathcal{S}$ may instead be written as:

$$\mathcal{S} = \frac{E_{rad}}{k_B T_r} \tag{1.14}$$

Where E is the total energy radiated by the electron during the period of observation[7]. Conservatively demanding a $\mathcal{S} \geq 10$, we require that our receiving device have a noise temperature no greater than 16 K if electrons are trapped on average for only 2 µs. Even this level of stringency is achievable - amplifiers are available commercially that have a noise temperature of 11 K.

1.5.4 Observation time

In the 2 µs that is required for a precision frequency measurement, a cyclotron electron with a pitch angle of $\pi/2 - 1°$ will travel a distance along the z axis of almost 3 m. To make such a measurement, then, the electrons must be confined in some way. Because the object of a CRES experiment is to measure precisely the energy of the electrons in question, clearly any configuration of trapping potentials that alters the energy of the electron is unacceptable. Therefore the familiar Penning-type traps which utilize an electric field to confine charged particles may not be employed, and instead we must rely on purely magnetic means to restrict the motion of the particles. As magnetic fields may do no work, we are guaranteed that the kinetic energy of the particle will not be changed by the action of a magnetic trapping potential.

Let us consider the Hamiltonian for an electron in helical motion which finds itself in a non time-varying purely magnetic field (i.e. $\mathbf{E} = 0$ everywhere), and which has an effective magnetic moment μ due to its circular motion in the xy plane. The Hamiltonian may then be written as

$$\mathcal{H} = \frac{m_e}{2} v_{\parallel}^2 + \mu \cdot B(z) \tag{1.15}$$

[7]In fact, $\mathcal{S}$ is bounded above by Equation 1.13 and not strictly equal to it. The received power will be attenuated by efficiency corrections such as lossy surfaces and imperfect antennas, so that in fact $\mathcal{S}$ as measured will be somewhat less than is suggested.

Because both $\mathcal{E}$ and μ are constants of the motion [8], we can rearrange this expression in terms of the parallel velocity and let the total energy $\mathcal{E}$ stand in for the value of $\mathcal{H}$:

$$v_{\parallel} = \sqrt{\frac{2}{m_e}\left(\mathcal{E} - \mu B(z)\right)} \tag{1.16}$$

Evidently, if $B(z)$ varies with z, then the component of the electron velocity which is parallel to the magnetic field will go to zero at points where $\mathcal{E} = \mu B(z)$. Consider a magnetic field that takes its minimum at $z = 0$, and increases symmetrically with z. Then for a given particle energy, there is some minimum magnetic moment that is trapped by this field configuration, equal to $\mu_{\min} = \lfloor \mu \rfloor = \mathcal{E}/B_{max}$. For any particle with a magnetic moment greater than $\mu_{\min}$, the magnetic field given by $B(z)$ will confine the particle, as the velocity component parallel to B will vanish at the turning points as defined above.

The initial magnetic moment of an electron born in a region of the trap where the magnetic field has strength $B_0 = B(z_0)$ is given[9] by

$$\mu_0 = \frac{m v_{\perp}^2}{2B_0}$$

And the total kinetic energy of the electron is of course

$$\mathcal{E} = \frac{m_e}{2}\left(v_{\parallel}^2 + v_{\perp}^2\right)$$

The turning point for this particular electron is defined as

$$B_{turn} = \frac{\mathcal{E}}{\mu_0} \tag{1.17}$$

We can choose to parameterize the motion of the electron in terms of the pitch angle θ which the electron velocity vector makes w.r.t the magnetic field direction B, and we find:

$$\sqrt{\frac{B_{\text{trap}}}{B_0} - 1} = \tan\left(\theta\right) \tag{1.18}$$

[8] The astute reader may protest that μ has nowhere been shown to be a constant of the motion. In the case where the magnetic field changes adiabatically over the motion of the electron, μ is a constant of the motion to all orders. Violating adiabaticity of the magnetic field on the scale of Project 8 would be extremely difficult indeed.

[9] Calculated in analogy with the magnetic field due to a loop of wire.

It is crucial to note that that the energy of the electron has completely vanished from our expression - the trapping condition is totally independent of the magnitude of the electron momentum. In addition, it is also impossible for our trap to confine an electron in purely parallel motion for which $\theta = 0$. Indeed, for a given maximum magnetic field $B_{\max}$ attained by the trap, there is a minimum pitch angle $\theta_{\min}$ that is trapped, and therefore a *loss cone* is established in phase space. For a given initial position in phase space (z_0, θ_0) for an electron in our trap, provided $\theta_0 < \theta_{\min}$ the electron will remain trapped.

1.6 The missing ingredient - relativistic electrons

The truly conclusive demonstration of the feasibility of CRES as a spectrometric technique is of course a functioning experiment that utilizes the technique. A standardized source of relativistic electrons emitted following a known energy distribution is the ideal target for experimentation. Of particular interest to the nuclear science community is $^{83\mathrm{m}}$Kr, a metastable isomer of krypton. This particular isomer decays electromagnetically from its excited $1/2^-$ state with $\tau_{1/2} \approx 1.8\,\mathrm{h}$ [42], and $E_{\mathrm{nuc}} = 32\,151.7(5)\,\mathrm{eV}$[44]. This decay is highly converted, with the total ratio of conversion to pure γ decays in excess of 2000[14]. Electrons which are bound to the atomic shells of Kr are ejected with characteristic conversion energies $E_{c,i}$, which are related to E_{nuc} by atomic binding energies:

$$E_{c,i} = E_{\mathrm{nuc}} - E_{b,i} \tag{1.19}$$

Where i is a proxy label for the usual spectroscopic indices e.g. K, L, and $E_{b,i}$ is the associated binding energy for that shell. A tabulation of some of the electron binding energies $E_{b,i}$ from X-ray studies[15], along with the expected conversion energy $E_{c,i}$ is shown in detail in Appendix B. The conversion electrons that are produced in these decays have very narrow radiative widths of $\Gamma \approx 1\,\mathrm{eV}$ to $3\,\mathrm{eV}$, albeit with some distortion due to atomic processes (shake-up and shake-off) which can create lower energy satellite electrons in concert.

1.7 Experimental requirements

With the conceptual difficulties in imagining a CRES experiment addressed, the actual construction of an experiment may be undertaken. Fundamentally, the experiment can be

reduced to a short list of components:

- An intense source of ^{83m}Kr that may be operated in high vacuum.
- A strong magnetic field that coerces the cyclotron motion under study.
- A system by which the ^{83m}Kr may be transported to this region of high magnetic field and analyzed.
- A method for confining to some intrumented region both the ^{83m}Kr and the conversion electrons that are thereby produced.
- A receiver capable of detecting and recording the signals produced by ^{83m}Kr conversion electrons.

With this overall outline in mind, we move on to discussing the particulars of the first demonstration of CRES as a novel spectrometric method.

Chapter 2

GAS SYSTEM

For the first experimental test of the principle of CRES, the "Project 8" demonstrator has been built with the capability to observe conversion electrons generated in the radioactive decay of ^{83m}Kr, and make accurate measurement of the cyclotron frequencies of those electrons. In order to achieve high spectral resolution, the electron must be observed for a time which is inversely proportional to the frequency resolution desired:

$$\Delta f \propto \frac{1}{\Delta \mathcal{T}_{\mathrm{obs}}} \tag{2.1}$$

For a free electron in a perfect vacuum, the observation time $\Delta \mathcal{T}_{\mathrm{obs}}$ may be taken to be infinite, and the achievable frequency resolution is limited only by radiative losses.

However, in the presence of a background gas, the electron will participate in inelastic scattering processes and thereby lose energy. In addition, it is possible for a trapped electron to scatter to an *untrapped* state, and thereby be no longer observable. The Project 8 gas system is responsible for both delivering the ^{83m}Kr under study to the analysis cell, as well as maintaining this sufficiently low background pressure so that $\mathcal{T}_{\mathrm{obs}} \gtrsim t_{\mathrm{MTBS}}$, where t_{MTBS} is the mean time between scattering for the electrons under study. The gas system, which is shown schematically in Figure 2, is of all-metal construction and has a total volume of roughly 1 L.

Figure 2.1: A schematic of the Project 8 gas system as constructed.

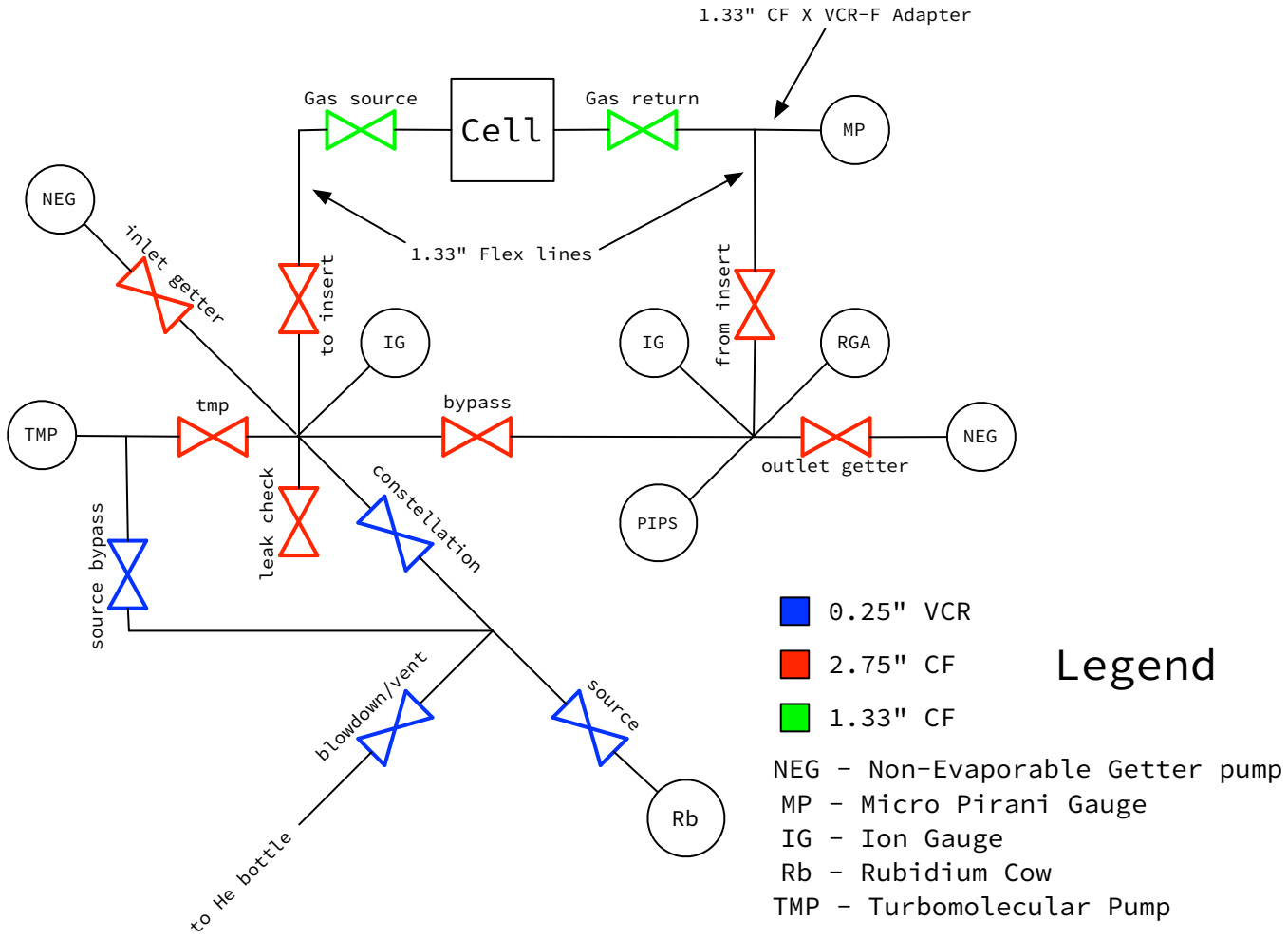

The system is divided into two regions by a bypass valve in the center (labelled bypass in Figure 2). On one side, referred to as the source side, the ^{83m}Kr source and the TMP are located. The other side, called the analysis side, contains instruments that are designed to detect the presence of the ^{83m}Kr as well as the background gas constituents. The separation of the two sides by the bypass valve serves as a mechanism by which source activity in the analysis cell may be verified - provided there is zero activity in the system at the moment the TMP valve is closed, and if the bypass valve is shut, if ^{83m}Kr is observed on the analysis side of the gas system then it must be the case that it has moved through the analysis cell.

2.1 Pressure Requirements

Consider an ideal background gas of partial pressures p_i and total pressure $P = \sum_i p_i$ at temperature T, such that the mean free path λ of an electron in such an environment may be written as

$$\lambda = \frac{1}{n\sigma} = \frac{k_B T}{P\sigma} \tag{2.2}$$

where the ideal gas law $P = nk_BT$ has been used to eliminate the number density n. The effective cross section for scattering from a background gas atom is the weighted sum of the individual cross sections for the i'th species:

$$\sigma = \frac{1}{P}\sum_i p_i \sigma_i$$

Substituting this relation into the expression for λ, and noting that the distance traveled by an electron may be related to time via its velocity β, we arrive at an expression for the mean time between scattering t_{MTBS}:

$$\begin{aligned} \lambda = \beta c t_{\mathrm{MTBS}} &= \frac{k_B T}{\sum_i p_i \sigma_i} \\ \therefore t_{\mathrm{MTBS}} &= \frac{k_B T}{\beta c}\frac{1}{\sum_i p_i \sigma_i} \end{aligned} \tag{2.3}$$

We can use this relationship along with the resolution requirement from Equation 1.11 to specify the tolerable background pressure P in the region of the trap. As an example, consider the case[1] where the background gas consists entirely of H_2 at a temperature of 100 K. Using the results[4] for total inelastic scattering ($\sigma = 3.40(7) \times 10^{-18}\,\mathrm{cm}^{-2}$) of 18 keV on gaseous T_2, the required pressure which must be maintained for an energy resolution of 1 eV is 5×10^{-5} Pa.

[1] This is a highly realistic case for a stainless steel gas system and low temperatures.

2.2 Turbomolecular and Chemical pumps

A Pfeiffer HiCube 80 Eco turbomolecular pumping station is used to reduce the total gas load of the system from atmosphere to UHV conditions. The high pumping speed of the TMP combined with the low volume of the system imply that the ultimate pressure of the pump in reached in less than an hour. However, the TMP removes Krypton from the system efficiently, thereby eliminating the isotope under study along with the background gases.

To maintain the low pressure which is established by the TMP but without pumping away the ^{83m}Kr, two SAES GP-50 non-evaporable getter (NEG) pumps are employed. The getter pumps have a pumping speed which is strongly dependent upon the specific species of gas that is present, and in particular has zero pumping speed for noble gases such as Krypton. The NEG pumps cannot, however, be used at atmospheric pressure - the active component of the NEG pump is its surface, which is rapidly depleted in atmosphere and becomes inert. Therefore, once a sufficiently low working pressure is reached using the TMP, the TMP valve is closed, and the NEG pumps maintain the vacuum.

While the getter pumps do not have the same high pumping speed as the TMP for all gases[2], they are more than adequate in the Project 8 gas system, where the background gas composition is dominated by the outgassing components of stainless steel at low temperatures.

2.3 Gas System Performance

A standard He based leak checking system attached to the leak check valve found no leaking through any of the conflat gaskets at the $1.0 \times 10^{-9}\,\mathrm{Pa\,L\,s^{-1}}$ level. In addition, the system was found to leak at the same level when tented to measure the integrated leak rate. The conclusion is that any gas load in the system emanates from a reservoir contained either in the stainless steel walls, the getters themselves, or the source beads. With the NEG

[2]The pumping speed of getter pumps as a function of species is highly variable. While a getter pump can pump hydrogen as fast or faster than a small TMP, they pump e.g. N_2 much more slowly. [7]

pumps running and the TMP valve closed, the typical working pressure of the system is $< 5 \times 10^{-7}$ Pa. This pressure has been maintained for months at a time with no turbopumping whatsoever - two orders of magnitude below the energy resolution required pressure of 5×10^{-5} Pa.

2.4 ^{83m}Kr source

The metastable ^{83m}Kr isotope of interest has a short half life of only 1.8 h[42]. However, the excited state is fed with a very high branching ratio from ^{83}Rb, which has a comparatively long half life of about 86 days[10]. Rubidium is a member of the Alkali metal group, and therefore has very similar chemistry to sodium. The chloride salt of Rb is readily formed and is highly stable, and may be used to construct a generator[45] of ^{83m}Kr.

The RbCl used in the Project 8 demonstrator is produced at Brookhaven National Laboratories and purchased in solution from Oak Ridge National Laboratories. In accordance with Venos et al[45] the RbCl is transferred to Zeolite beads with a characteristic bead diameter of 2 mm and a pore size of 0.5 nm. The RbCl is chemically adsorbed into the beads, and the solvent evaporated. The beads are transferred into a small (5 cm^3) stainless steel ampoule which is fitted with a Swagelok VCR gland. The chemistry is performed at Pacific Northwest National Laboratories (PNNL), and is then delivered to UW and baked at 150 °C in the presence of a helium purge gas to remove residual water. A pump/purge cycle using the hot He gas is performed several hundred times to ensure effective drying.

Under normal operation the source is maintained in HV conditions (by the getter pumps) such that the total pressure is $< 1 \times 10^{-5}$ Pa. Due to the noble chemistry of krypton, decay atoms which are created as daughters of ^{83}Rb are not bound to the Zeolite matrix, and diffuse out of the source freely on a time scale short compared with any relevant half life.

The activity of the source is monitored by a Canberra Passivated Implanted Planar Silicon (PIPS) detector, model number BKPD50-11-500ABM. The PIPS detector is physically inside the gas system, mounted on a high vacuum BNC feedthrough. During typical op-

eration the PIPS is biased to a voltage between 90 V to 100 V. The energy output of the preamplifier (Canberra model 2003BT) is shaped by a spectroscopy amplifier, and the pulse height recorded by an ORTEC Multi-Channel Analyzer (MCA). The MCA is read out by a computer running ORCA. The capacitance of the detector and feedthrough generate a noise floor which is comparable to the energy of the the K-shell 17.8 keV line, rendering it invisible. However, the L-shell conversion electrons are well resolved.

Chapter 3

MAGNET

A CRES experiment requires a suitable magnetic environment for operation, defined by a highly uniform magnetic field over the physical extent of the trapping volume. The Project 8 prototype is operated in the bore of a Spectrospin 200 MHz superconducting NMR magnet manufactured by Bruker Biospin Corporation in 1998.

The quench history of the magnet before it was acquired by the Project 8 collaboration in 2013 is almost completely unknown. Two known magnet quenches have occurred:

- The magnet was warehoused at full field (4.5 T) at some time in the past 10 years. Cryogen service was stopped, and eventually the magnet quenched. The magnet was not serviced or refilled with cryogens until Project 8 took ownership of the magnet in 2013. The condition of the Z^3 correction coil, which is inoperable due to a heater fault, may be a consequence of this quench.

- While installed in the Project 8 lab, a poorly calibrated liquid helium level sensor misled the collaboration to believe that the magnet was submerged in cryogens when it was in fact not. A quench occurred at a field strength of about 1 T. No damage from the quench has been observed.

3.1 Description

The magnet coils are manufactured from niobium-titanium alloy, with a critical temperature of T_c =9.2 K[23]. The magnet coils are maintained in their superconducting state by immersion in a bath of liquid helium (LHe). The LHe bath is surrounded and insulated by a jacket of liquid nitrogen (LN). Heat transported into the Dewar from the surrounding environment preferentially warms the LN by design, and thus the 43 L LHe volume is

relatively stable, with a very low liquid boiloff design rate of $9\,\mathrm{mL\,h^{-1}}$. LN is evaporated at a rate of $180\,\mathrm{mL\,h^{-1}}$, and therefore must be refilled twice a week with roughly 20 L to maintain the optimum LN volume of 52 L. When the Dewar is completely full of cryogens, the total system weight is 304 kg [11].

For reasons unknown, the actual observed LHe boiloff rate of the magnet is much higher than the design rate. A typical measured boiloff rate is $18\,\mathrm{mL\,h^{-1}}$ as measured by an instantaneous gas flow meter. Understanding the source of this discrepancy should reduce the cost of operating the experiment by perhaps as much as a factor of two.

The Spectrospin 200 MHz magnet is designed to produce a highly uniform field over the typically small volume of a liquid NMR sample (i.e. $\mathcal{O}(\mathrm{mm}^3)$). The bore of the magnet is oriented vertically, as are the fields produced by the coils. A small vacuum insulation space separates the magnet itself from the bore of the dewar, such that the magnet may be said to be 'warm bore' in the sense that the magnet may be maintained at 4 K while the bore of the magnet is at room temperature (or higher). The bore of the magnet is 52 mm in diameter, $\sim$1 m in height, and is constructed from aluminum.

The uniformity specification of the magnet, is $<$ 1ppm over a Z axis extent of 55 mm, with a secular field drift[11] of no more than $2\,\mathrm{Hz\,h^{-1}}$(10 ppb /hour) at a field of 4.5 T .

To achieve the above uniformity specification, superconducting correction ("shim") coils must be used. The shim coils are a system of coils, each of which produces a much smaller field than the main field, but whose magnetic field is tailored to a specific shape so as to cancel magnetic field inhomogeneities produced by the main coil. The Project 8 magnet has 9 such superconducting shim coils installed in the dewar, each referred to by the specific inhomogeneity component which it is designed to correct - X, Y, Z, XZ, YZ, XY, Z^2, and Z^3. The shim coils are wired in series, but each has an independent persistent switch. All of the shims with the exception of the Z^3 coil are fully operational - the Z^3 coil heater cannot be operated due to a fault in the dewar.

Figure 3.1: An outline drawing of the Spectrospin 200 MHz magnet. [11]

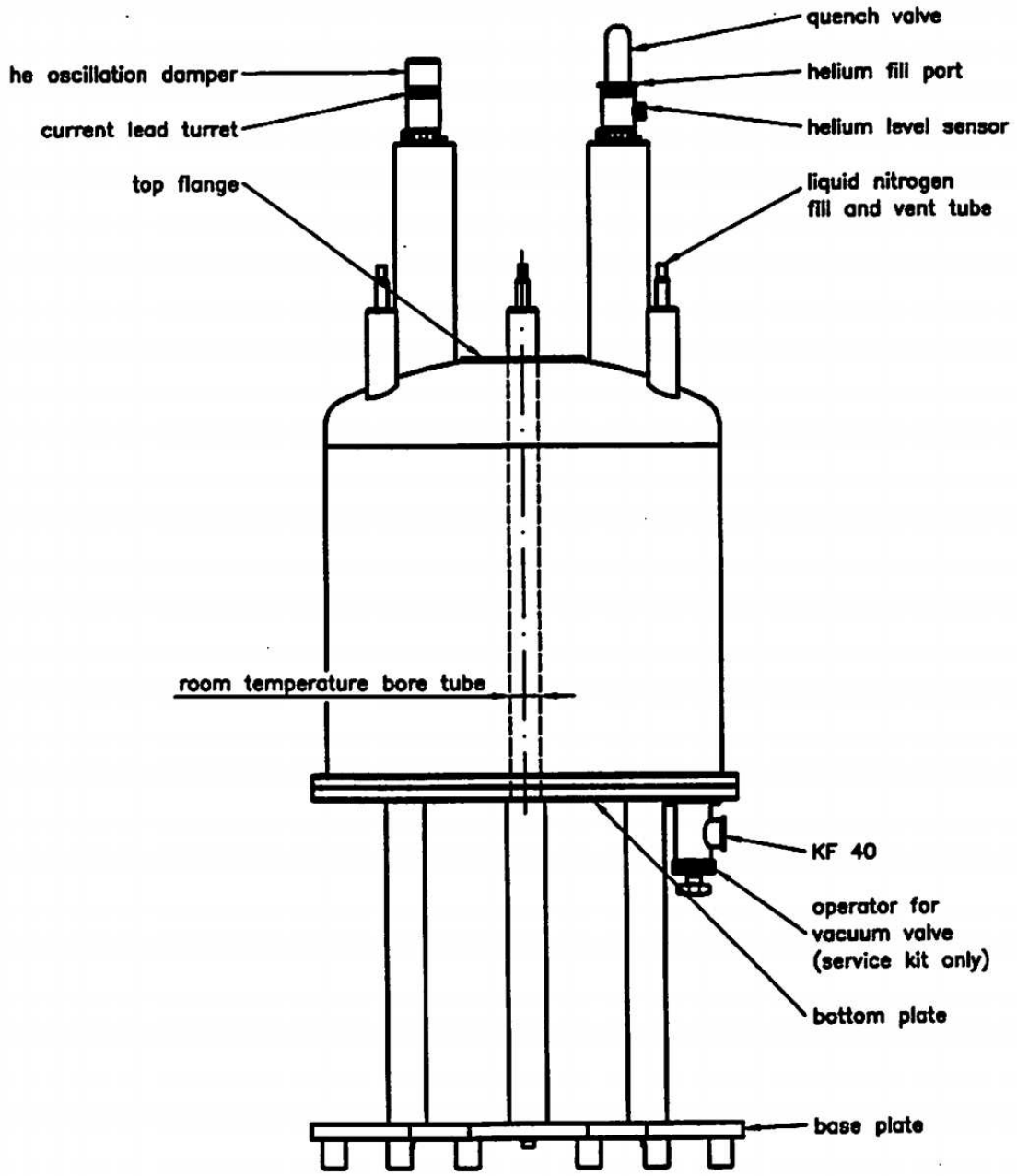

Figure 3.2: The circuit diagram for the magnet coils. The main magnet coil is on an independent circuit, while the shim coils are all wired in series with each other. The main magnet and all of the shim coils have independently controlled persistent switches.

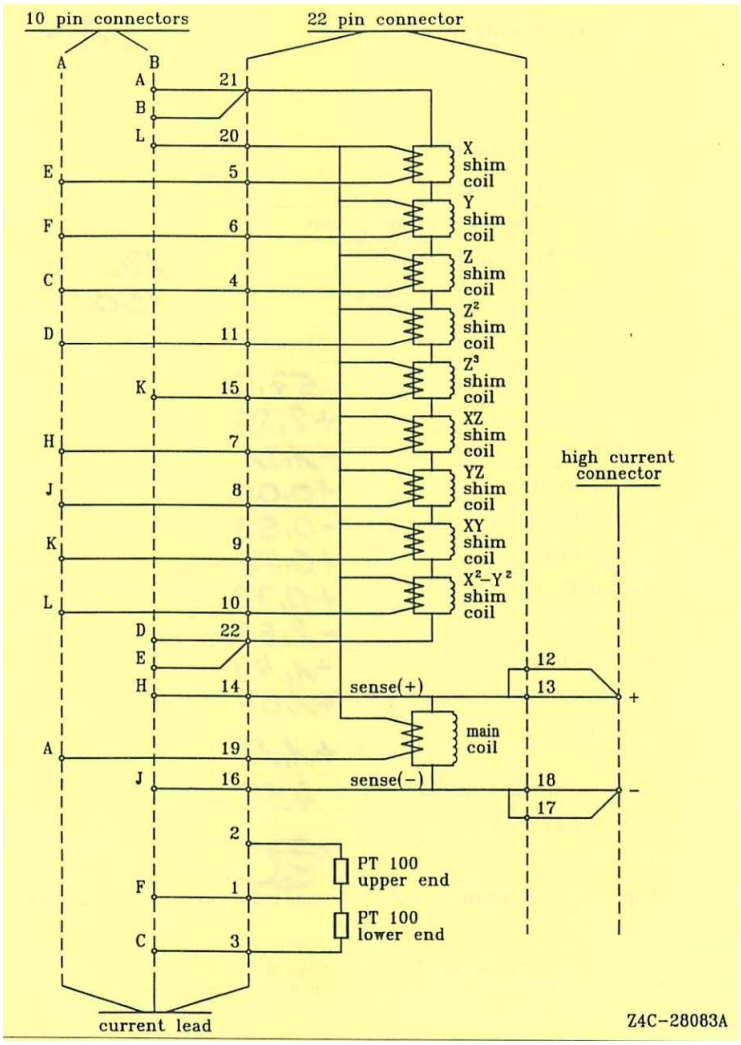

A typical field for Project 8 is near 1 T, which requires a main magnet current of close to 11 A. The shim coils are operated at much lower currents - a few amperes or less. When in operation, the main coil as well as the shim coils are operated in persistent mode.

The main coil inductance is 53 H. The current for all of the coils is sourced from a common power supply, Cryomagnetics model 4G-100-SHIM. The power supply also controls

the persistent switch heaters for the main and shim coils. Due to an unusually high current requirement for the persistent switches, an external relay driver was constructed by the CENPA electronics shop which is controlled by the power supply output. A representative schematic of this circuit is shown below in Figure 3.1.

Figure 3.3: A schematic of the circuit which is used to power the persistent switches in the Spectrospin 200 MHz magnet. The persistent switch heater current generated by the power supply is used to drive the switching side of a solid state relay. An internal constant current supply generates the larger current needed to activate the persistent switch. Each of the 9 superconducting shim coils has its own copy of this circuit.

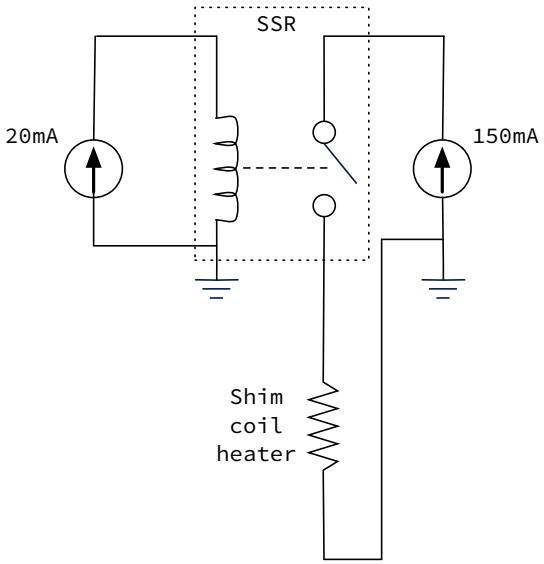

3.2 Magnetic Field Mapping

Axial (i.e. z-axis) field homogeneity of the magnetic field produced by the main magnet is necessary[1] but not sufficient for a successful CRES experiment. Any magnetic field gradient in the radial direction of the bore will produce a so-called "magnetron" component of the electron motion. The magnetron motion defines an orbit around the $r = 0$ point of symmetry

[1]Of course, there must be an inhomogeneity which is introduced in the form of a trap in order to perform CRES, but this is not apropos to the discussion of the main magnet.

of the magnetic field, which will "crash" the electrons into the wall of the waveguide before they can be detected[2] if the geometric axis of the waveguide is not aligned with that of the magnetic field. If azimuthal symmetry of the magnetic field is satisfied, Maxwell's equations demand that in the current-free region of the magnet bore the axial and radial gradients are related in a simple way:

$$\begin{aligned} \nabla \cdot \mathbf{B} &= 0 \\ \implies r^{-1}\partial_r \left(rB_r\right) + \partial_z B_z &= 0 \end{aligned} \tag{3.1}$$

For a solenoidal coil, the leading order expansion of the radial magnetic field component scales as $B_z rz$, so near the center of the solenoid we should expect that the radial inhomogeneity $\partial_r B_r$ to be of the same scale as the axial specification of 1ppm.

However, the assumption that the azimuthal gradient is exactly zero in Eqn. 3.1 is certainly not a good one, and in fact this assumption may be violated in a number of ways. Firstly, the need for correction coils which are azimuthally asymmetric (such as $X^2 - Y^2$) would be unnecessary if the field were symmetric to begin with. Furthermore, in the event that the magnetic field is tilted with respect to the bore, azimuthal symmetry is no longer a good assumption and the radial and axial gradients are only equal and opposite up to the contribution from the azimuthal gradient. A direct observation of this is shown by comparing the left and right panels of Figure 3.5.

As a function of strictly Z, the uniformity of the unshimmed main coil field as seen in Figure 3.4 is manifestly best between $z = -20\,\text{mm}$ and $z = 20\,\text{mm}$. If the assumption is made that the magnetic and geometric axes are equivalent, and that the azimuthal variation of the field should be negligible, the shape of the field may be explained as the magnetic field falling off as the probe is moved out of the highly uniform region and therefore away from the center of the coil where the field is strongest.

However, as can be seen in Figure 3.5, the magnetic field at $z = -20\,\text{mm}$ is clearly not

[2]Typical magnetron frequencies in the Project 8 experiment are $\mathcal{O}(100\,\text{kHz})$, so that the typical timescale associated with this motion is $\mathcal{O}(10\,\mu\text{s})$, comparable to the mean time between scatterings.

Figure 3.4: The magnetic field of the main magnet coil, as measured on the geometric axis of the bore ($x = y = 0$).

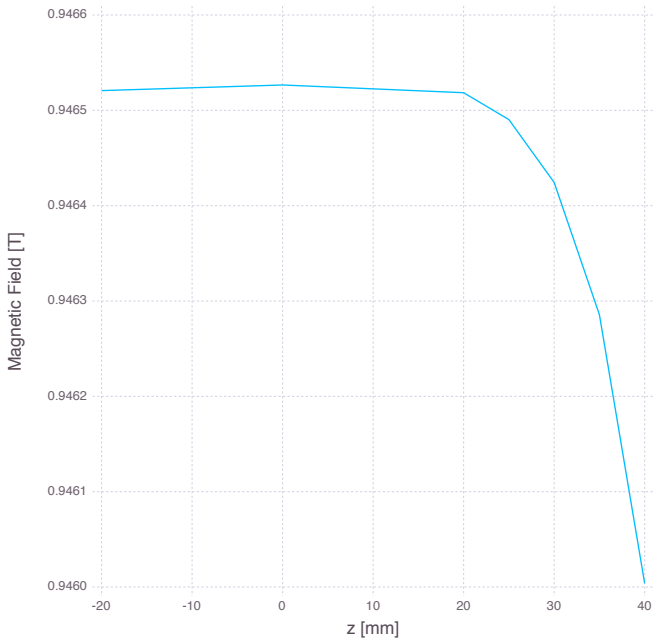

centered, and the azimuthal dependence of the field is nontrivial. Two conclusions are possible from this data: either the magnetic axis is *tilted* with respect to the geometric axis, and therefore the large values for z <20 mm are a result of sampling the magnetic field in a region where it is large compared to the central field, or the natural magnetic axis inside the main coil is not centered with respect to the geometric axis. In either case, this discrepancy underscores the necessity for precise magnetic field mapping off the geometric axis of the magnet bore.

The data in Figure 3.5 was taken using a custom NMR probe positioning device. The device consists of three controls, one for the Z (height) coordinate, and two that control the position of the NMR probe in the (ρ, θ) plane.

The NMR magnetometer is a Metrolab Teslameter system, model PT-2025. The probe

Figure 3.5: Two voronoi plots showing slices through the main magnet field, taken at two z positions in the region where the variation of the field strength with z is minimal. Each cell is formed by voronoi triangulation over the points at which the magnetic field is measured. The color of each cell is determined by the strength of the magnetic field at the center of the cell, relative to the field at the center of the plot.

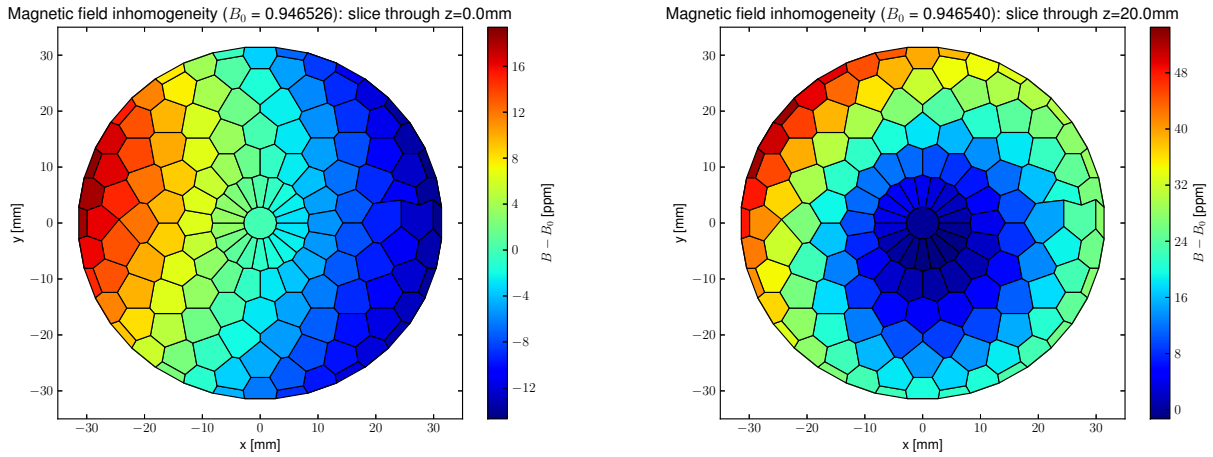

itself is a MetroLab #4 probe, which may be used in the range 0.35 T to 1.05 T. The probe sample is a 4 mm×4.5 mm ampoule of D_2O. The required field homogeneity for operation is between 800 ppm /cm to 1500 ppm /cm. The teslameter itself has a resolution of 1 Hz, a relative precision of "less than 0.1 ppm" (no precise figure is given), and an absolute accuracy[41] of 5 ppm.

The ρ and θ position of the probe is controlled by adjusting two angular degrees of freedom. A large knurled nut is mounted at the top of the probe positioner which rotates the probe around the geometric symmetry axis of the magnet bore. Inset in this nut is a smaller nut, which rotates the probe around a radially fixed point $\rho = \mathrm{R}/2$ where R is equal to the bore radius of the magnet. These two angular coordinates are denoted by θ_c and θ_e, respectively, where the indexes c and e stand for "concentric" and "eccentric" in reference to mechanical gears of the same name. θ_c and θ_e each have an inscribed index with 5° precision.

Figure 3.6: A functional sketch of the NMR mapping device. The angular and radial DOF are controlled by adjusting θ_c and θ_e. The z position is controlled by the motion of a M63×2.5 lead screw.

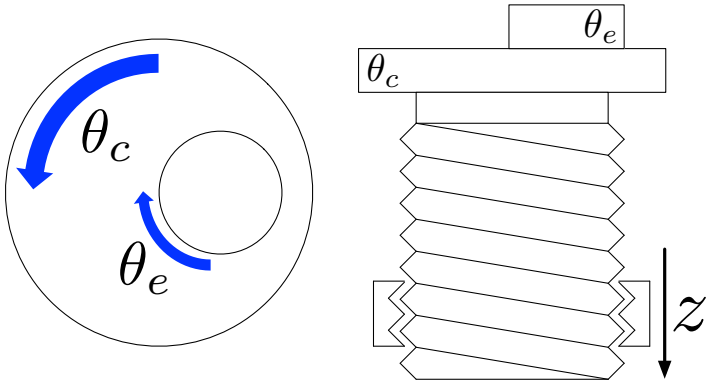

The position of the NMR probe in the Z axis is controlled by a large diameter M63×2.5 lead screw machined from 6061 aluminum (6061Al). Motion of the lead screw is controlled by turning a large knurled nut which is inset on a stage cut from 6061Al. The threads of the nut are cut from brass to prevent galling. The circumference of the stage has an index that indicates the fine Z position of the probe. A solid 6061Al rod is affixed to the lead screw stage and extends upward the full extent of the lead screw, where it penetrates the azimuthal adjustment stage. An index is inscribed on the rod, which may be used to determine the coarse Z position of the probe.

The probe itself is held rigidly in place at the end of hollow 6061Al cylinders by a teflon end piece to minimize diamagnetic corrections at the position of the probe from surrounding material. The cylinders are tack welded to the bottom of the angular dials for strength.

The full motion of the probe may then be described as epicyclic about the geometric axis of azimuthal symmetry of the magnet bore, with the deferent determined by θ_c and the epicycle determined by θ_e. Converting to standard cartesian coordinates is then straightforward, and cylindical coordinates almost as direct:

Figure 3.7: The SolidWorks drawing from which the NMR probe holder was built. The top aspect of the instrument is shown here. The light yellow dial controls θ_c, and the inset dark red dial controls θ_e. The purple index indicates the coarse z position, and the lower inset pink dial indices the fine z position. The M63×2.5 lead screw is cut into the green piece, and the brass nut is cut on the ID of the pink dial.

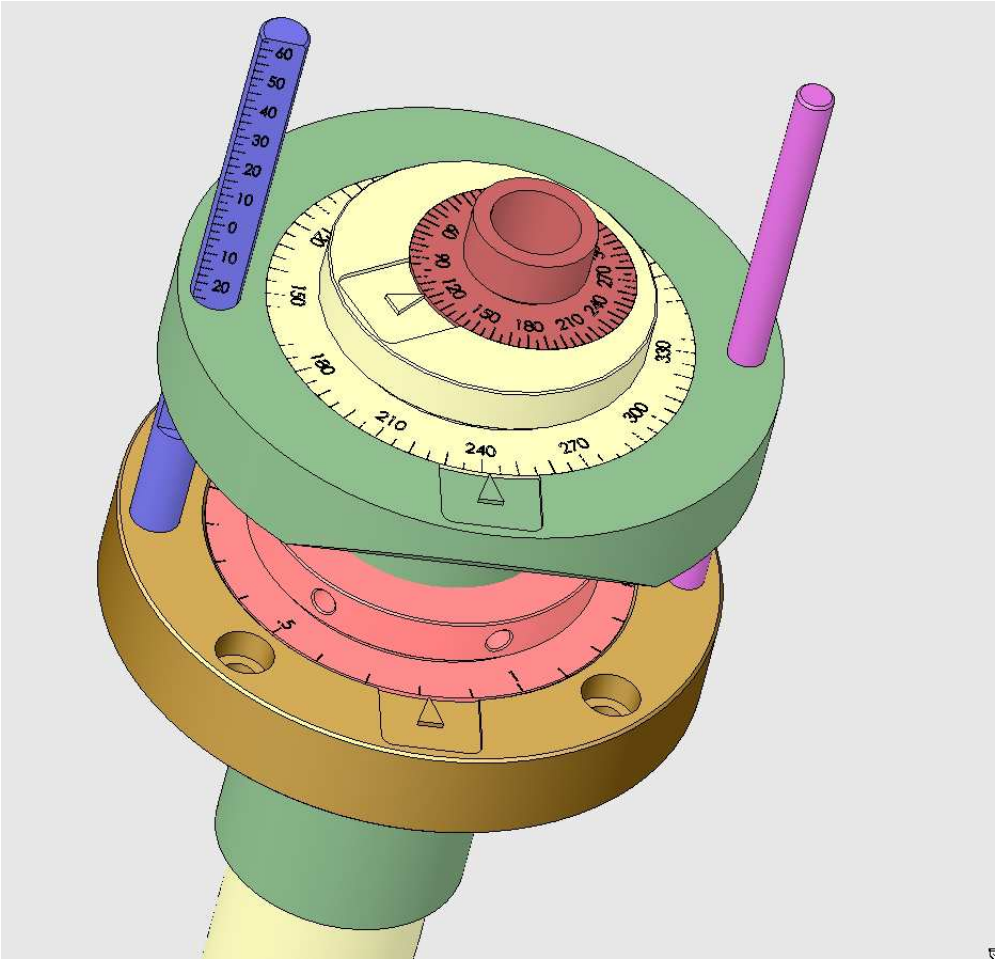

Figure 3.9: A conversion table between probe-centric coordinates and ordinary rectilinear coordinates.

Cartesian			Cylindrical
x	$R\left[\sin\left(\theta_c+\theta_e\right)-\sin\left(\theta_c\right)\right]$	$\sqrt{2}R\sqrt{1-\cos\left(\theta_e\right)}$	ρ
y	$R\left[\cos\left(\theta_c+\theta_e\right)-\cos\left(\theta_c\right)\right]$	$\tan^{-1}\left[\dfrac{\cos\left(\theta_c+\theta_e\right)-\cos\left(\theta_c\right)}{\sin\left(\theta_c+\theta_e\right)-\sin\left(\theta_c\right)}\right]$	θ
z	z	z	z

Figure 3.8: A cutaway view of the NMR probe holder mechanism. Colors are unique to each individual piece and maintain meaning through each drawing. Hollow 6061Al tubes are welded to the angular controls and penetrate the entire length of the bore to reach the teflon probe holder. The NMR probe itself is depicted in dark red, and the teflon holder in purple.

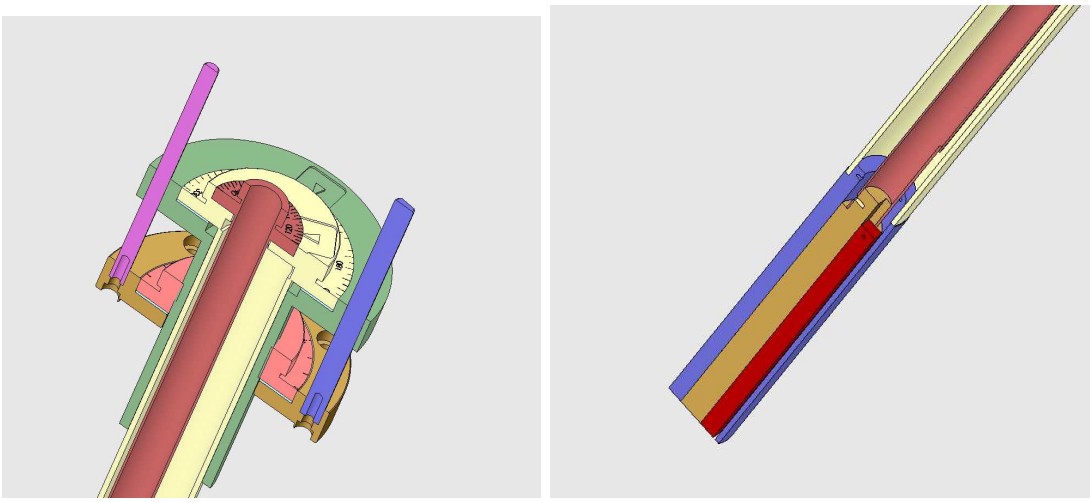

3.2.1 Mapping results from the NMR main magnet

To investigate possible offsets or tilts of the magnetic field with respect to the magnet bore, a detailed magnetic field map was made of the main magnet. 1141 measurements of the magnetic field produced by the primary solenoid of the NMR magnet were made using the three axis NMR probe positioner. Steps of 20° were taken in the θ_c and θ_e coordinates, and 5 mm in the z coordinate. The NMR probe uncertainty at any given measurement point was consistently 1ppm. The results and implications of this mapping are discussed in the next section.

3.3 Magnetic Field Shimming

To correct for spatial inhomogeneities of the main solenoidal coil, current may also be introduced into the shim coils. The shim coils form a separate circuit from the main coil, and so may be charged independently to compensate the main field. Determination of the

"correct" shim currents for maximum homogeneity requires knowledge of the effect of each individual shim coil on the field, and thus maps of the shim coil contributions themselves have also been generated.

To generate a shim coil map, the main field must first be energized to some nominal value in the range 0.35 T to 1.05 T - the shim coils cannot themselves generate a field of sufficient magnitude for the NMR probe to be operable without being energized with a dangerously high current. Once the main magnet is energized, the field is mapped using the three axis mapper. The shim coil contribution is then measured by energizing each shim coil individually to some known current, nominally 3.0 A, and the total field from the main coil plus the energized shim coil is mapped. The main coil contribution is then subtracted from the total field to yield the contribution from the shim coil alone.

After the shim coil under study is energized to the correct current, the shim coil is placed in persistent mode. The persistent switches to all other shim coils are then energized sequentially, so that any induced current is dissipated as heat in the resistance of the persistent switch. The coil under study is then taken out of persistent mode, and the power supply actively regulates the shim current at 3.0 A while the field is being measured. The mapping procedure takes approximately 6 hours for the full 1100 point scan, and therefore the secular drift of the magnet is expected to contribute only at or below the 50 ppb level - well below the precision of the NMR probe itself.

The fields thusly measured are then divided by the applied current in each case to yield the "shape factor" **s** for the coil. The shape factor is a well motivated quantity for the case of a constant current from the Biot-Savart law:

$$\mathbf{B} = \frac{\mu_0 i}{4\pi} \int_C \frac{d\ell \wedge \mathbf{x}}{x^2} \equiv i\mathbf{s}$$

Where the shape factor **s** is entirely determined by the geometry of the current distribution. The total combined field from the main coil plus the shim coils may then be written

as a sum over the coil shape factors:

$$\mathbf{B} = \sum_j \mathbf{s}_j i_j \tag{3.2}$$

Where i_j is the current applied to the j'th coil, and the index j runs over the main coil and all shim coils.

3.3.1 Magnetic field optimization

Equation 3.2 forms the basis of an optimization problem:

> Given a desired field $\mathbf{b}$, what is the optimal set of currents $\{i_j\}$ which appear in Equation 3.2 such that the quantity $|\mathbf{b} - \sum_j \mathbf{s}_j i_j|^2$ is minimized over some volume, subject to the constraints that the total field must lie in a specified range $B_{\min} < B < B_{\max}$ and the shim coil currents may not exceed their limits $\{i_{j,\max}\}$?

The following observations motivate a solution to this problem:

1. Up to mutual inductances between the coils, the shape factors $\mathbf{s}_j$ may be measured independently. Induced currents may be eliminated by resistive dumping of all shims which are not actively energized. Furthermore, any residual induced currents depend only on the flux linkage between any given pair of coils - the induced current in coil j when current is introduced into coil i depends *only* on the current in coil i, and not the state of any other coils.

2. The currents that optimize $\mathbf{b} - \sum_j \mathbf{s}_j i_j|^2$ need not be positive, or even nonzero.

3. The shape factors $\mathbf{s}_j$ may be adequately represented by some discrete set of measurements $\mathbf{s}_{kj}$ taken at a chosen set of representative points $\{\mathbf{x}_k\}$.

Let M_{kj} denote the measurement of the shape factor $\mathbf{s}_j$ at the discrete point $\mathbf{x}_k$. Then $\mathbf{M} = M_{kj}$ forms a matrix of size $P \times C$, where P is the number of sampled points, and C is the number of coils. Equation 3.2 may be recast in matrix form:

$$\mathbf{B}_k = M_{kj} i_j$$

And so by specifying the desired field $\mathbf{b}$ at the same set of measurement points $\{\mathbf{x}_k\}$, the above optimization problem reduces to minimizing the ℓ^2 norm $||\mathbf{M}\cdot\mathbf{i}-\mathbf{b}||_2$, subject to the constraints that the shim currents i_j not exceed their maximum value.

The problem of minimizing a matrix norm may be efficiently solved by convex programming techniques. The ECOS solver[17] was used to find optimal currents for both the 1-dimensional case (i.e. shimming only along the line $x = y = 0$), as well as the fully three dimensional case.

3.3.2 An example: one-dimensional Z axis shim coil optimization

Measurements of the shape factor of the main coil suggest that significant uniformity may be achieved by simply applying a quadratic correction with the Z^2 coil, as may be seen in Fig. 3.4. The shape factors of the main coil as well as the Z^2 coil were measured at 41 points along the line $x = y = 0$ corresponding to the geometric axis of the magnet bore and are shown in 3.3.2.

Convergence of the ECOS solver was achieved in 8 iterations with a running time of $\approx$1 ms, with the quantity $||\mathbf{M}\cdot\mathbf{i}-\mathbf{b}||_2$ reaching a minimum value of $3\times10^{-9}\,\mathrm{T}^2$. The specified target $\mathbf{b}$ for the minimization was a constant field of 0.945 T, and the optimum currents were found to be i_{main} =11.6311 A and i_{z^2} =1.696 04 A. The resulting field differs from the target by no more than 2×10^{-6} T over the z axis extents of -25 mm to 25 mm. The result of the one-dimensional shim optimization is plotted in Figure 3.3.2 in terms of the homogeneity of the field with respect to the total average field. In addition, the total unshimmed field and the total shimmed field are shown superimposed to highlight the dramatic difference in field homogeneity. Also of note is the shape of the residual field - it is clear that further improvements can be made by using the Z correction coil.

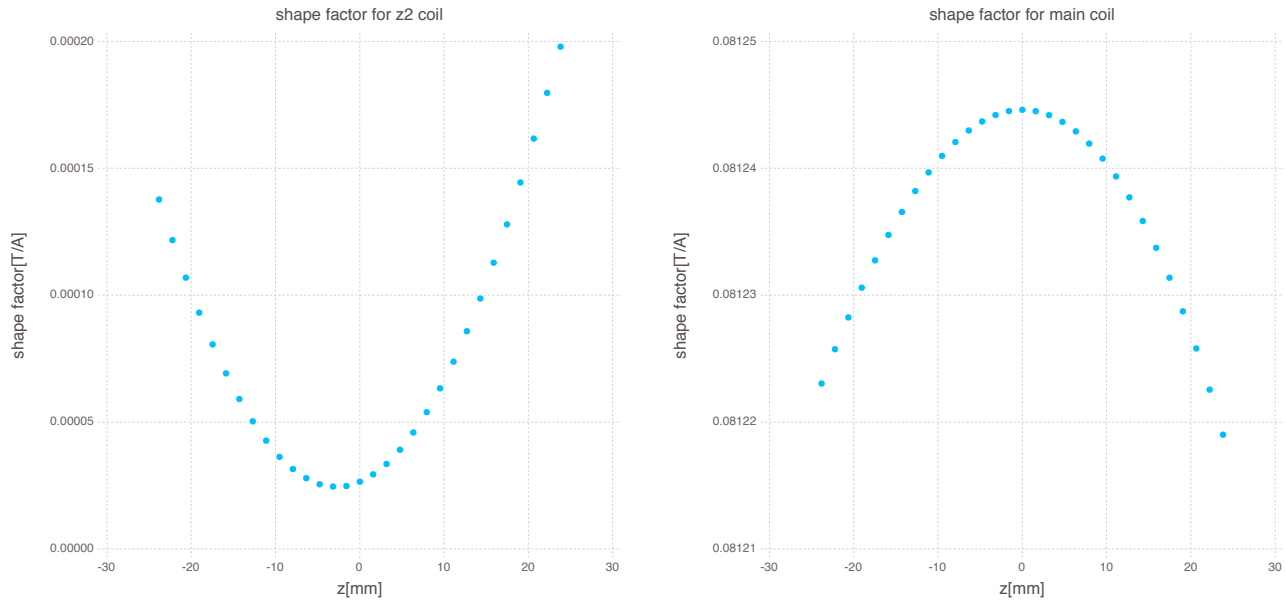

Figure 3.10: The measured shape factors for the main(right panel) coil, and the Z^2(left panel) coil.

3.3.3 Three dimensional shim coil optimization

An appealing property of the above optimization is that it does not require the geometry of the problem to be specified - any number of points may be used for the optimization, and their spatial relationships are entirely unconstrained by the problem. This property can be used to extend the above results to be fully three-dimensional.

The magnetic field from each of the 9 coils was recorded using the NMR mapping device at a predetermined set of 133 points. Data were taken at 19 different z positions, with 7 points describing a hexagon and their geometric center (see Figure 3.3.3) used at each z-slice. During each coil measurement, the main magnet and exactly one other coil were energized to a predetermined current. The other shim coils which were not undergoing mapping were resistively dumped as decribed above to prevent contributions to the shape from mutually induced currents. While it would be preferable to measure only the shim

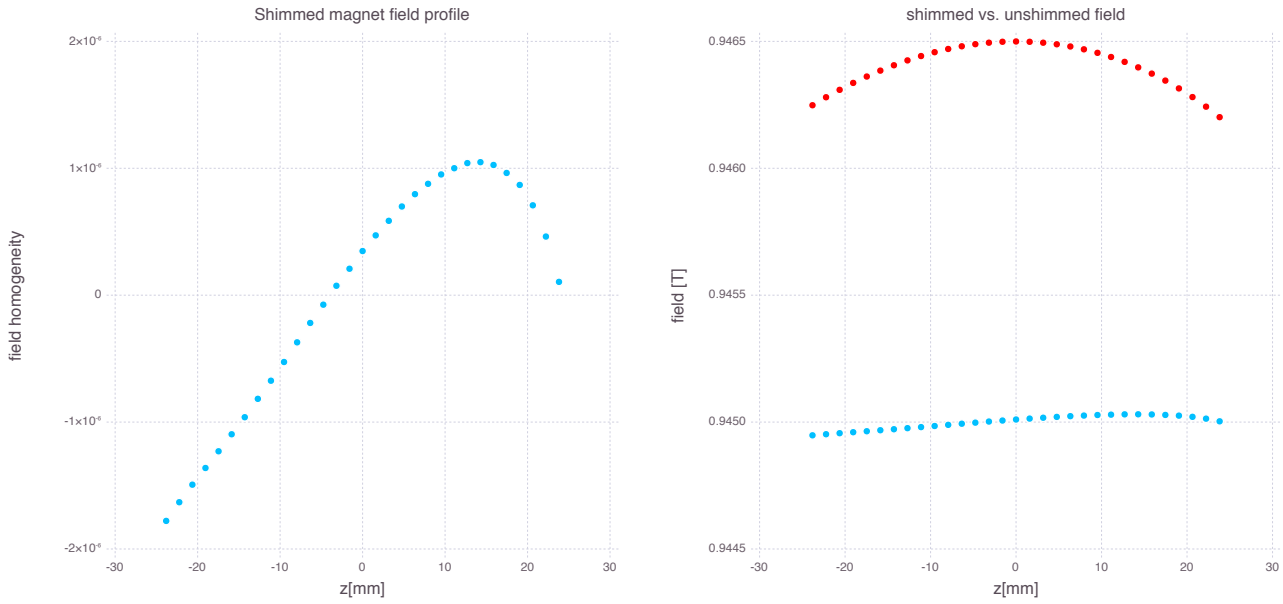

Figure 3.11: Results of 1-D shimming of the magnet using only the Z^2 coil.

coil in question without the influence of the main magnet, the magnetic field range over which the NMR probe functions is such that the main magnet must be co-energized for the measurement to be performed.

The solution obtained by the optimization procedure yields an axial homogeneity of better than 2ppm over the entire z-axis range, and better than 0.1ppm within 1 cm of the $z = 0$ position.

3.4 Magnetic Bottle Coils

In addition to the electromagnets which are installed in the Bruker magnet, three small magnetic trapping coils are wrapped on the waveguide cell itself. The central coil (called the main trapping coil) is a two layer solenoid coil made from 61 total turns of AWG36 wire located at the geometric center of the waveguide cell. The length of the coil is 7.62 mm and its inner diameter is 13 mm. The physical parameters of the coil were chosen so as to achieve

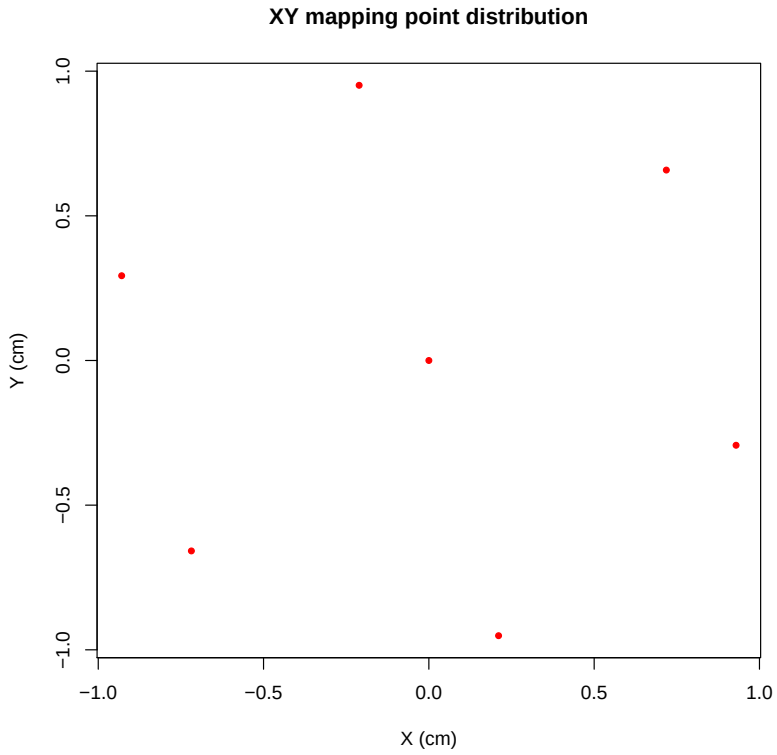

Figure 3.12: The distribution of points in the xy plane which were used to fully optimize the magnetic field.

a quadratic field gradient near the $z = 0$ axis of $10\,\mathrm{mT\,cm^{-2}}$. Hall probe measurements of the field shown in Figure 3.4 confirm this gradient is achieved at a steady state current of about 1.25 A.

The two remaining coils are located at $z = \pm 27.05\,\mathrm{mm}$ relative to the center of the main trap coil. These coils are similar to the central coil in terms of diameter, but differ in that they are both 6.35 mm long, and use a total of 51 turns of AWG36 copper wire each. When these two coils are energized simultaneously and with the same field polarity as the main magnetic field, a field configuration known as a "bathtub" trap is formed. The bathtub trap is characterized by a much flatter bottom than the central coil, and in addition has much steeper edges. The quadratic fits and raw data are shown below in Figure 3.4.

Figure 3.13: The main trap coil field as measured by a Hall probe is shown with a quadratic fit near the field maximum superimposed. The fit indicates that the gradient near the center of the coil is about $16\,\mathrm{mT\,cm^{-2}}$.

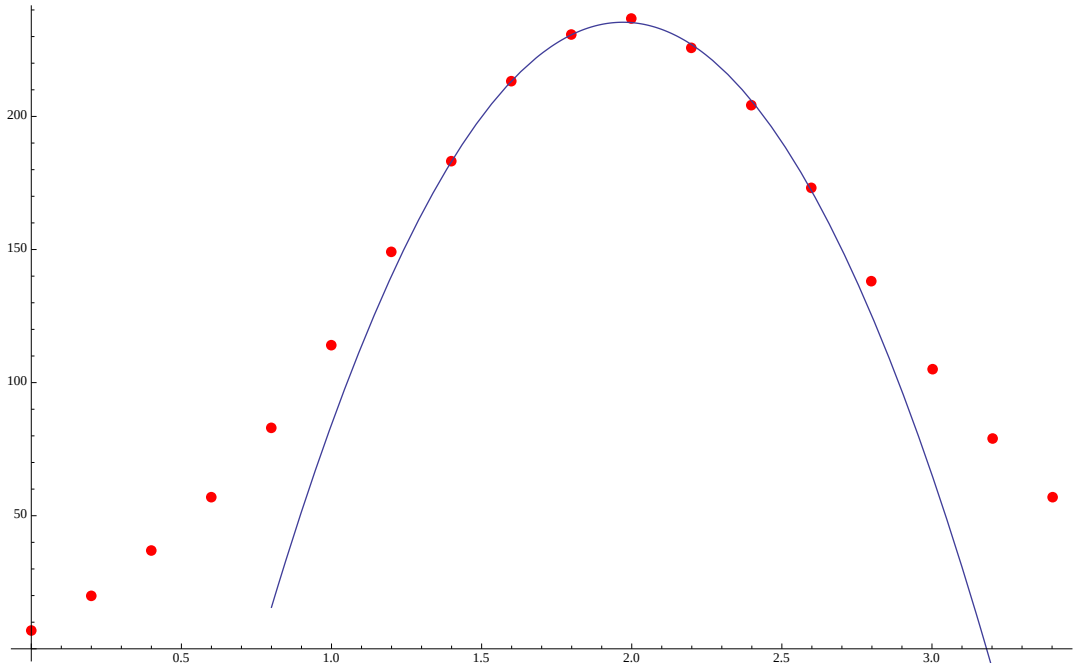

The effect of these coils on the total magnetic field and on the dynamics of electrons is discussed below as a component of the data analysis.

3.5 Magnetic Field Instrumentation

The NMR probe measurements are inherently ex-situ, as the probe itself occupies the entire magnet bore and leaves no room for the insert. In order to determine the magnetic field in-situ, two additional methods are used while the insert is installed in the magnet bore.

A Hall effect magnetometer is attached mechanically to the outside of the waveguide cell (described in a subsequent section devoted to the insert). The accuracy of the magnetometer (a Lakeshore HGCA-3020) is quoted by the manufacturer as $\pm 2\%$, which is sufficient to localize the cylotron frequency of an electron only to within roughly $\pm 500\,\mathrm{MHz}$ at a field

Figure 3.14: The bathtub coil fields are shown here as measured by a Hall probe on the z axis. Each dataset has superimposed on it a quadratic fit calculated near the center (i.e. points which are within 7 mm of the maximum. The gradients are roughly equal to $14\,\mathrm{mT\,cm^{-2}}$ each. The data shown were taken at an applied current of 1 A.

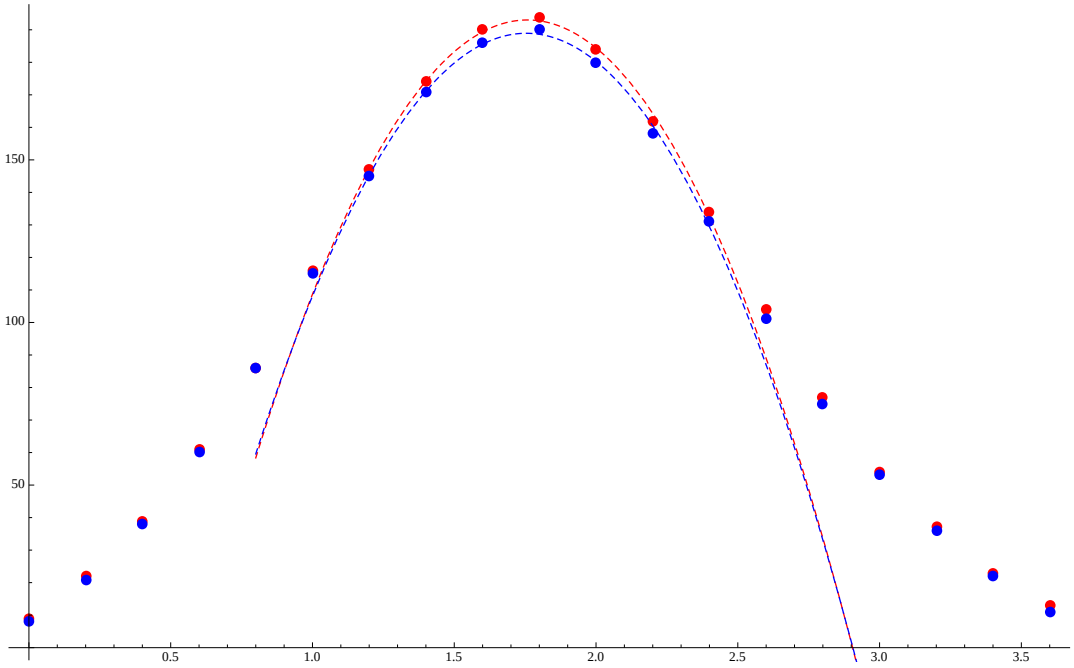

strength of 1 T. In addition to this rather poor frequency localization, the usefulness of the Hall probe measurement as a tool to locate electron signals in frequency space suffers due to the fact that the probe is not installed in the same physical region as the magnetic bottle. The magnetic bottle coil windings prevent the probe from being installed at the same z position as the trap center, and the waveguide itself is a mechanical barrier in the xy plane. The probe is therefore installed approximately 1 cm from the actual trap position. Consequently, the Hall probe serves mostly as a rough guide to the position of the insert in the magnet bore, but not as a precision measurement of the magnetic field itself.

A more accurate measurement of the magnetic field may be made using the Zeeman effect. A sample of 2,2-diphenyl-1-picrylhydrazyl (DPPH) which is small enough to fit in

the waveguide is installed just above the upper Kapton window of the waveguide cell. The DPPH is sealed under vacuum in a Pyrex ampoule 3 mm in diameter and roughly 0.5 cm long. The DPPH molecule has an unpaired electron which has an effective g-factor[2] of 2.0036 ± 0.0002. In a constant magnetic field of strength B, the Zeeman splitting for this unpaired electron is

$$\Delta U = U^+ - U^- = g\mu_B B$$

Where μ_B is the Bohr magneton, and g is the g-factor of the electron in question. Photons of energy ΔU may be absorbed by the electron and drive the transition between the aligned and anti-aligned states of the electron spin, and the absorption of those photons can be used as a probe of the local magnetic field strength B. The photon frequency that corresponds to this splitting energy is given by substituting the value of the Bohr magneton in the above relation and solving

$$\begin{aligned} hf_{abs} =& gB \cdot \frac{e\hbar}{2m_e} \\ \implies f_{abs} =& g \cdot eB4\pi m_e = \frac{g}{2} \cdot f_c \end{aligned} \tag{3.3}$$

Where f_c is the usual cyclotron frequency (at zero energy) for an electron in the magnetic field B. Given the DPPH g-factor of 2.0036, the electron spin resonance signal differs from the cyclotron frequency by 0.2%. The proximity of the ESR signal to the cyclotron signal under study is highly convenient from an experimental standpoint, as the receiver used to detect the cyclotron signals may also be used to measure the absorption of microwaves by the DPPH sample in the waveguide, and therefore the magnetometry shares many of the systematics of the main physics measurement.

When microwaves at the ESR splitting frequency propagate past the position of the DPPH sample, some (extremely small) fraction of them will be absorbed. For the purpose of the ESR measurement, the output of the receiver is terminated in an RF power diode whose output voltage is proportional to the input RF power level. A lock-in amplifier drives a solenoid wrapped around the sample at a frequency of typically 1 kHz while the frequency of radiation in the waveguide is swept by an external source. When the swept

source frequency is near resonance, some fraction of the RF power is absorbed by the DPPH. Due to the modulating field of the solenoid, the amount of power absorbed oscillates *at the driving frequency*, and the signal can be locked-in by the amplifier. The output signal from the lock-in is a derivative of the absorption curve, and consequently its zero crossing is a measure of the frequency at which the absorption of power by the DPPH is maximized. An example spectrum is shown below in Figure 3.5.

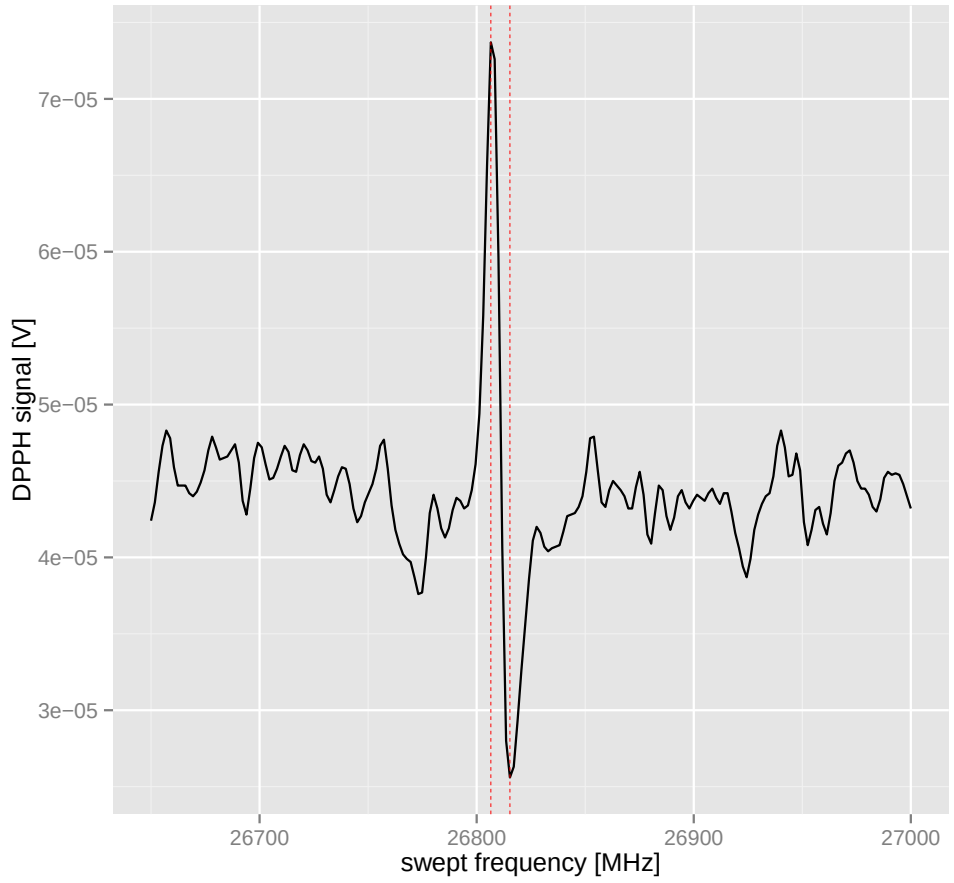

Figure 3.15: A recorded trace from the ADC output of the lock-in amplifier showing the characteristic absorption curve of the DPPH. The FWHM is marked by red lines and is equal to 8.75 MHz. Using this as a conservative estimate of the accuracy of this technique yields $\sigma_B/B \approx 400$ ppm.

Chapter 4

DETECTOR INSERT

4.1 Waveguide

In the late 19^{th} century, the discoveries of Faraday and Maxwell in the field of electromagnetism were firmly embraced by scientists, leading to a period of intense study of the consequences of the electromagnetic theories of the day. Oliver Heaviside, who in 1884 distilled Maxwell's twenty equations in twenty unknowns into the familiar four differential equations that we know today, turned his attention to the development of a practical theory of transmitting electrical power. His new theory, which we know today as transmission line theory, described the method by which electromagnetic waves could propagate along signal cables. Heaviside concluded from his studies that "It does not seem possible to do without the inner conductor, for when it is taken away we have nothing left upon which the tubes of displacement can terminate internally, and along which they can run... It would appear that the only way of completely solving the problem of the automatic transmission of plane waves within a single tube is a theoretical one, employing magnetic as well as electric conductance"[27].

In 1897, Lord Rayleigh discovered[40] that in fact, the solutions to Maxwell's equations inside hollow tubes *did* describe propagating electromagnetic waves, which exhibited a normal mode structure not dissimilar to familiar resonating structures such as a drumhead. Strangely, this discovery seems to have been ignored until 1936, when it was announced by two independent scientists that they had "discovered" that electromagnetic waves could propagate inside a hollow tube[36] rediscovery), and provided experimental verification of the same - bringing the waveguide into the forefront just in time for the tremendous interest in radar technology that would be brought to bear during the second world war.

The normal modes of a hollow conducting tube of rectangular cross section are labelled as $\mathrm{TE}_{n,m}$ and $\mathrm{TM}_{n,m}$, with the TE or TM designations indicating that the electric or magnetic field is purely transverse to the direction of propagation, respectively. Such a designation is justified because the waveguide modes form solutions to the transverse differential equation

$$\mathbf{E}_t = \pm\frac{ik}{\eta^2}\nabla_t\psi \ \ (\mathrm{TM}) \tag{4.1}$$

$$\mathbf{H}_t = \pm\frac{ik}{\eta^2}\nabla_t\psi \ \ (\mathrm{TE}) \tag{4.2}$$

And $\psi e^{\pm ikz}$ is E_z or H_z for TM and TE modes, respectively.

Because the normal modes of the waveguide form a spectrum, the constant η^2 must be further specified by a label λ that indexes the mode in question, η_λ^2. For a given frequency f, the wavenumber $k_\lambda^2 = 4\pi^2\mu\epsilon f^2 - \eta_\lambda^2$ may be written in terms of a "cutoff" frequency f_λ, defined as the value for which $k_\lambda^2 = 0$:

$$f_\lambda = \frac{\eta_\lambda}{2\pi\sqrt{\mu\epsilon}} \tag{4.3}$$

So that

$$k_\lambda = 2\pi\sqrt{\mu\epsilon}\sqrt{f - f_\lambda} \tag{4.4}$$

At $f = f_\lambda$, the waveguide is said to be "cut off". Note that for a waveguide precisely at cutoff, the equations that describe the fields are those of a cavity resonator - the electric (magnetic) field is in phase for all z positions. Furthermore, for $f < f_\lambda$, the wavenumber is strictly an imaginary quantity, so that the exponential dependence on z rapidly damps the amplitude of the field away from its source. The mode behavior is said to be evanescent for this condition, as the fields decay away[1] from $z = 0$.

Because the wavenumber is a mode dependent quantity, it is possible to operate a waveguide at a frequency where some modes are cut off, while others are propagating. The mode which has the *lowest* cutoff frequency f_λ is called the fundamental (or dominant) mode

[1]Naturally the choice of origin is arbitrary - the expressions may be written in terms of $z = z_0$ without loss of generality.

of the waveguide, and is always the first mode to begin propagating as the frequency is increased from zero. In a rectangular waveguide, the dominant mode is the $\mathrm{TE}_{1,0}$ mode, which has the lowest cutoff frequency of any TE or TM mode. If the waveguide has rectangular dimensions a and b, aligned along the x and y directions respectively (see Figure 4.1 and with $a > b$, then the electric and magnetic fields of the $\mathrm{TE}_{1,0}$ mode are exactly

$$H_z = H_0 \cos\left(\frac{\pi x}{a}\right) e^{ikz - 2\pi i f t} \tag{4.5}$$

$$H_x = \frac{-ika}{\pi} H_0 \sin\left(\frac{\pi x}{a}\right) e^{ikz - 2\pi i f t} \tag{4.6}$$

$$E_y = iH_0 \frac{2\pi f a \mu}{\pi} \sin\left(\frac{\pi x}{a}\right) e^{ikz - 2\pi i f t} \tag{4.7}$$

The cutoff frequency for the $\mathrm{TE}_{1,0}$ mode is obtained by setting $m = 1$ and $n = 0$ in the expression

$$f_{m,n} = \frac{1}{2\sqrt{\mu\epsilon}} \sqrt{\frac{m^2}{a^2} + \frac{n^2}{b^2}} \implies f_{1,0} = \frac{c}{2a} \tag{4.8}$$

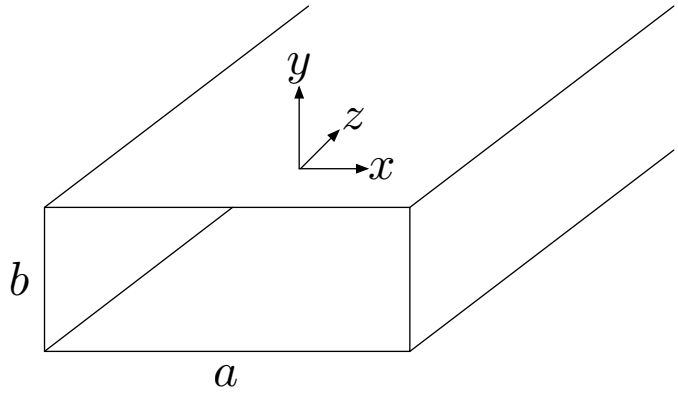

Figure 4.1: A schematic cutaway of a rectangular waveguide.

4.2 Coupling of currents to waveguide modes

Consider a distribution of current $\mathbf{j}(\mathbf{x}, t)$ contained in the interior of a waveguide. For example, the current distribution may be the motion of electrons on the exterior of a probe inserted into the waveguide and excited by a signal. To the left and right of the current

(such that the current is entirely contained by some artificial boundary), the electric fields in the waveguide may be written[28] as

$$\mathbf{E}^{\pm} = \sum_{\lambda'} A^{\pm}_{\lambda'} \mathbf{E}^{\pm}_{\lambda'} \tag{4.9}$$

Where the $A_{\lambda'}$ are expansion coefficients which are to be determined. By a recasting of Poynting's theorem, it may be shown that the expansion coefficients are precisely

$$A^{\pm}_{\lambda} = -\frac{Z_{\lambda}}{2} \int_{V} d^3x \, \mathbf{j} \cdot \mathbf{E}^{\pm}_{\lambda} \tag{4.10}$$

Where Z_{λ} is the impedance of the λ-th normal mode[38]. Viewed this way, the expansion coefficients appear to be a basis expansion for the exciting current $\mathbf{j}$ in terms of the waveguide modes. Consider a single electron in periodic circular motion of frequency f_c about the center of the waveguide, taken to be $x = 0$, $y = 0$, with radius r_c. The current density for this electron may be written as

$$\mathbf{j}_{el}\left(\mathbf{x}, t\right) = e\delta[x - x(t)]\delta[y - y(t)]\delta[z - z(t)] \cdot \dot{\mathbf{x}}(t)$$

Utilizing the previous solution to the equations of motion for an electron in cyclotron motion, we obtain the following time dependent expression for the expansion coefficient of the λ-th mode:

$$A^{\pm}_{\lambda}(t) = -\frac{eZ_{\lambda}}{2} \left[\mathbf{v}_{\perp}(t) \cdot \mathbf{E}_{t,\lambda}\left(\mathbf{x}\left(t\right)\right) \pm v_z\left(t\right) E_{z,\lambda}\left(\mathbf{x}\left(t\right)\right)\right] \tag{4.11}$$

Here the time t is the time in the source (waveguide) frame. For the moment, let us consider an electron which is confined to the xy plane, which is to say $v_3 = 0$. Studying more complicated trajectories requires a detailed knowledge of $\dot{z}(t)$, which we will obtain subsequently in the discussion of trapping and for which the punchline will be that the planar solution is modified by a function of the axial frequency of the electron motion. Given our present restrictions, the position $\mathbf{x}(t)$ can be obtained straightforwardly by integrating the electron EOM, so that for the dominant $\mathrm{TE}_{1,0}$ mode, the coupling coefficients $A^{\pm}$ (dropping the index) are equal to

$$A^{\pm}(t) = -\pi e Z f_c r_c \sqrt{\frac{2}{ab}} \cos\left(\frac{2}{a} r_c \cos\left(2\pi f_c t\right)\right) \tag{4.12}$$

So that the total power radiated down the waveguide in the source frame is

$$P^{\pm}(t) = \frac{\left[A^{\pm}(t)\right]^2}{Z} = \frac{2\pi^2 e^2 f_c^2 r_c^2}{ab}\cos^2\left(\frac{\pi x_0}{a}\right)\cos^2\left(\frac{2}{a}r_c\cos\left(2\pi f_c t\right)\right)$$

An electron with kinetic energy comparable to the endpoint of tritium β decay has a relativistic cyclotron frequency f_c of $27.0094\,\mathrm{GHz\,T^{-1}}$. That same electron has a relativistic Larmor radius r_c of $0.464\,\mathrm{mm\,T^{-1}}$. At the design fields of roughly 1 T, two commercially available waveguide sizes are single-moded: WR28 ($a = 7.112\,\mathrm{mm}$, $b = 3.556\,\mathrm{mm}$) and WR42($a = 10.668\,\mathrm{mm}$, $b = 4.318\,\mathrm{mm}$). The coupling coefficient scales as the inverse square root of the area of the waveguide, and therefore smaller waveguides are more desirable from the standpoint of coupling. Note that this scaling behavior is expected - the normalized magnetic flux enclosed by the electron is larger in a smaller waveguide, and therefore the coupling should be larger. WR42 gives a good tradeoff between coupling strength and cell volume, and is therefore the chosen size for the Project 8 prototype. Taking the value of a to be the waveguide long dimension $a_{42} = 10.668\,\mathrm{mm}$, it is clear that r_c/a is a small parameter and therefore the small angle approximation may be used for the final cosine term.

In the simplest case where the electron orbit is centered on the waveguide cross section, $x_0 = 0$, and thus we have

$$P^{\pm}(t) = \frac{\left[A^{\pm}(t)\right]^2}{Z} = \frac{2\pi^2 e^2 f_c^2 r_c^2}{ab}\cos^2\left(2\pi f_c t\right) \tag{4.13}$$

And of course, the average transmitted power is half of the peak power.

Compare the final time-averaged power transmitted down the waveguide to the total power radiated by a relativistic electron from Equation 1.7 in the case where $\theta = \pi/2$:

$$\frac{P_{\text{waveguide}}}{P_{\text{free space}}} = \frac{\pi^2 e^2 f_c^2 r_c^2}{ab}\cdot\frac{6\pi\epsilon_0}{e^4 B^2} m_e c^2 \frac{1}{(\gamma^2-1)} = \frac{3\pi r_c^2 Z\epsilon_0}{4ab(\gamma^2-1)} = \frac{3Z\epsilon_0}{4ab}\frac{c^2(1-\beta^2)}{16\pi a b f_0^2} \tag{4.14}$$

Where $Z = Z_0\left(1-(f_c/f)\right)^{-1/2}$ is the wave impedance, and Z_0 is the impedance of free space ($377\,\Omega$). A $^{83\mathrm{m}}$Kr conversion electron of $T = 17.8\,\mathrm{keV}$ in WR42 waveguide thus radiates a total power (summing forwards and backwards contributions) which is a factor of 0.55 times less than the total free space radiation. While this does represent a loss of available

signal power, the waveguide has the distinct advantage that the radiation *pattern* is of no consequence - to capture all of the power emitted by a cyclotron electron in free space, it is necessary to instrument the entire 4π solid angle surrounding the electron with perfectly matched antennas. In a waveguide, it suffices to simply capture the power radiated in both directions - and the radiation may be collected efficiently by matching the waveguide to an external circuit e.g. directly into an amplifier.

Note that this only considers the coupling to the dominant $TE_{1,0}$ mode - the total power radiated into all modes may very well be in agreement with the Larmor formula, although at present this is an unknown.

4.2.1 On scaling in a waveguide: an important theorem

It is no happy coincidence that the cyclotron radius of an electron fits comfortably into WR42 waveguide. The wavelength of radiation that is emitted by the electron is

$$\lambda_c = \frac{c}{f_c}$$

The frequency of radiation can be related to the gyroradius of the electron through its velocity:

$$r_c = \frac{mv_\perp}{eB} = \frac{v_\perp}{2\pi f_c}$$

Combining these two, we arrive at a scaling behavior:

$$\frac{r_c}{\lambda_c} = \frac{\beta_\perp}{2\pi} \tag{4.15}$$

The dominant $TE_{1,0}$ mode in a rectangular waveguide is cut off at a critical wavelength λ_{crit}:

$$\lambda_{\text{crit}} = \frac{c}{f_{\text{crit}}} = 2a \tag{4.16}$$

So that cyclotron frequency will radiate if $\lambda_c > \lambda_{\text{crit}}$. Therefore, if the cyclotron wavelength is such that it is above cutoff, (and noting that $\beta \leq 1$) we arrive at an important result:

For any waveguide operated above cutoff, the cyclotron frequency is related to the longest waveguide dimension a by:

$$a > \pi r_c \tag{4.17}$$

4.3 The shorted waveguide detector

The shorted waveguide detector shown below in Figure 4.3 - which is truly the heart of the Project 8 experiment - is a realization of the ideas presented in the previous section. The waveguide detector is fabricated from a section of aluminum WR42 waveguide flange stock 7.62 cm in length and 2.24 cm on a side. The longitudinal axis of the waveguide is oriented along the direction of the background magnetic field **B**. At the top and bottom of this central waveguide section are located specialized flanges that anchor Kapton windows 0.254 mm thick. Between the Kapton windows and the central waveguide section are gaskets made from high purity indium wire 0.760 mm thick. The indium gaskets are fabricated by carefully forming the indium wire so as not to occlude the interior of the waveguide and twisting the wire over itself. The gasket is then crushed by a bolt circle of 4-40 socket-head cap screws made from anodized aluminum, which are retained by the Kapton window flanges.

The Kapton windows themselves contribute negligibly to the signal attenuation in the waveguide. The loss tangent, defined as the ratio of the imaginary (lossy) part of the dielectric constant to the real part, has been measured at NIST [6] to be $\tan\delta = 5.3(10) \times 10^{-3}$. The corresponding RF loss may be correspondingly estimated at approximately 6×10^{-3}dB per window.

The Kapton-indium seal forms a high vacuum seal. Each of the seals was subjected in-place to helium leak testing and found to leak at less than $1.0 \times 10^{-9}\,\mathrm{Pa\,L\,s^{-1}}$. Helium was found to penetrate the seals, the time constant with which the leak checking apparatus

detected the helium gas being consistent with diffusion through the kapton windows rather than mechanical leaking.

Any radioactive gas introduced into the cell is confined by the Kapton windows (up to diffusion) to an isolated region, which has a total volume of $3.5\,\mathrm{cm}^3$. The gas is introduced through two gas ports on the broad wall of the waveguide. These ports consists of a square 3×3 array of 0.4 mm diameter holes. The holes are each 0.254 mm deep, so that the total gas port conductance is $1.35\,\mathrm{L\,s}^{-1}$ per port.

At the bottom Kapton interface, a section of waveguide flange stock known as the "tickler" section is attached. Half way along the total length (1.27 cm) of the tickler section is an extremely weakly coupled (roughly -80dB) port through which RF signals may be introduced. The tickler port serves as a method by which known signals may be injected into the waveguide, but through which only tiny amounts of RF interference can enter due to the extremely poor coupling.

Below the tickler section is a waveguide short. The short is made from a brass plug which has been silver soldered to a stub, so that the total length along the z direction from the geometric center of the central section of the cell to the shorted plane is $7\lambda_g/2$. This length is chosen so that radiation emitted by the electron in the z^- direction will reflect from the short and add constructively at the position of the electron with power which is radiated in the z^+ direction.

As discussed in the section on magnetometry, in the z^+ direction, a small ampoule of 2,2-diphenyl-1-picrylhydrazyl (DPPH) rests directly on the upper Kapton window outside the central waveguide volume. The DPPH is in a sealed Pyrex vessel, approximately 5 mm in length and 1 mm in diameter. Following the DPPH section, there is a very long (1.04 m) section of WR42 waveguide manufactured from OFHC copper which ends in a WR42×WR28 waveguide adapter, which in turn connects directly to the front end of a cryogenic amplifier.

The position of the waveguide detector is maintained at the center of the magnet bore by a short cylindrical section of Teflon with a very slightly smaller radius than the magnet bore itself. A truncated cone at the bottom of the cylinder allows for the insert to be guided into the bore during installation.

4.3.1 Standing Wave Analysis

Because the waveguide is terminated in a short in the z^- direction, radiation emitted in that direction from the z^+ direction will be reflected from the short with a phase shift of $\delta = \pi$. While the transverse field pattern will not be affected by this reflection, the field pattern in the z direction will exhibit standing wave structure. The fields in the waveguide will consist of a sum of two terms - the fields emitted originally in the anterior direction, and the fields which were emitted in the posterior direction but which have reflected from the short and travelled back to the position of the electron.

Neglecting any losses along the reflected path, and assuming that the waveguide is perfectly matched in the anterior direction (so that there is exactly zero reflection in that direction), the fields which are propagating in the z^+ direction may be written as simply

$$E(z,t) = e^{2\pi i f t}\left[E^+ e^{ikz} - E^- e^{ik(z+2z_0)}\right]$$

where z_0 is the distance from the electron position to the short, $E^\pm$ are the initial field amplitudes radiated in each respective direction, and the position of the electron is taken to be $z = 0$. If $E^\pm = E_0$, which is to say that the electron radiates equally in either direction (which is to be expected from our coupling discussion), then

$$E(z,t) = E_0 e^{2\pi i f t} e^{ikz}\left[1 - e^{2ikz_0}\right] \tag{4.18}$$

In the event that $kz_0 = \pi$, there will be perfect phase cancellation at the electron position between the waves which are transmitted in the anterior and posterior directions, and therefore $E(z,t)$ will be identically zero - i.e. no power transmitted. However, if $2kz_0 = n\pi$ for some integer n, the waves will add in perfect constructive interference, and the field

amplitude will be doubled[2]. The transmitted power is therefore

$$\begin{aligned} P(z,t) =& \frac{E_0^2}{Z}\left|1 - e^{2ikz_0}\right|^2 \\ =& \frac{2E_0^2}{Z}\left(1 + \cos\left(2kz_0\right)\right) \\ =& \frac{4E_0^2}{Z}\cos^2\left(kz_0\right) \end{aligned} \tag{4.19}$$

The effective range over which this 3dB enhancement takes place is therefore simply $kz_0 \pm 1/\sqrt{2}$, or roughly 125 MHz for an operating frequency of 26 GHz and constant z_0.

4.3.2 On amplifier loading and waveguide impedance

The total impedance as seen by the amplifier of the series combination of the signal waveguide (taken to be of length ℓ) and the short is given[38] by

$$Z_{\text{in}}(\ell) = Z_{\text{wg}}\left[\frac{Z_{\text{s}} + iZ_{\text{wg}}\tan\left(\beta\ell\right)}{Z_{\text{wg}} + iZ_{\text{s}}\tan\left(\beta\ell\right)}\right]$$

Assuming an ideal short with $Z_{\text{s}} = 0$, the input impedance as seen by the amplifier should be

$$Z_{\text{in}}(\ell) = iZ_{\text{wg}}\tan\left(\beta\ell\right) \tag{4.20}$$

If the waveguide were lossless, then Z_{wg} would be purely real and the amplifiers would see a pure reactance from the short. However, in the presence of conductor loss the waveguide impedance of the TE mode can be written

$$Z_{\text{TE}} = \frac{2\pi f\mu}{\alpha_c^2 + \beta^2}\left(\beta + i\alpha_c\right) \tag{4.21}$$

Where the conductor loss α_c is measured in $\text{dB}\,\text{m}^{-1}$. As will be reported in the receiver section, the loss of the waveguide has been measured at -2.7 dB, and given the waveguide length of 1.0414 m, α_c can be estimated at $2.6\,\text{dB}\,\text{m}^{-1}$. The impedance is therefore:

$$Z_{\text{wg}} = Z_{\text{TE}} \approx 448 + 1.5i\,\text{Ohm} \tag{4.22}$$

---

[2] Actually, there is a subtlety to this point. Because the frequency of the electron is actually changing, the fields which are emitted in the posterior direction and subsequently reflect are added to waves which are emitted in the anterior direction with a very slightly different frequency. As long as the path length to the short is small, so that the time delay is small compared with the rate of change of the electron frequency, this correction can be safely neglected.

The amplifiers therefore see a highly reactive load of magnitude Z_{wg}. This could be transformed to a purely resistive load by the addition of a parallel reactance, and would allow perfect matching of the amplifiers to the waveguide. A small stub tuner at the position of the WR42 x WR28 taper would accomplish this nicely.

4.4 Gas Delivery Lines

The gaseous species under study (e.g. $^{83\mathrm{m}}$Kr) is delivered to the central waveguide cell by means of long stainless steel tubes, referred to as the gas lines. The lines were manufactured by Nor-Cal industries using semiconductor grade materials and with additional mechanical and solvent based cleaning performed after construction. The tubes have short stainless steel bellows welded to the ends to accomodate mechanical tolerances associated with centering the central waveguide in the magnet bore and the shrinking that occurs during cooling of the insert.

The gas lines run down the bore of the magnet on either side of the long waveguide that connects the waveguide cell to the cryogenic amplifiers. At low pressures, Kr gas will be efficiently cryopumped at temperatures less than 100 K, as shown below in Figure 4.4. The data shown relate the temperature of the waveguide cell in degrees K to the integral of observed counts in a Si detector, which was monitoring the source radioactivity in the gas system.

To prevent freezing of the krypton on the interior of the gas lines, each line is wrapped with Kapton tape impregnated with heating elements. The heaters are used both to bake the gas lines mildly and to maintain their temperature (if need be) above 100 K.

The tops of the gas lines are welded to 1.33-inch rotatable Conflat flanges that mate via high vacuum feedthroughs to the rest of the gas system. The bottoms of the gas lines near where the lines meet the waveguide cell are terminated in Swagelok 1/2 inch female VCR glands. After the VCR joint, the lines are fabricated from OFHC copper to minimize any diamagnetic effects of the gas lines on the field near the trap region. A custom gas fitting fabricated from OFHC copper connects the gas lines to the waveguide cell via indium wire

seals.

4.5 Cryogenics

To reduce the thermal background noise at the input to the cryogenic amplifiers, the insert is maintained at as low a temperature as possible without freezing out the source gas. A Cryomech AL-60 Gifford-McMahon style cryocooler is installed at the topmost vacuum feedthrough flange. The main responsibility of this cryocooler is maintaining the amplifiers at a temperature of roughly 30 K, but it is also used to cool the rest of the insert. A large busbar made from OFHC copper runs the full length of the insert, and transports heat up to the coldhead.

This design satisfies the requirement that the gas lines not be cooled below 100 K, but could be improved with additional cooling power. The current design is able to maintain the waveguide at a temperature of roughly 200 K. This factor of two in physical temperature would have a noticable impact on the noise floor of the experiment, as elaborated on in the section on receiver noise (Section 5.5). In addition, while the cell must be warm enough so that krypton will not freeze, the fiducialization afforded by the Kapton windows allows the rest of the experiment to be maintained at a much cooler temperature, which additional cooling power would allow.

4.6 The trapping coil

A conversion electron created in the central waveguide section with a pitch angle θ not precisely equal to $\pi/2$ will move in the z direction and strike one of the Kapton windows in short order. For even a modest complementary pitch angle of $\phi = 1 \times 10^{-3}$, the time for an electron to collide with the Kapton at the end of the central section is less than 0.5 µs. Therefore, in order to satisfy the requirement on electron observation time, a short solenoid is wound on the detector insert in order to provide a trapping potential.

4.6.1 Effective Trapping Volume

The minimum pitch angle $\theta_{\min}$ which is trapped by a given field distribution is actually a function of the z position in the trap. For a gaseous radioactive source, electrons will be produced uniformly w.r.t. solid angle, and therefore at any given z position, the fraction of electrons produced at that z position with a pitch angle greater than $\theta_{\min}$ will be trapped. The relationship between this observation and the fraction of emitted electrons which are trapped may be quantified by defining an "effective" trapping volume V_{trap}, which is simply a weighted volume integral:

$$V_{\text{trap}} = \int_V d^3x \, \frac{\Omega(\mathbf{x})}{4\pi}$$

Where $\Omega(\mathbf{x})$ is the total solid angle which is trapped at a given position, and the volume integral is carried out over the physical extent of the trap. In the case that *all* solid angles everywhere are trapped, then $\Omega(\mathbf{x}) = 4\pi$, and V_{trap} is simply equal to the physical volume of the trap.

4.6.2 Effective trapping volume of the solenoidal trap coil

The trapping magnet in the Project 8 demonstrator is formed by a short solenoidal coil. The waveguide stock from which the waveguide cell is formed is turned down to a cylindrical cross section onto which a solenoidal coil is wound. This solenoid is of length $L = 7.62\,\text{mm}$ and radius $a = 6.5\,\text{mm}$. The coil is designed so that the axial field gradient is about $10\,\text{mT}^2\,\text{cm}^{-1}$. The effect of this additional magnetic field component is discussed in a following section.

On the z-axis, the field due to the solenoid may be written as

$$B(z) = B_0 \left[\frac{z + \frac{L}{2}}{\sqrt{(z + \frac{L}{2})^2 + a^2}} - \frac{z - \frac{L}{2}}{\sqrt{(z - \frac{L}{2})^2 + a^2}} \right]$$

So that for an electron born at $z = z_0$, the field it experiences is $B(z_0)$, and the electron must have a pitch angle greater than

$$\cot(\theta) \geq \sqrt{\frac{B_\infty}{B(z_0)} - 1}$$

where of course B_∞ is the maximum field which occurs outside the trap [3] . Therefore the trapping volume for the solenoidal trap is

$$V_{\text{trap}} = \int_0^{2\pi} \int_0^{\pi} \int_{z_{\min}}^{z_{\max}} dz\, d\cos(\theta)\; d\phi \frac{\Omega(\mathbf{x})}{4\pi}$$

The integral over the azimuthal angle ϕ is trivial. The integral over θ will only contribute in the range $[\theta_{\min}, \pi/2 + \theta_{\min}$. Because the integrand is symmetric w.r.t. the induced limits, we can integrate over half the range and double the result. The final integral is then

$$V_{\text{trap}} = \int_{z_{\min}}^{z_{\max}} \int_{\theta_{\min}(z)}^{\pi/2} d\cos(\theta)\; dz \tag{4.23}$$

When evaluated with parameters from the solenoidal trap, the result is a trapping volume of approximately $1.5\,\text{mm}^3$.

[3] In general, B_∞ would be replaced with the maximum field which is attained by the combination of the background field and the trap field. For traps such as the solenoidal trap which lower the local magnetic field, the field at "infinity" is the background field, which is the right field to use.

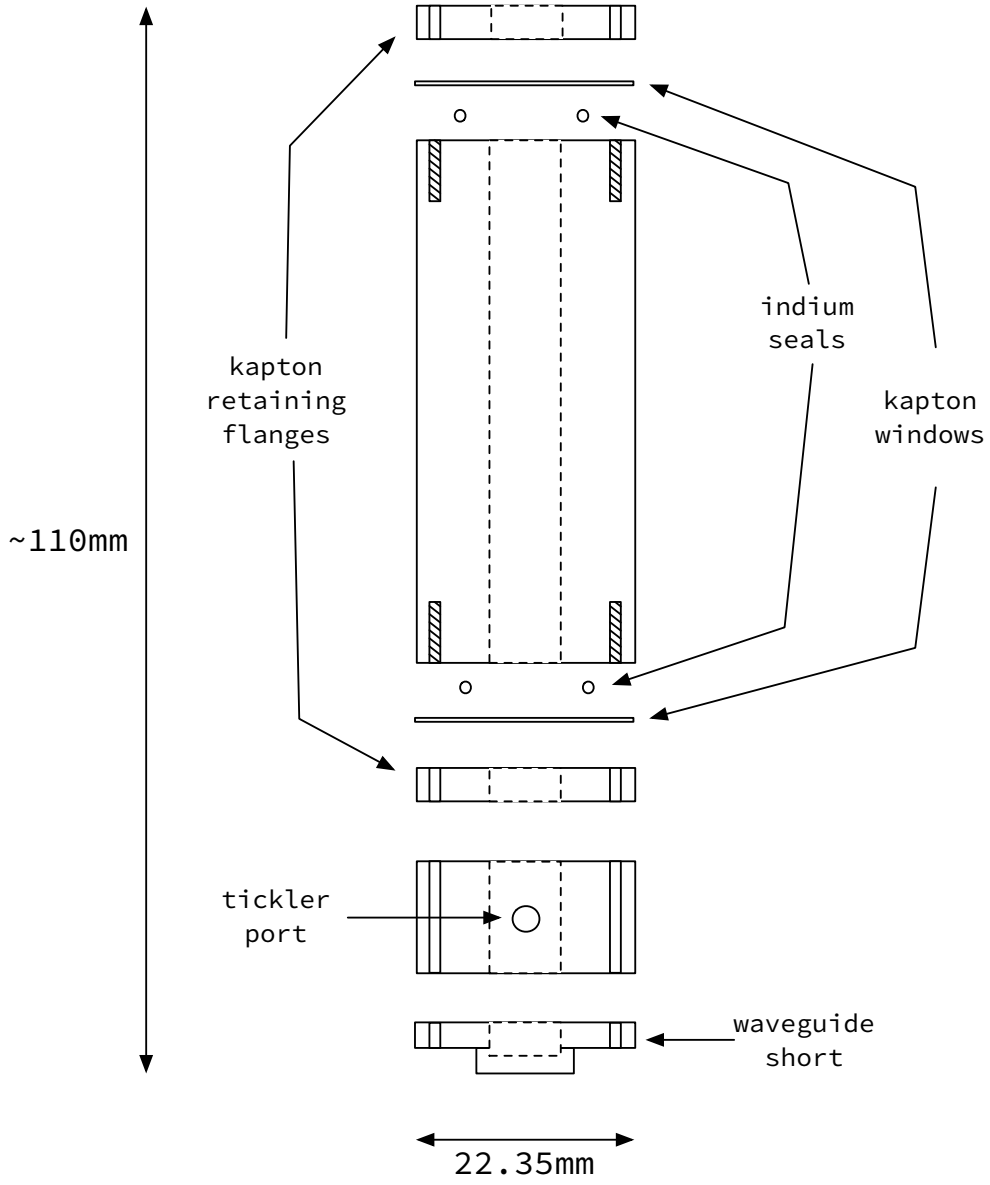

Figure 4.2: A schematic view of the waveguide detector as sliced through the z-plane. The y axis points out of the page, so that the dashed lines are the outline of the broad wall of the waveguide.

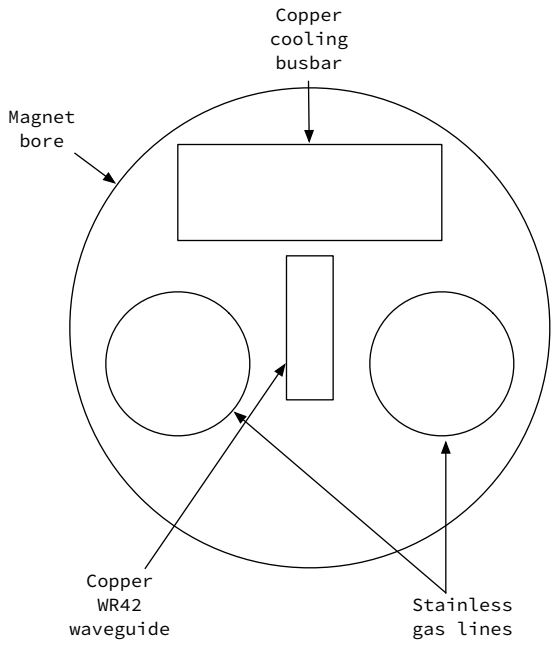

Figure 4.3: A schematic slice through the magnet bore transverse to the field axis, showing the layout of the gas lines, the cooling components, and the waveguide.

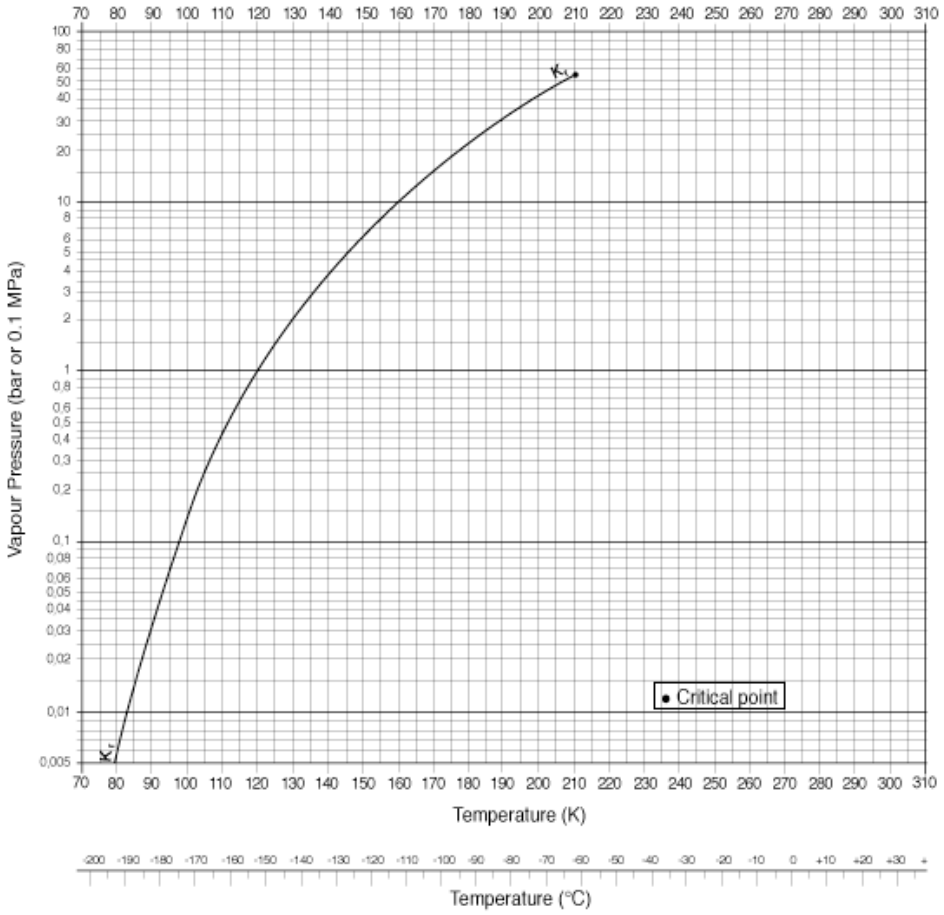

Figure 4.4: Measured vapor pressure for krypton over a wide temperature range [1].

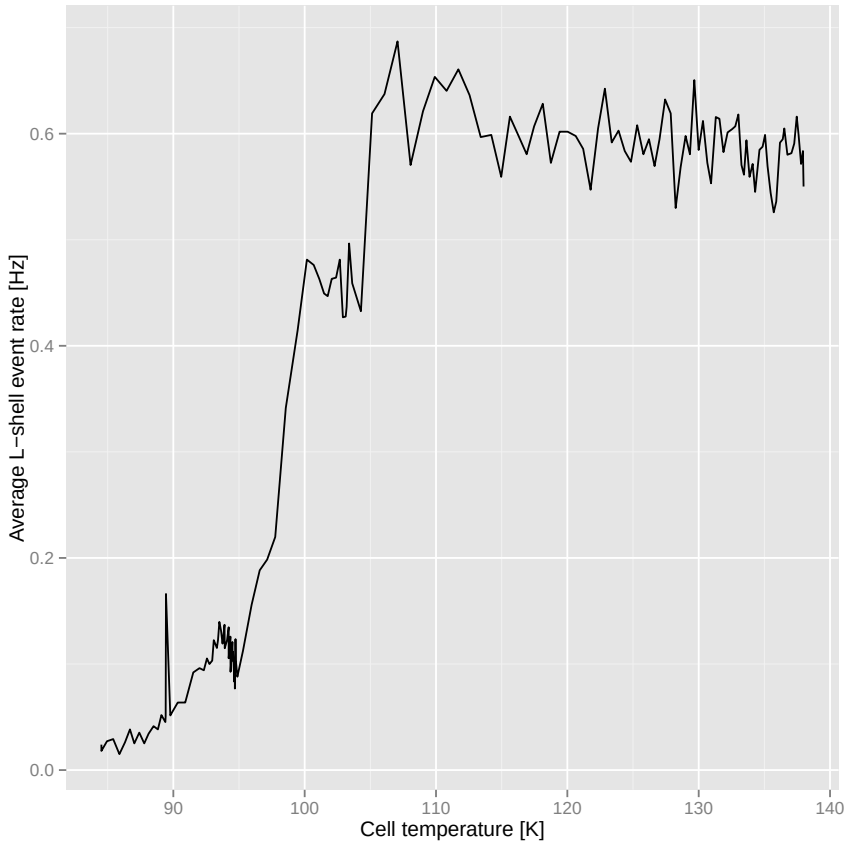

Figure 4.5: The L-shell activity as monitored on the PIPS detector while the temperature of the waveguide cell was varied in the vicinity of the boiling point of krypton. A transition is seen to occur around 100 K. The average rate was measured by integrating the total observed L-shell decays for 900 s at each data point. The expected doubling of rate over the temperature range 90 K to 100 K is to be expected from the data in Figure 4.4. Saturation of the rate occurs at around 110 K as the source is not an infinite reservoir.

Chapter 5

RECEIVER

5.1 Receiver noise

Noise performance is a critical component of a discussion on receiver performance. For a given signal input power P, the noise temperature of the receiver T_r determines the maximum output signal to noise ratio $\mathcal{S}_{\text{out}}$:

$$\mathcal{S}_{\text{out}} = \frac{P}{P_{noise}} = \frac{P}{k_B \nu T_r}$$

where ν is an appropriately chosen bandwidth. It is obvious that optimizing $\mathcal{S}_{\text{out}}$ is of utmost importance for the analysis of signals.

As will be shown below, the noise temperature of the receiver is essentially determined by the noise temperature of the first component in the receiver cascade. Components downstream of those initial components contribute negligibly, provided the gain of the initial components is sufficiently large[1].

Consider two electronic components of gain G_0 and G_1, with noise temperature T_0 and T_1, respectively. If the output of component 0 is connected to the input of component 1, as shown in Figure 5.1, a natural question to ask is what the *lumped* gain and noise temperature are for the cascaded components.

---

[1] A good rule of thumb is that the noise temperature of the first component will be the noise temperature of the cascade until lossy components overwhelm its gain.

Figure 5.1: A simple two component RF cascade.

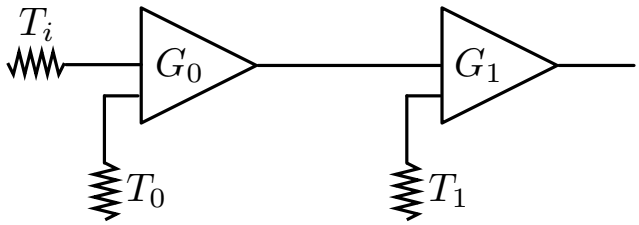

The analysis of this cascade is simple. The input noise power density at the first component input is simply $k_B T_i$, so the output noise power density is given by $G_0 (T_0 + T_i)$. With this expression as the input to the second component, we find that the cascade output noise power density is $G_1 (G_0 (T_0 + T_i) + T_1)$. Because we are interested in the "lumped component" formed by the two components in cascade, we seek an expression in the form of $G_c (T_i + T_c)$, where the index c indicates cascaded quantities.

Simply factoring out a factor of G_0 from the expression for the output noise power density, and setting this equal to the cascaded expression, we arrive at

$$\begin{aligned} G_c (T_i + T_c) = &\quad G_0 G_1 \left(T_0 + T_i + \frac{T_1}{G_0} \right) \\ \therefore G_c = &\quad G_0 G_1 \qquad (5.1) \\ T_c = &\quad T_0 + \frac{T_1}{G_0} \qquad (5.2) \end{aligned}$$

In particular, for N components which are cascaded, the overall gain is given by

$$G_c = \prod_i^{N-1} G_i \qquad (5.3)$$

And the cascaded noise temperature is given by

$$T_c = T_0 + \sum_{i=1}^{N-1} \frac{T_i}{\prod_{j=0}^{i-1} G_j} \qquad (5.4)$$

Note in the above expressions the grave effect of having $G_0 < 1$: the temperature of the second component in the chain is actually magnified rather than mitigated. It is therefore

very important to minimize any losses before the gain stage of the receiver to make this effect as small as possible.

The Project 8 receiver has been designed in such a way that the first components in the receiver cascade have very low noise temperature and very high gain. Subsequent components have been chosen functionally, but with less regard to noise and gain performance. The components, their connectivity, and functionality are described below in terms of functionally distinct *stages* - a cryogenic input stage, a high frequency heterodyne stage, and a low frequency heterodyne stage.

The overall receiver architecture is a broadband superheterodyne.

5.2 Receiver gain and bandwidth

The voltage output of the receiver is discretely sampled in time with sampling period $\mathcal{T}_s$ and converted to a digital representation by an analog to digital converter, where the n'th voltage sample taken at time $n\mathcal{T}_s$ is represented as

$$s_n = \frac{s(n\mathcal{T}_s) - V_-}{V_q}$$

where V_q is the quantization voltage $V_{FS}/2^N$, and N is the number of bits of the ADC. The design of the receiver must fulfill two separate requirements:

- The overall gain of the receiver should be such that the signal voltage at the output of the receiver should be greater than some multiple of the quantization voltage: $v_s \geq s \cdot V_q$.

- The overall gain of the receiver should be sufficiently small that the r.m.s. noise voltage at the output of the system is smaller than some fraction of the full-scale voltage, so as not to consistently saturate the ADC: $v_n < d \cdot V_{FS}$.

Let the overall linear power gain of the receiver be G, such that for a given input power P_{in}, the power at the output of the receiver is $P_{\text{out}} = GP_{\text{in}}$. Then the quantities v_n and v_s

may be related to the gain of the receiver:

$$P_{\text{out}} = GP_{\text{in}} \implies v_{\text{out}}^2 = Gv_{\text{in}}^2$$

$$\therefore \quad \sqrt{G}v_{n,0} < d \cdot V_{FS} \tag{5.5}$$

$$\sqrt{G}v_{s,0} \geq s \cdot V_q \tag{5.6}$$

Where $v_{i,0}$ is the i'th voltage (signal or noise) present at the input of the receiver. Let $\sigma_v = \frac{v_{s,0}}{v_{n,0}}$ be the input voltage signal-to-noise ratio. Then eliminating the input signal voltage in terms of the quantity $\sigma_v v_{n,0}$ and rearranging, we may express the above in terms of an inequality involving G:

$$\left(\frac{s}{2^N \sigma_v}\right)^2 \left(\frac{V_{FS}}{v_{0,n}}\right)^2 \leq G < d^2 \left(\frac{V_{FS}}{v_{0,n}}\right)^2$$

$$\left(\frac{s}{\sigma_v 2^N}\right)^2 \leq \frac{G}{g^2} < d^2 \tag{5.7}$$

Where the 'gain' g relates the input noise voltage to the full-scale voltage of the ADC and is defined as $g = (V_{FS}/v_{0,n})^2$

Shown in Figure 5.2 is an example of the allowed region for the total gain for a fictitious situation where $s = 10$, $N = 8$, and $d = 0.6$. In the left pane, the signal-to-noise ratio $\sigma_v = 0.1$, whereas in the right panel, $\sigma_v = 0.075$. As expected, more gain is needed for the lower value of σ_v, but the total gain budget is set by d, which is constant between the two panels.

If the input noise voltage $v_{0,n}$ is treated as generated by a noisy resistor at some non-zero temperature T of resistance R, then we may write the noise voltage as

$$v_{0,n}^2 = 4k_B T R \nu \tag{5.8}$$

where k_B is Boltzmann's constant, and ν is the bandwidth over which we are considering the noise. For our purposes here, ν may be taken to be the frequency space width of the *narrowest* filter in the receiver, which is to say ν is the width of the interval in frequency space over which the power spectral density of the input noise is nonzero[2]. We may then

[2]A more thorough statement is that ν is the equivalent width of a truly white spectrum

Figure 5.2: The allowed gain region for an example receiver. Note that as the ratio g increases (implying a lower input noise voltage), the allowed region for G is larger. For the left pane, $\sigma_v = 0.1$. In the right pane, $\sigma_v = 0.075$.

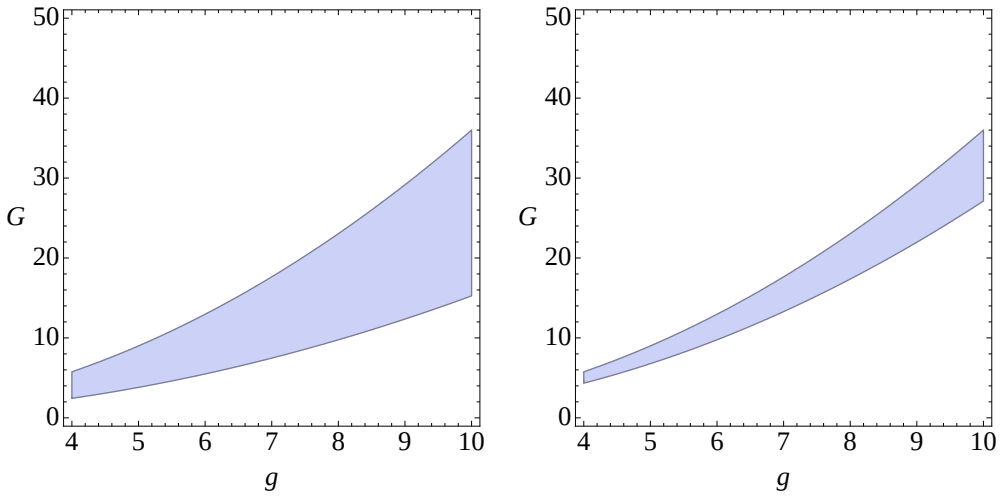

re-write our inequality in terms of this quantity:

$$\left(\frac{s}{\sigma_v 2^N}\right)^2 \leq \frac{\nu G}{g_0^2} < d^2 \tag{5.9}$$

Where now g_0 is the noise voltage *per hertz*. With this reparameterization, it is clear that the quantity that is constrained is not just G, but the bandwidth-gain product BG. Therefore, we have arrived at a system of constraints that will allow us to design the receiver to satisfy simultaneously the requirements that the output signal level be of a sufficient amplitude, while not saturating the input to the ADC:

- s - the desired ratio of the input signal voltage to the quantization voltage of the ADC.
- σ_v - the voltage signal-to-noise ratio. This parameter is determined by the conditions of the experiment, as outlined below.
- N - the number of bits of the ADC.
- g_0 - the noise voltage density. This parameter is also determined by the conditions of the experiment, as outlined below.

- d - the desired ADC input noise voltage, in units of the full-scale voltage of the ADC.

Once the above parameters are determined, it remains only to choose BG such that the inequality 5.9 is satisfied.

5.3 Receiver Stages

5.3.1 Cryogenic Input Stage

The cryogenic input stage consists of two cascaded LNF-LNC22_40WA low noise amplifers manufactured by Low Noise Factory. The amplifiers are specified at a physical temperature of T_{amb} =12 K to have a noise temperature of T =14 K. The gain of the amplifiers is 28 dB at T_{amb} =12 K, and being only 2 dB greater than the same figure at T_{amb} =300 K is relatively insensitive to temperature.

Figure 5.3: Gain and temperature data taken from the LNF-LNC22_40WA datasheet.

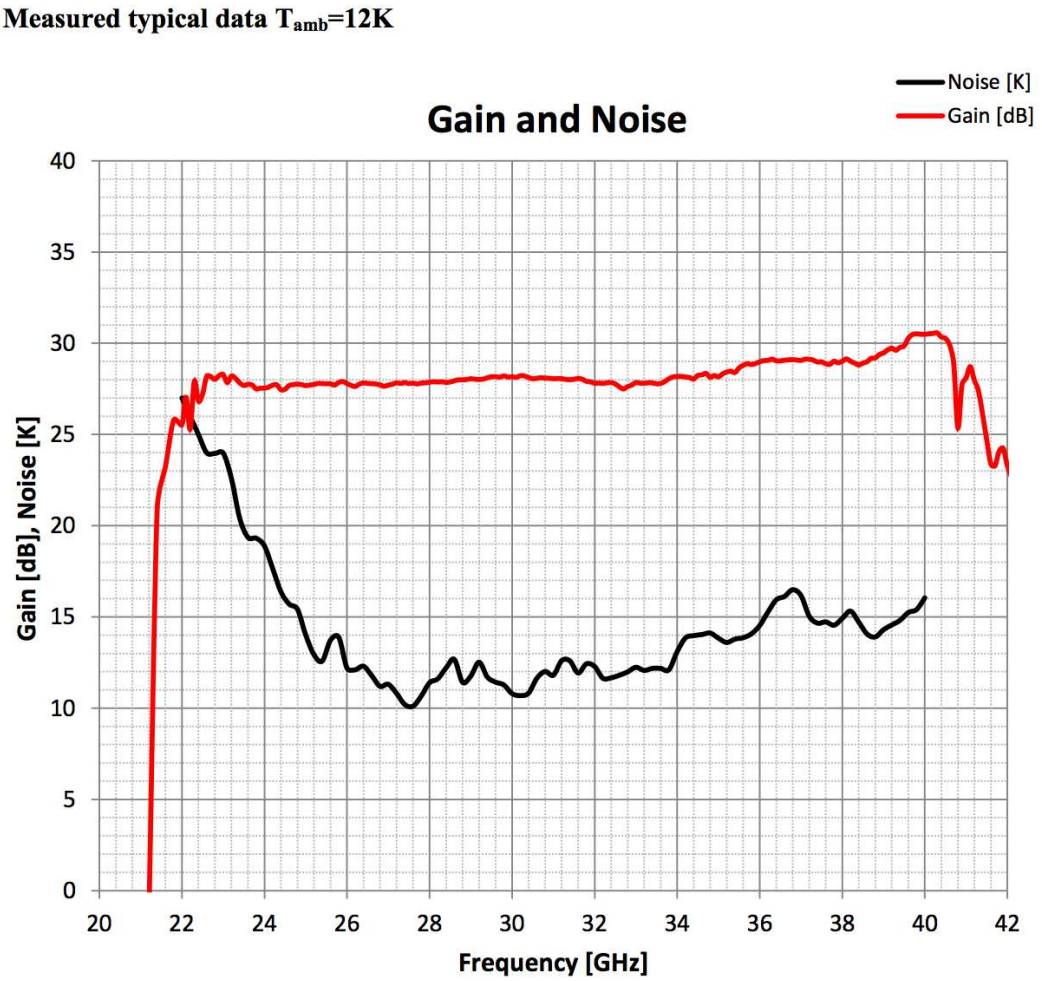

The amplifier input and output are WR28 waveguide ports, as seen in Figure 5.3.1. A single 9-pin Micro-D connector provides ground, bias monitoring, and the single gate and drain supply. Physically the amplifiers are quite small, measuring only 34.3 mm ×40 mm ×19.7 mm. The two amplifers are joined by a 7.62 cm section of WR28, the interior of which is flashed with gold.

The input of the cryogenic stage is a WR42×WR28 cryogenic taper from Quinstar. The output is a WR28×2.92 mm cryogenic adapter, also manufactured by Quinstar.

Figure 5.4: A picture of one LNF-LNC22_40WA cryogenic amplifer. Picture is courtesy of the LNF datasheet for the part.

5.3.2 High Frequency Heterodyne

The high frequency heterodyne stage, or HF stage, is designed to downconvert the K band output from the cryogenic preamplifier stage to an intermediate frequency in the L band.

Figure 5.5: A block diagram of the HF downconverting receiver.

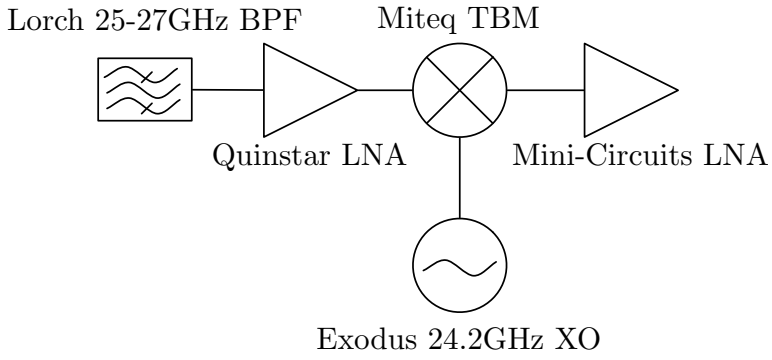

The frequency conversion is accomplished by a Miteq TB0426LW1 triply balanced mixer.

The LO port is driven by an Exodus Dynamics EDPLO-3000-24.20 phase locked oscillator, phase locked to an external Exodus Dynamics 100MHz Oven Controlled Crystal Oscillator (OCXO-501-04516W-100.00). The nominal frequency of the PLO is 24 200 MHz, and its output power is 15 dBm. Before the RF port is a Lorch 4EZ7-260002000-S bandpass filter, with a 3 dB passband between 25 000 MHz and 27 000 MHz. Between the filter output and the mixer RF input, a Quinstar QLW-18262530-J0 low noise amplifier compensates for cable and filter insertion losses between the cryogenic preamplifier stage, as well as the conversion losses from the mixer.

The IF output of the mixer is amplified by a Mini-circuits ZX60-3018G-S+ amplifier with a nominal gain of 30 dB.

Figure 5.6: The passband of the RF (green) and IF (blue) stages of the high frequency receiver. The stages are defined as pre and post-mixer, respectively. The local oscillator of the first stage is set at 24 200 MHz.

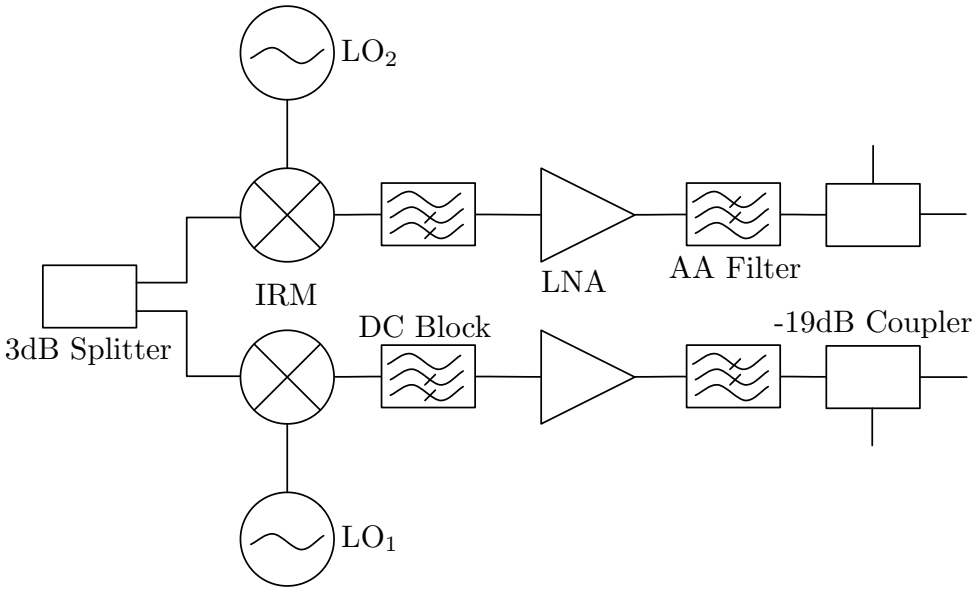

5.3.3 Low Frequency Heterodyne

The low frequency heterodyne stage (LF stage) is designed to downconvert the L band output from the HF stage to a final working frequency band between DC and the middle of the VHF band (100 MHz).

Figure 5.7: A block diagram of the HF downconverting receiver. The LF receiver consists of two independent channels whose RF input is identical. The two oscillators LO_1 and LO_2 may be set to different values to allow recording of two passbands simultaneously.

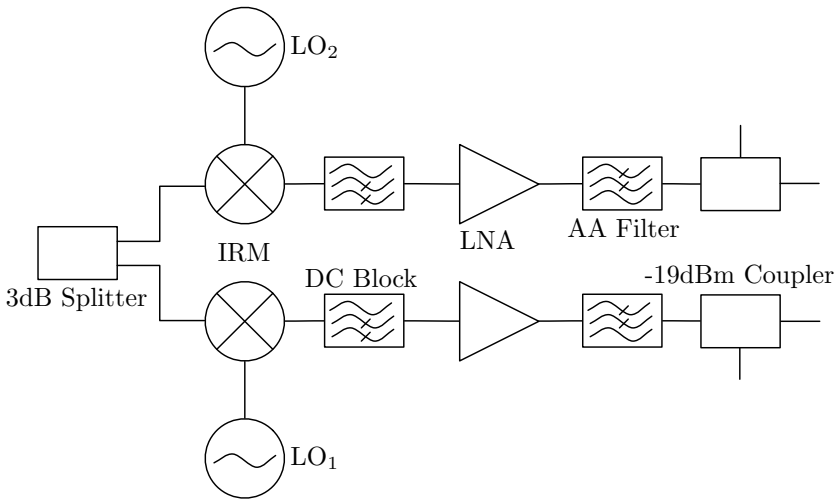

The LF stage consists of not one but two separate receivers, which are referred to as channels. Each channel has an input fed by a 3 dB splitter, so that the RF input to the two channels is identical modulo an overall phase (or time delay). The local oscillator for each channel is independent, so that if two different LO frequencies are chosen for the two channels, the two outputs will be independent subbands of the RF input, as shown in Figure 5.8.

The input splitter is a Mini-Circuits ZFRSC-42-S+. The mixers that receive the splitter outputs are both Polyphase Microwave IRM0622B image-reject mixers (IRM), which have been selected with a 30 MHz to 90 MHz image rejecting output band. The local oscillators $LO_{1,2}$ are external sources, which are configured to drive each IRM at P_{LO} =13 dBm.

Figure 5.8: If two different frequencies are chosen for the local oscillators, the effect of the low frequency passband filters is to select two separate 100MHz subbands of the RF input passband. This may be used to monitor two separate signals simultaneously, e.g. the 17.8 keV and 30.2 keV lines.

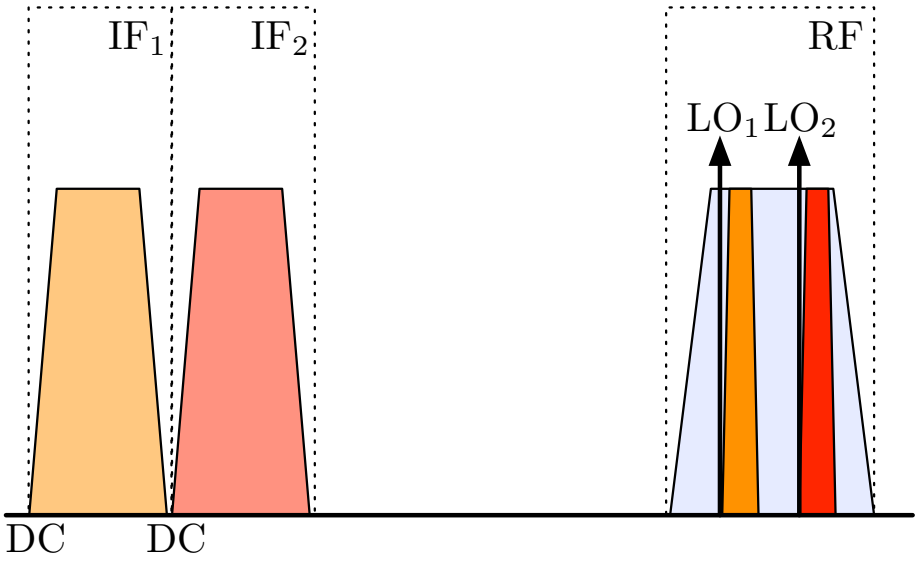

The post-mixing amplifer is a Mini-Circuits ZX60-3018G-S+, and the bandpass filtering is accomplished with a combination of a Mini-Circuits ZFHP-0R055-S+ and a Mini-Circuits SLP-90+ such that the output passband is 70 kHz to 90 MHz. The directional couplers are Mini Circuits part number ZX30-17-5-S+, and are used for diagnostic purposes.

5.4 Digitizer

Recording of signals at the output of the receiver chain from trapped electrons is performed with a Tektronix Real-Time Spectrum Analyzer (RSA) model RSA5106B. A frequency domain mask (FDM) trigger is generated by the instrument, which establishes a threshold based on absolute signal power in a given frequency band. The FDM causes the instrument to trigger if a signal of sufficient power is detected in the frequency band of interest. Upon triggering, the instrument records time-series data to disk for a fixed period of 5 ms, starting 1 ms before the trigger event. The data produced are IQ data that are sampled at a variable

rate depending on the chosen resolution bandwidth (RBW), so that the Nyquist criterion is always satisfied.

5.5 Receiver Analysis

A tabulation of the contribution of each component to the overall gain G_r and noise temperature T_r of the receiver follows. For components that have been measured (indicated with a †), experimental quantities are quoted. Figures with a $*$ are calculated from theory, and unmarked entries are from specification sheets. Shown measurements were performed by either the author or Jonathan Tedeschi (PNNL).

The total system noise temperature was measured by carefully calibrating the overall gain of the receiver components between the cell and the amplifiers, including the waveguide. The tickler port was calibrated relative to a matched 2.7mm to WR-42 adapter. A signal of known power was then injected into the tickler port. The output amplitude of this tone was monitored on a spectrum analyzer, and the noise floor amplitude measured relative to the peak. The figure so obtained by Jonathan Tedeschi is 145 K, and has a likely error of 1 or 2 decibels due to gain calibration errors.

5.5.1 Passive Components

The gain G of a passive component is defined to be the inverse of its insertion loss[38], so that if the insertion loss of a component is specified in decibels, the gain is obtained by simply flipping the sign of the insertion loss.

The noise temperature T_n is determined from both the insertion loss (or equivalently its gain) and its physical temperature T:

$$T_n = T\left(10^{G/10} - 1\right) \tag{5.10}$$

Component	T_i	G_i	ν_i	T_r	G_r	ν_r
Signal Waveguide†	47.75 K	-1.2 dB	14 GHz to 28 GHz	47.75 K	-1.2 dB	14 GHz to 28 GHz
WR42/WR28 taper	1.75 K	-0.1 dB	14 GHz to 40 GHz	50.04 K	-1.3 dB	14 GHz to 28 GHz
LNF Amp 1(T=11 K)	14 K	28 dB	22 GHz to 40 GHz	68.93 K	26.7 dB	14 GHz to 28 GHz
WR28 Standoff	0.4 K	-0.05 dB	22 GHz to 40 GHz	68.95 K	26.65 dB	14 GHz to 28 GHz
LNF Amp 2	14 K	28 dB	22 GHz to 40 GHz	69 K	54.65 dB	14 GHz to 28 GHz
WR28/K adapter	2.5 K	-0.3 dB	22 GHz to 40 GHz	69 K	54.35 dB	14 GHz to 28 GHz
Adapter to bulkhead cable	216.23 K	-5 dB	22 GHz to 40 GHz	69 K	49.35 dB	14 GHz to 28 GHz
Bulkhead feedthrough	300 K	-3 dB	14 GHz to 28 GHz	69 K	46.35 dB	14 GHz to 28 GHz
Bulkhead to receiver cable	1593 K	-8 dB	22 GHz to 40 GHz	69 K	38.35 dB	14 GHz to 28 GHz
Lorch Bandpass Filter	650 K	-5 dB	25 GHz to 27 GHz	69.1 K	33.35 dB	25 GHz to 27 GHz
Quinstar amplifier†	226 K	32.7 dB	18 GHz to 26.5 GHz	69.1 K	66.05 dB	25 GHz to 27 GHz
Miteq TBM†	2700 K	-10 dB	1 MHz to 3000 MHz	69.2 K	56.2 dB	800 MHz to 2800 MHz
Mini-circuits amp†	250 K	22.7 dB	1 MHz to 3000 MHz	69.2 K	78.75 dB	800 MHz to 2800 MHz

Figure 5.9: Tabulated gain and noise parameters for all components of the Project 8 receiver.

Chapter 6

DATA COLLECTION AND ANALYSIS

6.1 Expected Electron Signal

The conversion electrons which are the object of the Project 8 experiment must be trapped via the introduction of a magnetic inhomogeneity. Consequently, the cyclotron frequency of those electrons is a time dependent quantity, changing as a consequence of the motion of the electrons in the nonuniform field:

$$f_c \rightarrow f_c(t) = \frac{1}{2\pi}\frac{e}{m}\frac{B\left[\mathbf{x}(t)\right]}{\gamma\left(t\right)}$$

The electron signal as observed by the receiver (up to an overall phase) is expected to be of the form:

$$s(t) = Ae^{i\phi(t)t} = V_0 e^{2\pi i \int dt'\, f_c(t')} \tag{6.1}$$

In order to predict the exact characteristics of this signal, the detailed trajectory of the electron $\mathbf{x}(t)$ must be known. This requires a solution to the equations of motion for the electron in the combination of the constant background magnetic field with the magnetic bottle coil superimposed:

$$\mathbf{B}\left(\mathbf{x}\right) = B_0\hat{z} + \mathbf{\Delta B}\left(\mathbf{x}\right)$$

6.1.1 Signal due to solenoidal trapping coil

Near the center of the solenoidal trapping coil (where we will set $z = 0$) the leading order expansion of the total field in powers of z is a quadratic term[1]. Consequently, we expect that the field due to the trap coil along the z axis can be written approximately as:

$$\Delta B(z) \approx \Delta B(1 + a^2 z^2)$$

[1] As it of course should be, due to the symmetry of the current distribution.

where a is an inverse length scale that characterizes the second derivative of the field near $z = 0$. This simple form is unappealing from a physical perspective because it fails to satisfy both $\nabla \cdot \mathbf{B} = 0$ and $\nabla \wedge \mathbf{B} = 0$, which are the constraints imposed by Maxwell's equations in a current-free region. To restore compliance with these constraints, we must introduce dependence on the radial coordinate ρ as well. Introducing the lowest-order terms involving ρ that are possible, the total solenoidal field may be written approximately [2] in cylindrical coordinates as

$$B_z = \Delta B \left[1 + a^2 z^2 + \frac{a^2}{2}\rho^2\right] \tag{6.2}$$

$$B_\rho = -a^2 \Delta B z \rho \tag{6.3}$$

and thus the equations of motion from the Lorentz force law can be written as:

$$\frac{m_e}{e}\ddot{\rho} = \dot{\theta}\left[B_0 + \Delta B\left(1 + a^2 z^2 + \frac{a^2}{2}\rho^2\right)\right] \tag{6.4}$$

$$\frac{m_e}{e}\ddot{\theta} = \Delta B a^2 \rho z \dot{z} - \dot{\rho}\left[B_0 + \Delta B\left(1 + z^2 + \frac{1}{2}\rho^2\right)\right] \tag{6.5}$$

$$\frac{m_e}{e}\ddot{z} = \Delta B a^2 \rho z \dot{\theta} \tag{6.6}$$

Unfortunately an analytic solution to these EOM is not apparent. In analogy with the theoretical results[3] for geonium[9], the qualitative features of the motion are expected to be:

- Cyclotron motion of the electron in a plane perpendicular to the total field.
- A "slow" periodic motion of the center of the cylotron motion (the so-called guiding center[34]) about the axis of symmetry of the magnetic field. This motion is called the magnetron motion and its frequency f_m is expected to be much smaller frequencyw than the cyclotron motion.

[2] Notably, this same expansion may be reached by computing the lowest order terms which contain nontrivial z and ρ dependence in a Taylor expansion of the magnetic field due to a solenoidal coil near its center.

[3] The author is suspicious that using the solutions for the EOM of geonium[9] in a Penning trap as an Ansatz, the answer may be obtainable. Indeed, I have discovered a truly marvellous proof of this, which this footnote is too narrow to contain.

- A harmonic oscillation of the guiding center in the z direction due to the quadratic character of the trapping field. The frequency f_a of this axial motion is expected to lie in between the two other frequencies of motion: $f_c >> f_a >> f_m$.

Despite the unavailability of an exact solution in the general case, a great deal of information can be had by considering the simple harmonic case, where the axial and cyclotron motions may be solved exactly for small oscillations about the center of the coil and where the radial component of the field is neglected.

Consider the case where the guiding center of the electron is taken to be on the axis of symmetry $x = y = 0$, and where the Larmor radius of the electron is very small i.e. the limit in which $\rho \to 0$. Then the total field can be written in terms involving only z:

$$\mathbf{B}(z) = B_0 \left[1 + \frac{\Delta B}{B_0}(1 + a^2 z^2)\right) \tag{6.7}$$

$$= B\left(1 + a^2 z^2\right] \tag{6.8}$$

where B is the value of the magnetic field at $z = 0$, including the contribution from the trap coil. The parameter a may be determined empirically by magnetic field measurements as in Figure 3.4. If the parameter a is small enough so that changes in the magnetic field are small on the length scale of the gyroradius of the electron, it can be shown that the magnetic moment of the electron, μ, is an exactly conserved[4] quantity:

$$\mu = \frac{m v_\perp^2}{2B}\hat{B} \tag{6.9}$$

The interaction between the magnetic moment of the electron in its orbit and this inhomogenous total magnetic field can be expressed in terms of the magnetic moment of the electron via a simple interaction Hamiltonian:

$$\mathcal{H}_{int} = -\mu \cdot \mathbf{B}$$

[4]This would be a very difficult assumption to invalidate on the scale of a Project 8 like experiment, and can be safely taken for granted.

Because the magnetic moment for the electron orbit is aligned along the magnetic field, this term gives rise to a Hooke's law potential:

$$U_{trap} = -a^2 B\mu z^2$$

from this relation, we can immediately deduce that the axial frequency of motion must be

$$f_a = \frac{1}{2\pi}\sqrt{\frac{2a^2 B\mu}{m_e}} \tag{6.10}$$

$$= \frac{a}{2\pi}\sqrt{\frac{2B}{m_e}\frac{mv_\perp^2}{2B}} \tag{6.11}$$

$$= \sin(\theta)\frac{ac\beta}{2\pi}\sqrt{\frac{B}{B(z_0)}} \tag{6.12}$$

Where $B(z_0)$ is the strength of the magnetic field at the z position where the electron is created. With this in hand, we can extend the results of the analysis of the electron motion in Section 1.3 to include this axial motion:

$$z(t) = z_0 + z_{max}\sin(2\pi f_a t) \tag{6.13}$$

$$x(t) = x_0 + r_c\cos(2\pi f_c t) \tag{6.14}$$

$$y(t) = y_0 + r_c\sin(2\pi f_c t) \tag{6.15}$$

Without loss of generality, we can set z_0 to zero, and express $z(t)$ in terms of the pitch angle of the electron at the center of the trap:

$$z_{\max} = \frac{1}{a}\cot(\theta) \tag{6.16}$$

And now the expected signal can be expressed thusly:

$$f(t) = \frac{eB}{\gamma m}\left[1 + a^2 z_{\max}^2 \sin^2(2\pi f_a t)\right] \tag{6.17}$$

Expanding $z_{\max}$, we have the following expression for the electron frequency:

$$\begin{aligned} f_c(t) =& \frac{eB}{\gamma m}\left[1 + a^2 z_{max}^2 \sin^2(2\pi f_a t)\right] \\ =& \frac{eB}{\gamma m}\left[1 + \frac{1}{2}\cot^2(\theta)\left(1 - \cos(4\pi f_a t)\right)\right] \end{aligned} \tag{6.18}$$

where the modulation amplitude may be understood as due to the average field which is experienced by the electron, and the modulation frequency is twice the axial frequency because the field is quadratic and therefore there are two values for z at which the field is equal to its average.

6.1.2 Reintroducing Power Loss

Because the electrons that find themselves trapped by the bottle coil are continuously losing power in the form of cyclotron radiation, the factor γ^{-1} is changing in time. Therefore, even in the absence of a confining magnetic field, the cyclotron frequency for a relativistic electron would not be constant in time. The change in frequency can be written in terms of the power radiated by the electron:

$$\begin{aligned}\dot{f}_c =& \dot{K}\frac{df_c}{dK}\\ =& -\dot{K}\frac{1}{2\pi}\frac{1}{\gamma^2 mc^2}\frac{eB}{m}\\ =& -\dot{K}\frac{f_c}{mc^2\gamma}\end{aligned}$$

As observed previously, $-\dot{K} = P_c$, so that

$$\dot{f}_c = \frac{P_c f_c}{mc^2\gamma} \tag{6.19}$$

With the assumption that the power loss is constant[5] we can then include in the overall instantaneous frequency law a linear increase:

$$f_c(t) \approx f_c\left(1 + t\cdot\frac{P_c}{mc^2\gamma}\right) \tag{6.20}$$

6.1.3 The frequency of radiation as observed in the receiver frame

Because the electron and the amplifier are in relative motion, the time as measured in the electron frame is different from the receiver frame, and there will be a doppler shift. In a parabolic trap, the receiver time and electron time are related through a simple

[5]It most certainly is not, but as long as we are only concerned with the electron for a short time in which its energy does not change much, this is a reasonable assumption.

transformation[31]:

$$t_r = t_e - \frac{z(t_e)}{v_p} \tag{6.21}$$

where v_p is the phase velocity of radiation in the waveguide. While the time and frequency are different in the source and receiver frames, the phase of the radiation is a Lorentz invariant[28] quantity:

$$\phi_e = \phi_r \tag{6.22}$$

To transform from the source frequency to receiver frequency, we note that the frequency is the derivative of the phase and change coordinates:

$$\begin{aligned} 2\pi f_r =& \frac{d\phi_r}{dt_r} = \frac{d\phi_e}{dt_r} = \frac{d\phi_e}{dt_e}\left(\frac{dt_e}{dt_r}\right)^{-1} \\ = 2\pi f_e &\left(1 - \frac{v_z(t_e)}{v_p}\right)^{-1} \end{aligned} \tag{6.23}$$

Which, for axial velocities that are small compared to the phase velocity, can be expanded to first order to yield

$$f_r = f_e\left(1 + h_a \cos\left(2\pi f_a t_e\right)\right) \tag{6.24}$$

Where the axial modulation index $h_a = 2\pi z_{\max} f_a v_p^{-1}$.

6.1.4 The total instantaneous frequency law in the receiver frame

Combining the linear modulation from power loss with the sinusoidal modulations from the axial motion and the doppler shift (and approximating $t_e = t_r = t$), we arrive at the total instantaneous frequency (IF) law for the electron in the receiver frame:

$$f_c(t) = \frac{1}{2\pi}\frac{qB}{m\gamma}\left[1 + t \cdot \frac{P_c}{\gamma mc^2} + \frac{z_{max}^2}{2}\left(1 - \cos\left(4\pi f_a t\right)\right)\right] \cdot \left(1 + h_a \cos\left(2\pi f_a t\right)\right) \tag{6.25}$$

This level of detail is obscured in general by the time resolution of the detecting equipment, as will be explained in a later section.

6.1.5 Emitted power revisited

The axial motion of the electron modifies its coupling to the waveguide in a non-trivial way. An internal collaboration report[31] performed a calculation for the coupling constant

$A[t|f]^{\pm}$ for the dominant $\mathrm{TE}_{1,0}$ waveguide mode calculated in the receiver frame:

$$A^{\pm}(t) = \sqrt{2}\pi \frac{eZ_{\lambda} f_c r_c}{ab} \cos\left(\frac{\pi x_0}{a}\right) \sum_{m=-\infty}^{+\infty} J_m(h_a) \cos\left(2\pi \left(f_0 + m f_a\right) t\right) \tag{6.26}$$

where the Bessel function argument is the axial modulation index h_a. $\mathcal{F}[t|A]$ exhibits peaks at the carrier frequency f_0, but in addition there are sidebands separated from the carrier by integer multiples of the axial frequency. The power in the axial sidebands is expected to be attenuated by about $-20\,\mathrm{dB}$ relative to the power in the first harmonic for electrons with a pitch angle close to $\pi/2$. However, the above expression has zeros - there are pitch angles for which the electron emits no power into the waveguide whatsoever. This very interesting consequence has implications for the pitch angles that can be detected by the Project 8 receiver, as the signal-to-noise ratio for these small pitch angle electrons may be below the detectable threshold.

6.2 The Spectrogram: Basic Time-Frequency Analysis

To analyze time-series data in such a way that the detailed evolution of the frequency spectrum of a trapped electron can be extracted is a challenge unto itself. The signal generated by the electron and amplified by the receiver may be formally representated in two extremes with respect to the information that is conveyed. First, there is $s(t)$, which is simply the voltage that is recorded as a function of time. In this representation, at any given time *all* frequencies which are present contribute to the voltage. At the other extreme is the frequency space representation as calculated by the Fourier transform of the signal $\mathcal{F}[\omega|s]$. In the frequency space representation, at any given frequency *all* times contribute to the amplitude of that particular frequency. Viewing these two representations as extremes is useful, not least of which because it exposes the area "in between" these two in which alternative formulations may yield *both* time *and* frequency information simultaneously. The most simple of these formulations, the spectrogram, may be regarded as a very natural extension of Fourier analysis to a two dimensional plane in which one axis represents frequency, and the other represents time.

The continuous time Fourier transform of a signal $s(t)$ is defined as an integral over time:

$$\mathcal{F}[f|s] = \int_{-\infty}^{\infty} dt'\, s(t') e^{-2\pi f t'} \tag{6.27}$$

As is apparent from the expression, the time dependence of the signal is integrated out, and with it goes all information regarding the time evolution of the frequency spectrum. For a signal which is *stationary*, which is to say that its frequency content is constant, this loss of information is largely irrelevant. If a single A440 tuning fork resonant at 440 Hz is struck, the power spectrum $|\mathcal{F}^*\mathcal{F}|^2$ of the resulting audio signal (perhaps collected by a microphone and digitized) will exhibit a single peak at precisely A440. On the other hand, consider the case where a second tuning fork, perhaps E649 (resonant at 649 Hz) is struck during the same period so that both tones are audible simultaneously. While a power spectrum of this combined signal will indeed show evidence of both tones, what it cannot possibly indicate is any information regarding the time ordering of the striking of the tuning forks. We can know that both signals are present, but we *cannot* know which one was struck first.

For any application in which information regarding the time ordering of different spectral components of an overall signal is important, a simple Fourier analysis is therefore woefully inadequate. In fact, this ambiguity has long been recognized - perhaps the earliest technical solution is the invention of sheet music. The horizontal position of the various notes on each staff indicates their ordering in time, and the vertical position indicates the note which is to be played. In fact, it is possible looking at the sheet music to intuit various aspects of the composition without ever *hearing* it played, such as a rising pitch or a period of silence.

6.2.1 The spectrogram: simple time-frequency analysis

We seek a sheet-music-like representation of the signal in which the time information is not integrated out. In such a representation, it is then possible to achieve localization not just in frequency, but also in time.

Figure 6.1: A page of sheet music from Mendelssohn's Elijah.

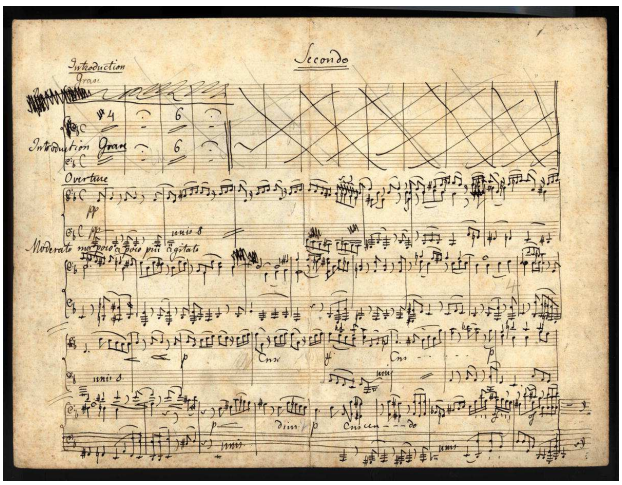

The "spectrogram" of a complex-valued signal $s(t)$ which is defined[8] in terms of a windowing function[6] $w(t, \mathcal{T})$:

$$\mathcal{S}\left[f, t|s, w\right] = \left| \int_{-\infty}^{\infty} dt'\, s(t') w(t' - t, \mathcal{T}) e^{-2\pi i f t'} \right|^2 \tag{6.28}$$

The above definition may be interpreted as follows. At any given time, t, the windowing function $w(t - t', \mathcal{T})$ localizes the signal to within some time interval centered at t with some duration which is on the order[7] of $\mathcal{T}$. The integral is taken over t', so that the spectrogram evaluated at time $t = t_0$ is the frequency spectrum of the portion of the signal which is localized around t_0. Therefore the spectrogram accomplishes the goal of localizing the signal both in time and frequency, and allows us to determine detailed information about the instantaneous frequency law of the signal so analyzed $z(t)$.

6.2.2 What an electron spectrogram might look like

For an electron that is generating a signal that follows the instantaneous frequency law as defined in Equation 6.25, a toy spectrogram calculated from its signal might appear as in

[6]The choice of which is arbitrary up to the requirement that it be even in time and bounded.

[7]No window can perfectly localize the signal to an interval of exactly $\mathcal{T}$ - this is an area of considerable study and is general discussed under the umbrella of window or sidelobe "leakage".

Figure 6.2.2 below. Despite being highly unrealistic[8] in terms of details, Figure 6.2.2 does

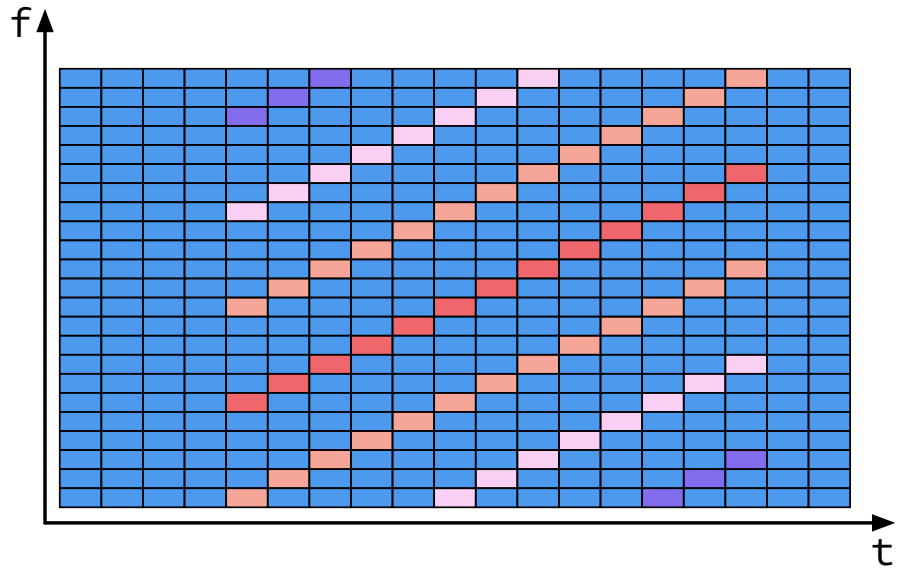

Figure 6.2: A highly schematic electron spectrogram. The carrier frequency is shown in red, and axial sidebands appear at regularly spaced intervals separated from the carrier frequency on either side. This schematic assumes negligible noise.

have the salient features expected from an electron spectrogram:

1. A "sudden" onset of high power bins, marking the beginning of an electron trajectory in the trapping field.

2. A gradual linear rise in frequency (chirping).

3. Axial sidebands appear at integer multiples of the axial frequency separated from the carrier frequency. The axial sidebands are suppressed relative to the carrier in amplitude.

[8] A realistic signal displays a much gentler frequency slope, among other things.

4. The electron has a short duration in time, eventually scattering out of the trap as a result of collisions with gas.

With a spectrogram such as the one above in hand, the goal turns to reconstruction. The instantaneous frequency law promises that information about the initial conditions of the electron - including its kinetic energy - is encoded in the recorded signal. By correctly interpreting the spectrogram, and in particular by correctly identifying the first bin which belongs to the electron signal, a wealth of information may be had.

6.3 Reconstruction methodology

In order to construct spectrograms such as the schematic shown in the last section, it is first necessary to localize electron signals roughly in time. The expected rate of trapped conversion electron events is about 1 Hz for K-shell electrons. With an average event duration of 100 µs, a ballpark figure for the effective livetime of the experiment is 0.0001%. Triggering is therefore an important tool for improving livetime and reducing overhead from storing and processing a continuous stream of digitized data, most of which would be noise.

6.3.1 Frequency Mask Triggering

Data have been collected using various models of the Tektronix 5000 series Real-Time Spectrum Analyzer almost continuously since June 2014. The acquisition bandwidth ν of these instruments is in the range 40 MHz to 110 MHz depending on the factory hardware configuration. The primary advantage of the RSA as a data-taking platform is the so-called Frequency Mask Trigger (FMT) mode of operation, shown schematically below in Figure 6.3. The FMT mode enables a frequency dependent software triggering mode in which the trigger condition is met if a signal appears in a pre-defined region of frequency space (the frequency "mask") with a power above a user-defined threshold. Upon triggering, the RSA will automatically record the time series data relevant to the triggering event to disk. A transient signal has some probability (probability of intercept, or POI) of violating the FMT for long enough that the instrument records a trigger. For an acquisition bandwidth of 40 MHz and a resolution bandwidth of 12 kHz, an electron signal of duration 30 µs has a

probability of intercept[43] (POI) of almost 1.

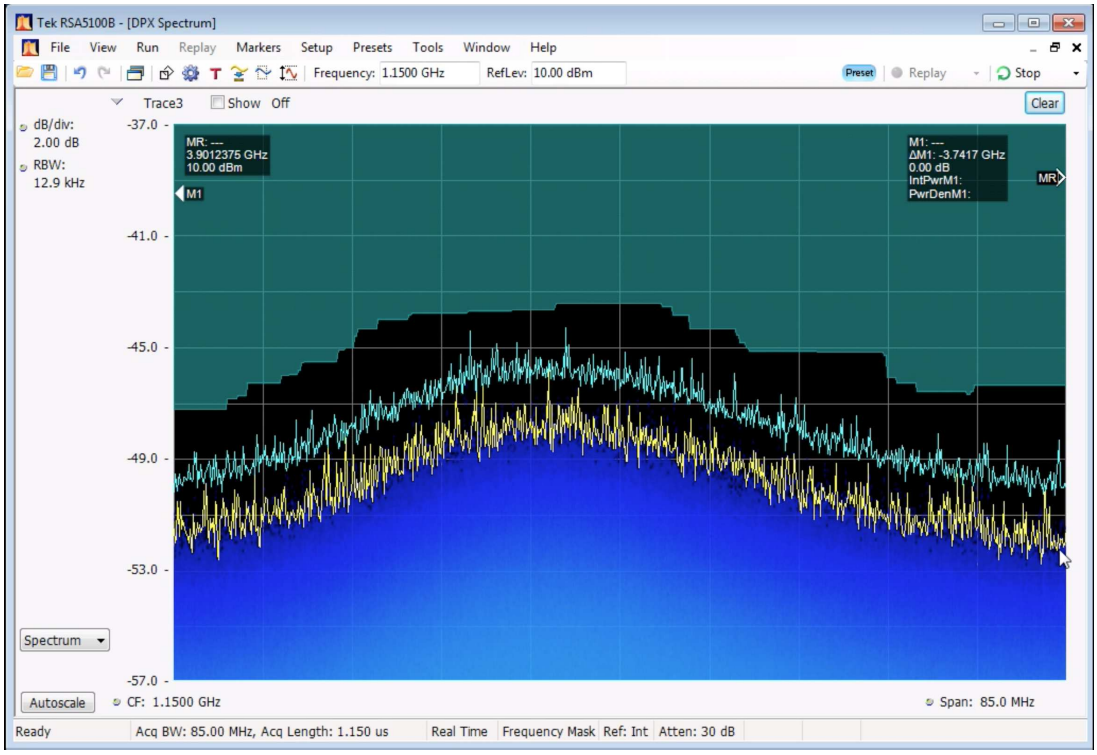

Figure 6.3: The Frequency Mask Trigger mode of the RSA essentially "masks" a region of frequency space. The cyan region of the screen which appears above the noise is the mask as defined by the instrument. If a spike of power in the frequency spectrum enters the FMT region, the FMT condition may be said to be "true". The RSA may be configured to use the violation of the mask in this way by transients as a triggering condition.

6.3.2 Analysis of time series data from triggered events

Once the RSA has triggered on the Frequency Mask Trigger, the time series data which has been recorded must be analyzed to extract the detailed frequency information of interest. This data analysis is performed on the PIC computers using the Katydid analysis software package developed for the Project 8 collaboration by N. Oblath (see `http://github.com/`

`project8/katydid`) The architecture of Katydid is modular - data processing operations are defined as composable elements and may be arranged as a dataflow pipeline, so that the output from one procedure forms the input to the next. Below are the steps by which the voltage signals recorded by the RSA are transformed by Katydid into an electron energy spectrum.

Time-Frequency Representation

The data consist of complex-valued digital samples sampled at 50 MHz, so that the time between successive samples is 20 ns. The data were processed in chunks of 4096 contiguous samples, so that the total time per slice is 81.92 µs. This slicing is effectively a boxcar windowing function, and the spectrogram of the signal is then calculated by using each slice as a distinct value of t. The final spectrogram pixel size is 12.2 kHz $\times$ 81.92 µs.

Candidate identification

Recorded events will occasionally be entirely noise with no electron signal present due to random violation of the FMT by thermal noise fluctuations. To distinguish purely noise events from those containing electrons, an identification scheme is employed which dramatically reduces the chances that a noise event will be miscategorized as an electron event.

The first step in the process of generating a so-called "candidate" from a spectrogram is thresholding. In this step, the spectrogram is reduced to a set of points $p_i = (t_i, f_i)$ in the time frequency (TF) plane for which the power in the corresponding bin in the spectrogram exceeds some signal-to-noise threshold which is specified for the particular frequency bin in question.

As is indicated schematically in Figure 6.2.2, for a true electron event, these high power bins will tend to lie close together on the $t - f$ plane, whereas they will be randomly distributed for a pure noise event. The density based clustering algorithm DBSCAN[21] is used to group the p_i into clusters based on pairwise distances. DBSCAN finds clusters in

spatial data by categorizing data points according to a simple rubric:

1. For any given point p_i, any other point p_j for which $|p_j - p_i| < \epsilon$ on some suitably defined norm (Project 8 uses the simple ℓ_2 norm) is said to be directly reachable. The set of all points which are directly reachable from p_i is denoted R_i. A point p_i which has $|R_i| > 0$ is called a core point.

2. Consider a single p_i and its directly reachable set R_i. If another point $p_k \notin R_i$ is reachable from some point $p_j \in R_i$, then that point is said to be density reachable from p_i. The set of all points which are density reachable from p_i is denoted D_i.

3. All points p_i s.t. $|D_i| \leq C$ where C is a cardinality threshold are considered outliers.

4. Clusters are defined by the set of points p_i where $|D_i| > C$.

5. Any two points which are density reachable from each other are members of the same cluster by definition, and therefore no point may belong to more than one cluster.

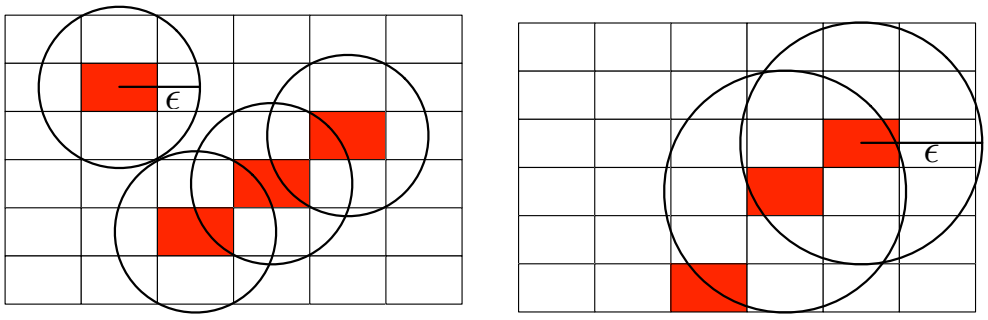

Figure 6.4: An illustration of the DBSCAN rubric for labelling points. In the left panel a density-reachable cluster is shown along with an outlier. In the right panel, the bottom center point is not directly reachable from the top right point, but is density reachable via the center point. All three points therefore belong to the same cluster.

The DBSCAN algorithm categorizes events as noise on the basis that cluster formation from random thermal fluctuations is highly unlikely. The probability of false cluster identification

is further reduced by a cut which requires that the points in a cluster must lie on a line with a slope within some range. However, noise bins may be erroneously included as members in clusters of signal bins. This effect tends to increase cluster sizes and, as detailed below in a study of the noise rejection performance of DBSCAN, tends to bias the initial frequency estimation in the low signal-to-noise regime.

While DBSCAN gives generally good results in terms of event selection, the algorithm is highly sensitive to its input parameters. Changing the value of ϵ has a dramatic effect, as does the minimum cluster size C for acceptance. Without some established training set of data, each set of data may require a bespoke set of parameters.

Forming electron tracks from clusters

The output from DBSCAN is a set of clusters. Provided at least one cluster passes the threshold for minimum size, the next stage is a fitting of the clusters with a piecewise linear function. Each cluster is assigned its own slope and time support (t_i, t_f) in this step. If two clusters are adjacent in time within some time interval δ - i.e. $t_{i,2} \leq t_{f,1} + \delta$, the clusters are merged into a track.

6.4 Sources of systematic error

Measurement of the kinetic energy of the electron is subject to systematic error. Because the energy measurement is itself derived from a frequency measurement, some of these errors originate in effects which mangle the interpretation of the original frequency information. These effects are essentially errors in scale - either the frequency scale established by the zero-energy cyclotron frequency f_0 that appears in Equation 1.10, or the scale which is introduced by the frequency of the mixing stages which translate the signal of the electron to the analysis frequencies. In fact, recalling Equation 1.10:

$$K = m_e c^2 \left(\frac{f_0}{f_c} - 1 \right)$$

the systematic error associated with a measurement of K is either derived from the numerator of the frequency ratio as an error in total magnetic field, or from the denominator as an error in observed frequency.

6.4.1 Magnetic field measurement error

While the magnetic field measurement methods outlined in Section 3.5 are useful, in practice the most practical measurement of the magnetic field comes from trapped cyclotron electrons themselves. Recall that the cyclotron frequency of an electron of known energy K in a magnetic field of the form $\mathbf{B} = \mathbf{B_0} + \mathbf{\Delta B}$ is given by

$$f_c = \gamma^{-1}(K)\,\frac{e}{m}\,(B_0 + \Delta B) \tag{6.29}$$

The contribution to the field from the inhomogenous term ΔB can be expressed in terms of the current which is supplied to the coil:

$$\Delta B = i_{\mathrm{trap}} \Delta B' \tag{6.30}$$

Where the primed B is understood to be the field per unit applied current. By varying the trap current i_{trap} and thereby ΔB, the cyclotron frequency f_c can be measured as a function of trap depth. With all other parameters fixed, the data are expected to be linear with respect to applied field, with the slope equal to $\gamma^{-1} e \Delta B'/m$, and the intercept $\gamma^{-1} e/mB_0$, thereby simultaneously measuring the background applied field as well as the current-dependent field generated by the trapping field. A primary benefit of this type of magnetic field measurement is that the field at the trap position is measured, and in fact probed directly, by the same physical system which is under study.

The measurement of the magnetic field was performed by Luiz DeViveiros at UCSB[16]. The calibration that was chosen for the kinetic energy of the K-shell conversion line is an approximation to the results given by Picard[5], $K = 17.83\,\mathrm{keV}$. A more contemporary measurement of the energy of the excited state of $^{83\mathrm{m}}$Kr which gives rise to the K-shell conversion line was performed by Venos[45]. This measurement, from which the energy of the conversion electrons can be deduced (and which is summarized in Appendix B), is

expected to alter the magnetic field calibration by several parts in 10^4.

Using the result from Picard, the magnetic field as measured by this technique at a harmonic trap current of 400 mA is

$$B_{\text{total}} = 0.951\,634(45)\,\text{T} \tag{6.31}$$

The uncertainty introduced by this systematic error is

$$\sigma_K^B \approx mc^2\gamma(K)\frac{\sigma_B}{B} \tag{6.32}$$

Which is roughly 25 eV for the entire $^{83\text{m}}$Kr spectrum, the prefactor of γ being somewhat insensitive to the kinetic energy K.

While this is a powerful method of measuring the magnetic field, a previously measured line energy must be used as a calibration to calculate the prefactor γ^{-1} which appears in the expression for the magnetic field. Any error in the previously measured spectrum is therefore inherited by comagnetometry.

6.4.2 Magnetization of materials

If the magnetic field is measured independently of the conversion electrons in the trap, and without the insert present in the bore, there will be a systematic error in **B** associated with magnetization of the insert materials upon installation into the magnet bore. The construction materials have been carefully chosen to minimize this effect - the insert is constructed entirely from indium, aluminum, and OFHC copper. However, there will be nonetheless be a small perturbation of the magnetic field due to the non-negligible permeability of the insert.

The geometry of the insert is complicated, and analytically determining this contribution to the magnetic field is therefore difficult. Indeed, any simplifying assumption made to reduce the problem to a subset of the geometry is likely to neglect an important contribution, as the overall strength of this effect is a sum of small terms. A full 3-D model of the insert as built was therefore studied by Brent VanDevender using the Ansys Maxwell 3D

magnetic field solver at PNNL. Magnetization is expected from the results of this simulation to contribute a field on the order of 10 µT, or in terms of energy following the above prescription, $\sigma_K^{\chi} \approx 5\,\text{eV}$.

It should also be noted that whatever the total field is, if the in-situ method of comagnetometry is used to measure it, this systematic may be neglected, as it involves an unknown term which is probed directly by comagnetometry.

6.4.3 Oscillator frequency

The first stage mixing oscillator is a phase locked dielectric resonant oscillator (PLDRO) with excellent short term stability. However, the long term drift of the oscillator is guaranteed to only 1 ppm, which corresponds to a frequency uncertainty of about 50 kHz. Expanding Equation 1.10 in terms of this small frequency error δf, the equivalent systematic uncertainty in kinetic energy associated with imperfect knowledge of the oscillator frequency is

$$\sigma_K^{\text{osc}} \approx mc^2\gamma\left(K\right)\frac{\delta f}{f_c} \tag{6.33}$$

which is on the order of 1 eV.

6.4.4 Systematics table

Below is shown the expected systematic errors for all effects listed above, evaluated at the energies of interest for K, L, and M shell conversion electrons. Also shown is the quadrature sum of the systematic uncertainties.

Shell	σ_K^B	σ_K^{χ}	σ_K^{osc}	$\sigma_K = \sqrt{\sum(\sigma_K^i)^2}$
K	25.00 eV	0.56 eV	1.03 eV	25.03 eV
L	25.60 eV	0.57 eV	1.08 eV	25.63 eV
M	25.95 eV	0.58 eV	1.09 eV	25.98 eV

6.5 Expected spectral lineshape

From the standpoint of trying to measure the kinetic energy of a trapped electron, z_0 and z_{max} (and by extension, the pitch angle θ) are effectively nuisance parameters. In order to

measure the initial energy of the electron, the signal frequency must be measured precisely at the time when the electron is created (taken to be $t = 0$ without loss of generality). In the STFT, the peak frequency at $t = 0$ will correspond to the average cyclotron frequency of the electron over the time duration of the pixel:

$$f_c(t \approx 0) = \frac{1}{2\pi}\frac{qB}{m\gamma}\left[1 + \frac{1}{2}\cot^2(\theta)\right] \tag{6.34}$$

Here θ is understood to be the pitch angle of the electron at the minimum of the trap. The distribution of observed frequencies χ_f for a monochromatic source of electrons (or nearly so, as in the case of the 17.8 keV ^{83m}Kr line) is referred to as the lineshape (or detector response).

6.5.1 Trapping coil lineshape in the harmonic approximation

The pitch angle θ for any given electron takes values between 0 and π which are distributed uniformly at the point of its creation with respect to solid angle: $P_\theta \propto \sin(\theta)$. We can use this distribution to transform Equation 6.34 into a probability distribution to observe f_c from a monochromatic source of electrons with "true" boosted cyclotron frequency $f_0 = eB/m\gamma$:

$$\begin{aligned} f_c &= f_0\left(1 + \frac{1}{2}\cot^2(\theta)\right) \\ \implies \theta &= \cot^{-1}\left(\sqrt{2\left(\frac{f_c}{f_0} - 1\right)}\right) \\ \therefore \chi_f = |J| \cdot P_\theta\left(f_c^{-1}\right) &= \frac{1}{2f_c - f_0}\frac{1}{\sqrt{2\left(\frac{f_c}{f_0} - 1\right)}}\frac{1}{\sqrt{2\frac{f_c}{f_0} - 1}} \end{aligned} \tag{6.35}$$

The singular nature of the lineshape near $f_c = f_0$ reflects the rapidly growing phase space available to the electron as it approaches a pitch angle of $\pi/2$. However, this predicted lineshape is far too narrow to adequately explain the observed variation in initial cyclotron frequency.

Shown below in Figure 6.5 is a diagram which indicates the phase space in which electrons will be trapped by this phenomenological description of the solenoidal bottle coil.

The lineshape as calculated in Equation 6.35 is singular at the point $f_c = f_0$.

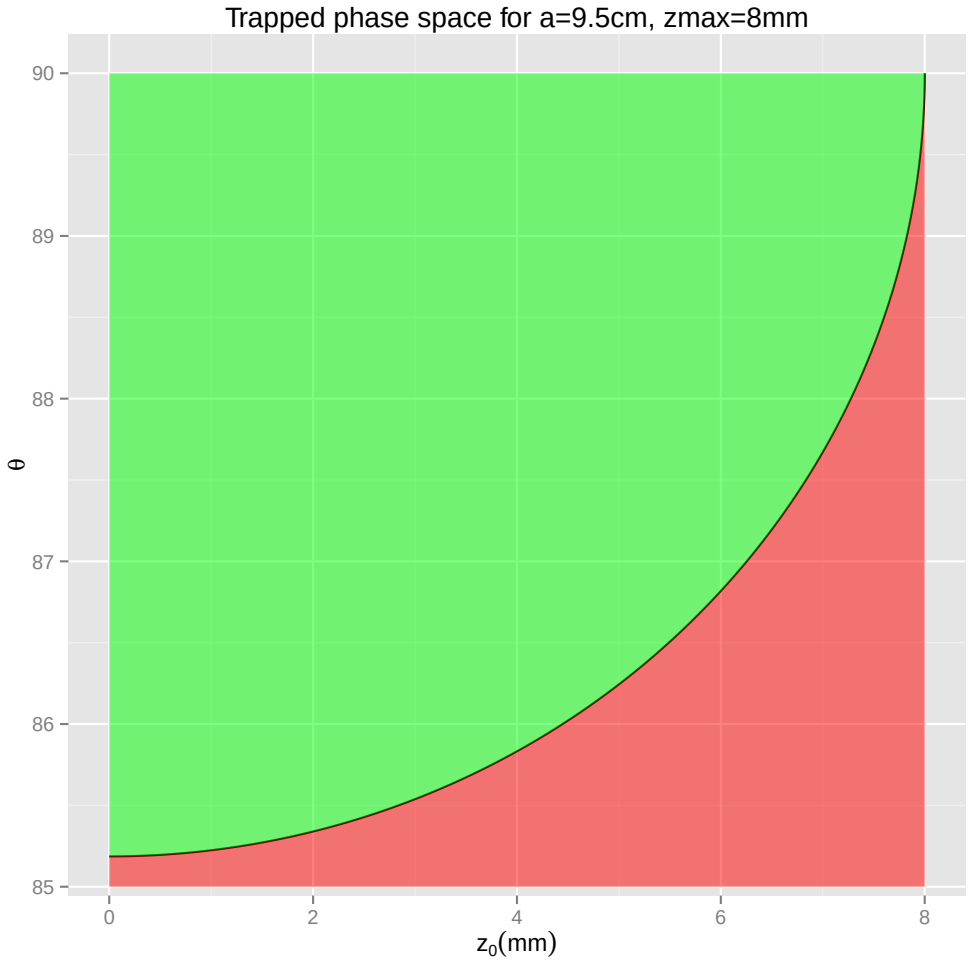

Figure 6.5: The trappable phase space for a harmonic coil with parameters $a^{-1} = 9.5\,\mathrm{cm}$ and $z_{max} = 8\,\mathrm{mm}$. Red regions indicate where the PDF is identically zero, and green regions are trapped.

Trapped pitch angle acceptance

In a magnetic trap configuration that is highly inhomogeneous such as the harmonic trap coil, the observed frequency spectrum will be considerably broadened by the distribution of pitch angles which characterizes trapped electrons. The axial frequency of the harmonic trap is only weakly dependent on pitch angle, and is predicted to have a typical value of

about 100 MHz. Because the width of the time bins in the STFT bins is very large (81.92 µs) compared to the axial period of a trapped electron, the carrier frequency will correspond to the average frequency of the electron over many axial periods. Small pitch angle electrons will explore higher magnetic field regions, so that the initial frequency that is observed for an electron of pitch angle θ will be:

$$f_c(\theta) = f_c\left(1 + \frac{1}{2}\cot^2(\theta)\right) \tag{6.36}$$

Were this the only consideration, the expected lineshape would be given by Equation 6.35. However, the pitch angle affects the observed lineshape in a number of ways, including:

- The average field experienced by a trapped electron, and therefore the average frequency of radiation emitted over several axial periods.

- Due to wave interference phenomena in the waveguide, there are axial frequencies for which no power is emitted into the fundamental and instead all of the radiated power appears in the axial sidebands. This behavior changes the probability of detection by the receiver.

The feature of the pitch angle blurring that is most important to interpreting the observed spectrum, however, is the fact that $\cot(\theta)$ takes its minimum value at $\theta = \pi/2$, and therefore the effect of pitch angle on the observed distribution will always increase the frequency (decrease the energy) of a given observation. This blurring gives rise to a significant high frequency tail, but the effect is much more muted on the low frequency edge.

The low frequency (high-energy) edge is expected to have a much simpler shape. In the limit of high signal-to-noise ratio where the probability of initial bin misidentification is low, the high energy lineshape should be well modeled by the convolution of a Lorentzian profile and a Gaussian profile. This combination is known as a Voigt profile, and is often used to describe the observed lineshape in ultraviolet spectroscopy. While a full description of the low energy tail of the spectrum is left an open question, this treatment of the high energy edge should be a reasonable proxy for the underlying response of the detector without the

pitch angle effect, and should therefore a hint at what the ultimate resolution of the detector may be.

6.5.2 Monte carlo study of lineshape

In general, the distortions to the observed lineshape are much more complicated than what can be accounted for analytically. The assumption that the field is harmonic and that electrons are emitted at precisely $z = 0$ are both demonstrably incorrect, and deviations from the expected lineshape are certain. To probe these more complicated effects, numerical integration over the predicted distributions is an appealing alternative to analytic study.

Monte Carlo calculations of the expected lineshapes for a solenoidal bottle coil have been performed according to the procedure below:

1. Draw an initial electron position from a uniform distribution over the extent of the trap $z_0 \in (-Z, Z)$. The maximum Z values should be chosen so that the entirety of the trapping region is covered. The initial magnetic field for this electron may then be calculated from the known trap shape. In this case, the on-axis field due to a short solenoid was used.

2. Draw a pitch angle for this electron from a uniform solid angle distribution. If the pitch angle obeys
$$\theta \geq \cot^{-1}\left(\sqrt{\frac{B_{max}}{B(z_0)} - 1}\right) \tag{6.37}$$
Where B_{max} is the value of the field outside the trapping region, accept the sampled pair (z_0, θ).

3. For each accepted sample, calculate the initial cyclotron frequency averaged over many axial periods by transforming the initial pitch angle to θ to the pitch angle at the center of the trap θ_0, and using the form $f_c = f_0\left(1 + \frac{1}{2}\cot^2(\theta_0)\right)$.

The distribution of frequencies so obtained is a numerical estimate of the lineshape for the trap in question, and is shown below for the harmonic trap in Figure 6.6. Initial positions with $|Z| = 2\,\mathrm{cm}$ were generated uniformly for monoenergetic electrons with $T = 17.8\,\mathrm{keV}$. All angles were considered and distributed in accordance with a uniform solid angle. The maximum field amplitude from the trap coil was -1.636 mT at $z = 0$, and the main background field was 0.953 27 T and taken to be completely homogenous. No off-axis components of the magnetic field due to the trap were considered in this calculation. The "true" cyclotron frequency f_0 for this field configuration is about 25 613 MHz.

As expected, there is a peak at low frequencies which corresponds to the cyclotron frequency in the superimposed fields. The high frequency structure of the lineshape is due to electrons which are born at large $|z_0|$ with pitch angles close to $\pi/2$. Indeed, as shown in Figure 6.5.2, the contributions to high frequencies in the lineshape are dominated by electrons for which $|z_0| > 7.5\,\mathrm{mm}$.

6.6 Data collection: the gory details

All data shown in the following section was collected with a Tektronix 5106A, with an acquisition bandwidth of 40 MHz and a true bandwidth of 50 MHz. The instrument was operated in frequency mask trigger mode, with the mask constructed automatically by the instrument to begin 3 dB above the thermal noise floor of the receiver. Upon triggering, a total of 5 ms of data was recorded, including 1 ms of pre-trigger holdoff data.

The time-series data were analyzed with Katydid, using DBSCAN for event selection with the minimum cluster size set to 4, and the connectivity radii set to $\epsilon_f = 150\,\mathrm{kHz}$ and $\epsilon_t = 600\,\mu\mathrm{s}$. The slice size was 4096 (82 µs), for a resolution bandwidth of 12 207 kHz.

The K-shell dataset consists of 9916 trigger events, of which 7244 passed the DBSCAN event selection for an efficiency of 73.05%. All data were recorded on September 3, 2014, over an exposure time of 6 hours.

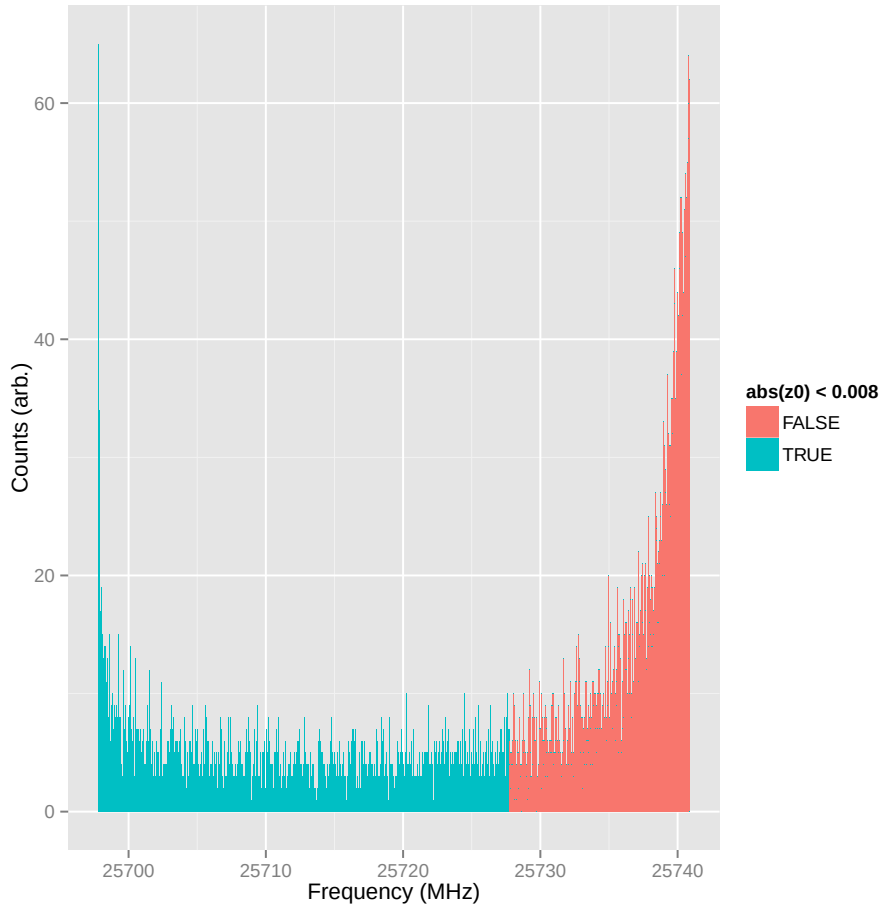

Figure 6.6: The distribution of observed frequencies for a sample ($N = 10000$) of initial conditions for trapped electrons. The bottle coil has a maximum field strength at its center of -1.636 mT, and the main background field is of a uniform 0.953 27 T strength.

The raw L-shell dataset contains 10364 trigger events. 7882 of these events passed the DBSCAN event selection criteria, for an efficiency of 76.05%. The data were recorded on September 3, 2014, over an exposure time of 6 hours.

M-shell events were recorded on September 9, 2014. 8790 triggers were recorded to disk, and 5540 passed event selection for an efficiency of 63.02%. This somewhat lower efficiency is accounted for by a higher noise floor in the vicinity of the M-shell events.

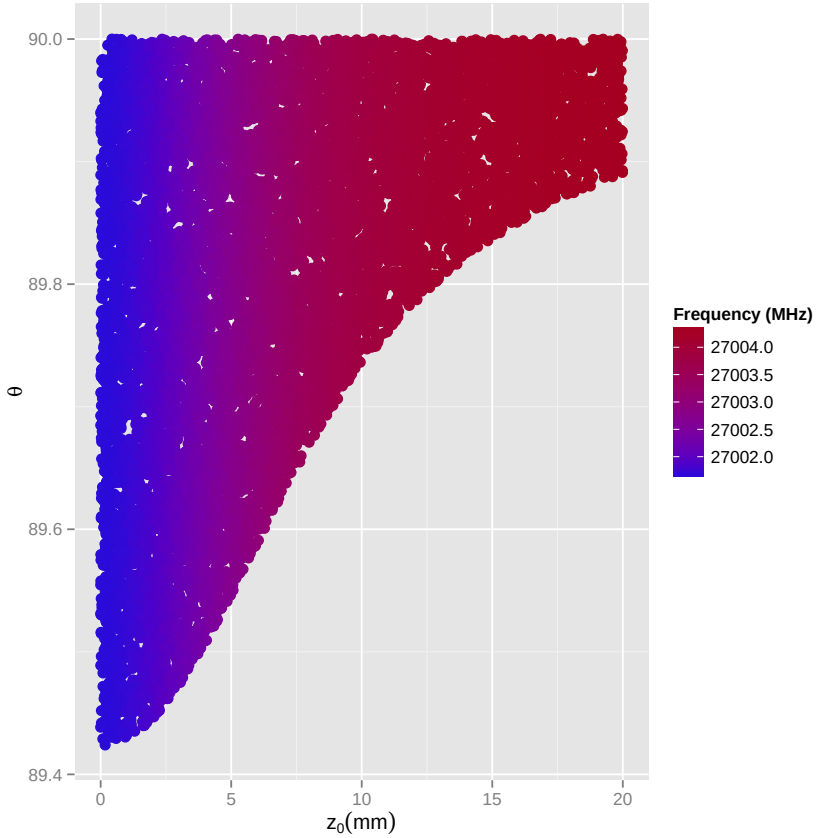

Figure 6.7: The phase space for which electrons are trapped in a solenoidal trap coil monte carlo. The simulation is carried out for all positions in the area of the plot, and trapped electrons are marked. The color of the points indicates their initial cyclotron frequency.

Chapter 7

RESULTS

The culmination of this text up to this point is the first observation of the cyclotron radiation from a single trapped electron in the Project 8 CRES prototype experiment. While it is premature to declare that the experiment has reached its precision era, it is noteworthy that all conversion lines that have been reported for the 32 keV transition in previous literature have been observed.

The purpose of this chapter is to present the data which have been collected and processed as described above - to wit, the frequency and reconstructed energy spectra of conversion electrons from ^{83m}Kr. To motivate the topic, the spectrogram of the signal from a single trapped electron will be analyzed first. Having done so, the aggregated frequency and energy spectra from an ensemble of electrons representing the K, L, M, and N series conversion lines will be shown. Finally, a comparison will be made between the observed spectra (and fits to those spectra) and previous work. Discrepancies and possible explanations for those discrepancies will be discussed.

7.1 Analysis of the spectrogram from a single K-shell electron

Shown below in Figure 7.1 is a selected spectrogram of the signal from a single trapped electron taken from a sample of electrons ($N = 7823$) all recorded on July 2, 2014 during a 7200 s period. The calibration of the z-axis was performed by careful measurement of the gain of all of the components in the receiver chain including the tickler port and then using a tone of known amplitude as a standard candle. The uncertainty of the gain calculation is estimated at ± 1 dB. Time series data were acquired using a Tektronix 5106A with an acquisition bandwidth of 40 MHz, a capture time of 5 ms, and a trigger holdoff of 20%. The low frequency receiver chain was bypassed for this measurement in lieu of the internal

heterodyne receiver of the RSA.

The cyclotron frequency of the recorded events in this run are centered on a frequency window 50 MHz wide centered on the expected cyclotron frequency for a 17.8 keV conversion line from ^{83m}Kr, as estimated from measurements of the magnetic field using a trap depth scan. Identification of this line as belonging to K-conversion electrons can be made with high confidence, as the K-shell line is a singlet, and the closest neighboring conversion line (the L_1 line at ≈30.2 keV) is 600 MHz distant.

The current applied to the harmonic trap used for this measurement was 1.00 A, resulting in a trapping field of $\Delta B \approx 40\,\mathrm{mT}$.

The spectrogram in Figure 7.1 bears a striking resemblance to the schematic shown in Figure 6.2.2, with the exception of the sidebands, which are not visible. Two explanations for the lack of sidebands are offered: firstly, the carrier signal to noise ratio for this run was approximately 6 dB as evidenced by the color scale, while the predicted suppression of the sidebands relative to the carrier is −20 dB. Secondly, the acquisition bandwidth of the instrument is 40 MHz, but the first axial sideband appears ≈100 MHz from the carrier. If the sidebands were visible, then the pitch angle of the electron could be measured[1], and θ would no longer appear as a nuisance parameter in the expression for $f_c(t = 0)$, possibly leading to a much improved estimator for the initial kinetic energy of the electron.

The average power[2] emitted by the electron as measured by the calibrated z-axis in a single bin is about $-120(1)$ dB mW(or 0.5(3) fW), which is large when compared with the expectation from the calculation of electron power coupling to the fundamental waveguide mode. However, the coupling between the electron and evanescent modes is unaccounted for in that calculation, so that the total power radiated by the electron is actually bounded below by the assumption that all of the power is radiated into the dominant mode.

---

[1]This is actually not strictly speaking true in a non-harmonic trap. In the harmonic trap, the relationship between the electron pitch angle and its initial cyclotron frequency can be inverted exactly.

[2]The error associated with this measurement is assumed to be entirely due to the error in gain.

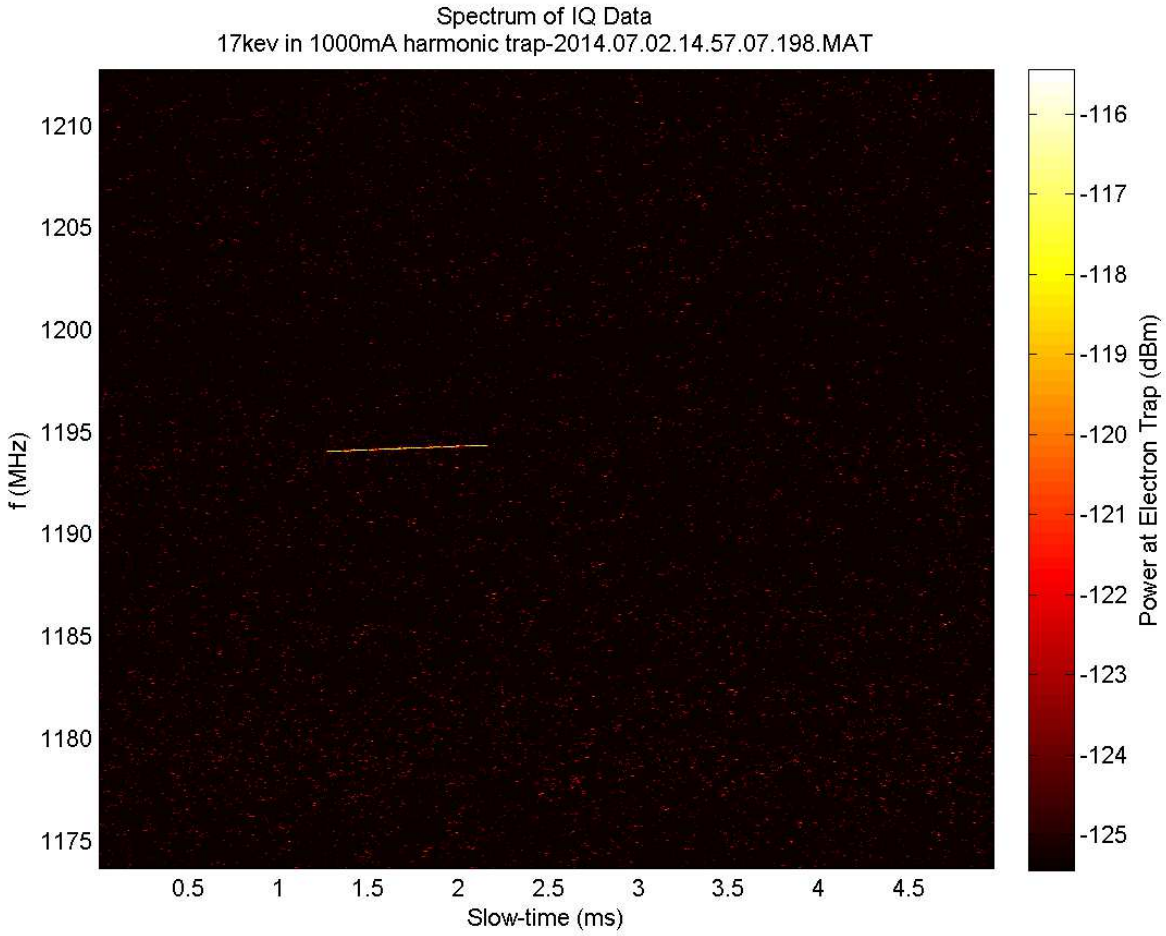

Figure 7.1: The spectrogram of the signal from a single trapped electron born at $t \approx 1.1\,\text{ms}$ that subsequently undergoes a single scattering at roughly $t = 2.2\,\text{ms}$, causing it to leave the trap.

As a check on this calculation, the rate of change of the electron frequency $\dot{f}_c$ is a complementary measure of the total energy loss of the electron. The power P_c that appears in the expression for the linear term of the electron instantaneous frequency law is a total power, and therefore is insensitive to the details of the specific modal coupling. An estimate of P_c can therefore be made by measuring the slope of the observed IF law. A linear

interpolation between the beginning and end of the electron track (and assuming symmetric 1 pixel errors) yields a slope of $452(160)\,\mathrm{MHz\,s^{-1}}$, which corresponds to an energy loss of

$$\dot{E} = mc^2\gamma\frac{\dot{f_c}}{f_c} \approx 1.5(5)\,\mathrm{fW} \tag{7.1}$$

The two measurements are in 1σ agreement.

At the time this event was recorded, an overall drift in magnetic field due to an imminent quench condition made estimation of the magnetic field difficult. However, using the best field estimate available and assuming the drift imposes a 0.5% systematic error on the value of the magnetic field, the kinetic energy of this electron can be measured: $K = 18.3 \pm 2.6(\mathrm{sys}) \pm 0.06(\mathrm{stat})\,\mathrm{keV}$. The analyses presented below will present data from a well-known magnetic environment.

7.2 Frequency and energy spectra from ^{83m}Kr source

Details of the conversion spectra, including natural linewidths, can be found in Appendix B. The data are grouped according to the shell which is converted in the decay, which corresponds roughly to a per-shell energy range. The study begins with the K-shell electrons, which have a characteristic energy near 17.8 keV. L-shell electrons appear between 30.2 keV to 30.5 keV, and the very weakly bound M and N shell electrons are grouped together around 32 keV. The raw frequency spectrum is presented along with the statistics pertinent to the dataset. An energy spectrum is generated from the raw frequency spectrum, and the high energy edge of a single representative line from each shell is fit to a Voigt profile. A summary of the fit details can be found in a table immediately following the spectra.

7.2.1 Conversion electrons from the K-shell of Krypton

The raw frequency spectrum for the K shell conversion electrons is shown below in Figure 7.2. The K-shell electrons from ^{83m}Kr can be used as an independent measurement[3] of the

[3]For details of this calculation, see Section 6.4.1.

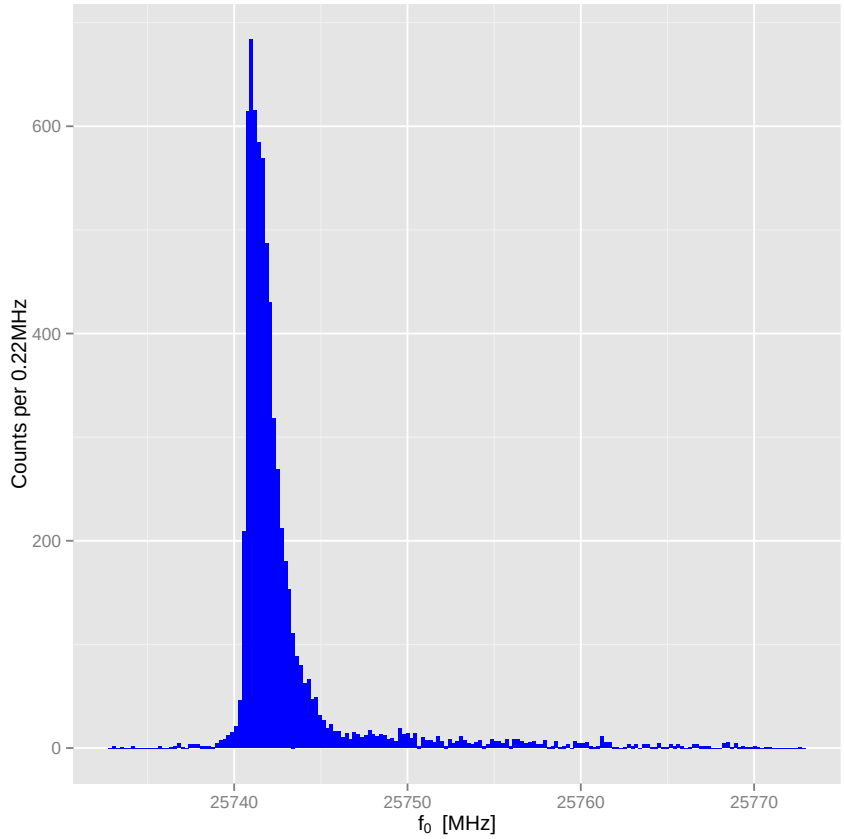

Figure 7.2: The raw frequency spectrum for the 17.8 keV data.

magnetic field in the trap B, by fixing the value of B so that the value of $f_c(T = 17.83\,\text{keV})$ is at the peak of the observed spectrum:

$$B = \frac{\gamma m f_c}{e}$$

The total magnetic field as measured[16] is 0.951 634(45) T, which corresponds to a systematic energy uncertainty of ≈25 eV. The energy spectrum for the 17.8 keV line is shown below in Figure 7.3.

The high energy edge of the spectrum shown in Figure 7.3 was fit to a Voigt profile. The edge was defined by using only energy measurements whose value was larger than the value of the peak bin in the histogram, where the Friedman-Diaconis rule was used to determine

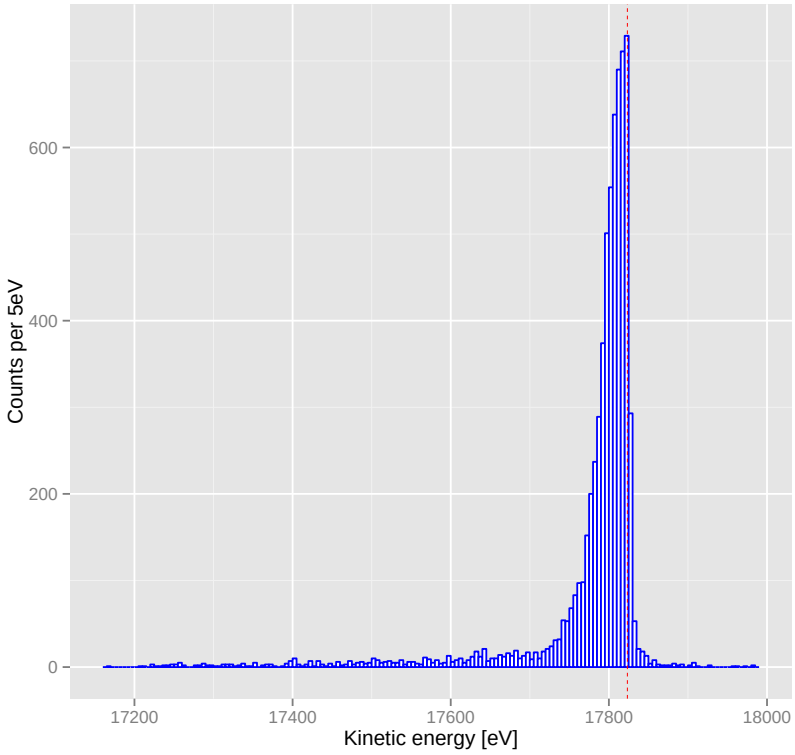

Figure 7.3: The measured energy spectrum for $T = 17.8\,\mathrm{keV}$ electrons. Measurements of the nuclear and atomic energy levels can be used to predict the energy of this line as $17\,823.64\,\mathrm{eV}$. This value is shown as a dashed red line.

bin sizes. This high-energy edge data was then rebinned according again to the FD rule. A binned fit was performed and is shown below in Figure 7.4.

The reconstructed energy from the fit is $17\,816(25)\,\mathrm{eV}$, and is dominated by systematic uncertainty associated with the measurement of the magnetic field. The reduced χ^2 for this fit is 1.69 per d.o.f..

7.2.2 L-shell conversion electron events near 30 keV

Figure 7.5 below shows the raw frequency spectrum for a sample of L-shell conversion electrons ($N = 6666$).

All three L conversion lines are clearly represented in the spectra. The reconstructed

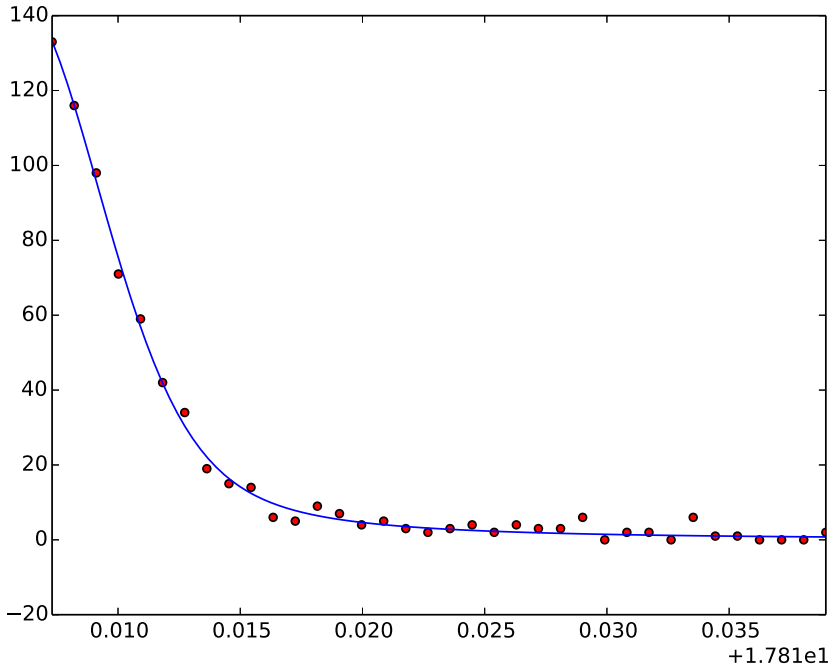

Figure 7.4: The plot and raw data for the Voigt profile fit to the high energy edge of the K-shell conversion electron energy spectrum. The fit and data are in excellent agreement.

energy spectrum is shown below in Figure 7.6.

The fitting procedure used on the K-shell electrons was also used for the highest energy L_3-shell conversion line, with a result of $E_c = 30\,468(25)\,\mathrm{eV}$, again dominated by systematic error. The other L-series lines were not analyzed due to the distortion introduced by the low energy tail from the L_3 electrons. The fit to the data in the high energy edge is shown below in Figure 7.7.

The reduced χ^2 of 1.91 is somewhat worse than that of the K-shell electrons.

7.2.3 M and N-shell conversion electrons

The weakly bound M and N shell electrons give rise to a complex of internal conversion lines near $K = 32\,\mathrm{keV}$. Spin-orbit coupling is responsible for the appearance of closely

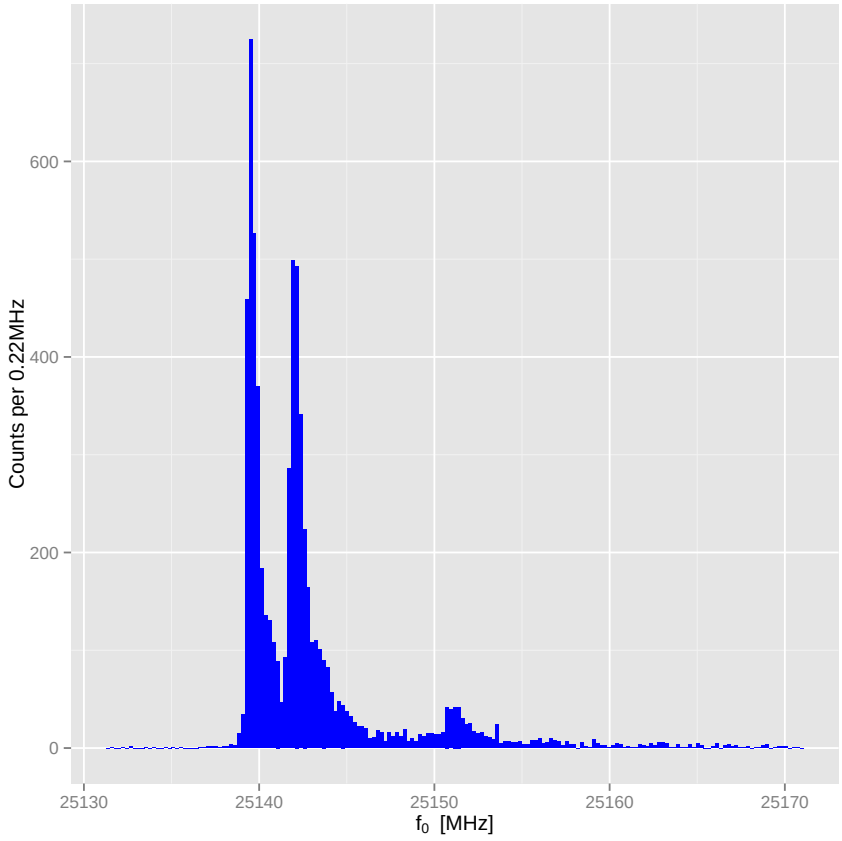

Figure 7.5: The raw observed frequency spectrum for L-shell conversion electrons from ^{83m}Kr. All three lines which are expected are clearly observed.

spaced doublets in the spectrum which are far below the resolution of Project 8 - the N_{2+3} line is a doublet with a spacing of 0.66 eV. These lines may be of considerable interest in future experiments - the binding energy for these is typically known to a few µeV from optical spectroscopy, giving a very precisely known fixed point in the energy spectrum.

The frequency spectrum from M and N-series electrons are shown in Figure 7.8, and contains evidence for observation of all of the known conversion lines in the series.

The complicated forest of lines combined with the relatively low bin statistics of this dataset makes reconstruction of the highest energy N_{2+3} line difficult. Instead, the doublet

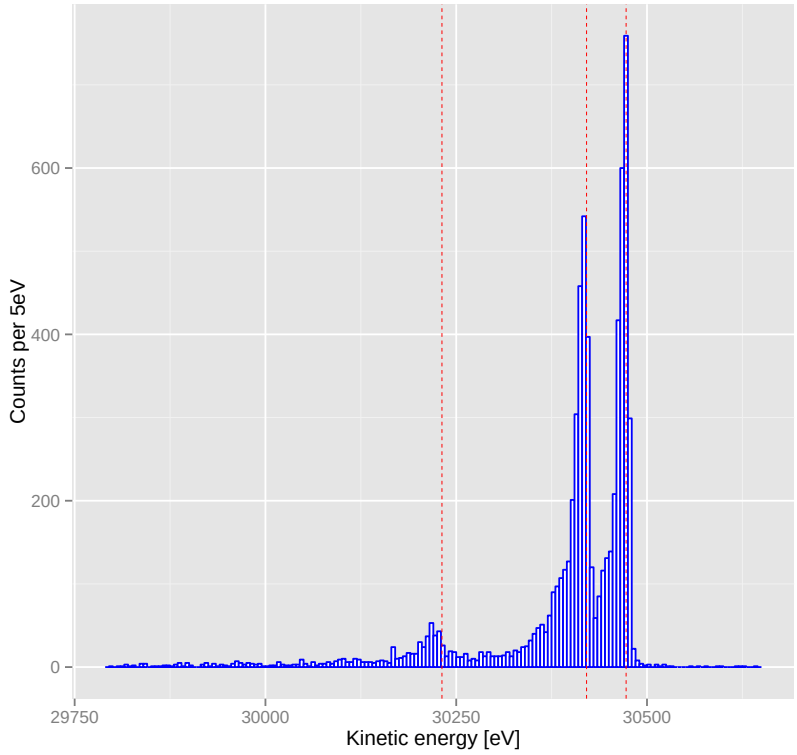

Figure 7.6: The measured energy spectrum for L-shell conversion electrons. Expected energies of 30 231.3 eV, 30 420.8 eV, and 30 472.63 eV are shown as dashed red lines.

$M_{1,2}$ line was used under the erroneous assumption that it is a single spectral component. The fit data is shown in Figure 7.10.

The measured energy value is 31 926(25) eV.

7.2.4 Detailed fit results

A summary of the fit parameters, along with 1σ errors obtained by bootstrapping, are shown in Table 7.11 below. The FWHM of the components of the Voigt profile is given for each line, along with the total FWHM of the Voigt profile itself. The FWHM of the Voigt profile is defined as $\mathrm{FWHM}_V \approx 0.5346\mathrm{FWHM}_L + \sqrt{0.2166\mathrm{FWHM}_L^2 + \mathrm{FWHM}_G^2}$, where the approximation is valid[35] to within 0.02% and $\mathrm{FWHM}_{L,G}$ are the full-widths at half-maximum for

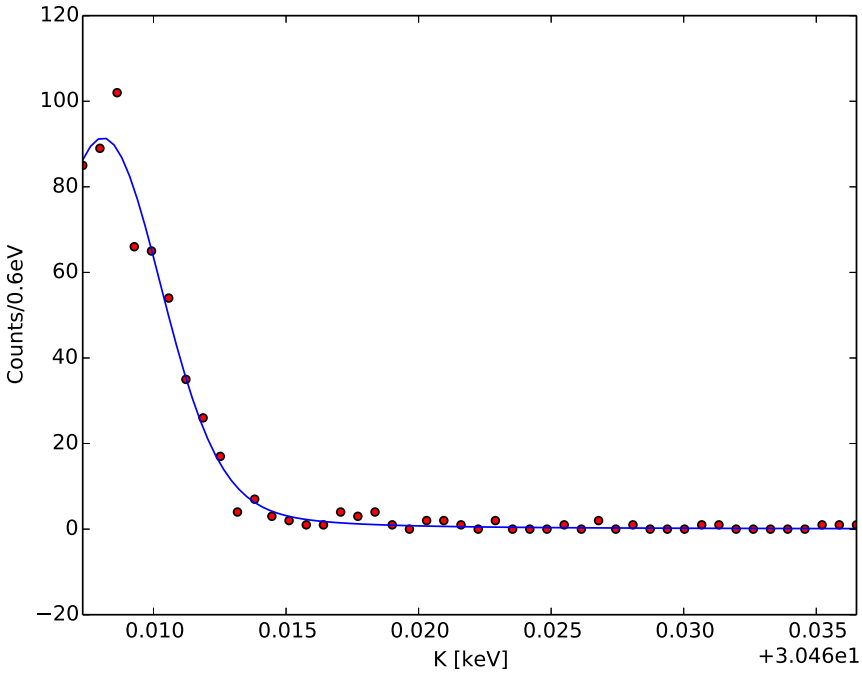

Figure 7.7: The Voigt profile fit of the high energy edge of the L_3 conversion line is presented with the raw data. The data clearly show some structure in the peak due to the choice of binning.

the Lorentzian and Gaussian components of the Voigt profile, respectively.

7.3 Discussion

The overall impression from the data is that the measured spectra are in good agreement with expectations, both from prior art and from X-ray studies. All three energy measurements are dominated by a common systematic error of 25 eV which originates in the present understanding of the magnetic environment in the experiment. Over the course of data taking, the secular drift in the magnetic field should present an additional systematic uncertainty in the magnetic field of roughly 10ppb.

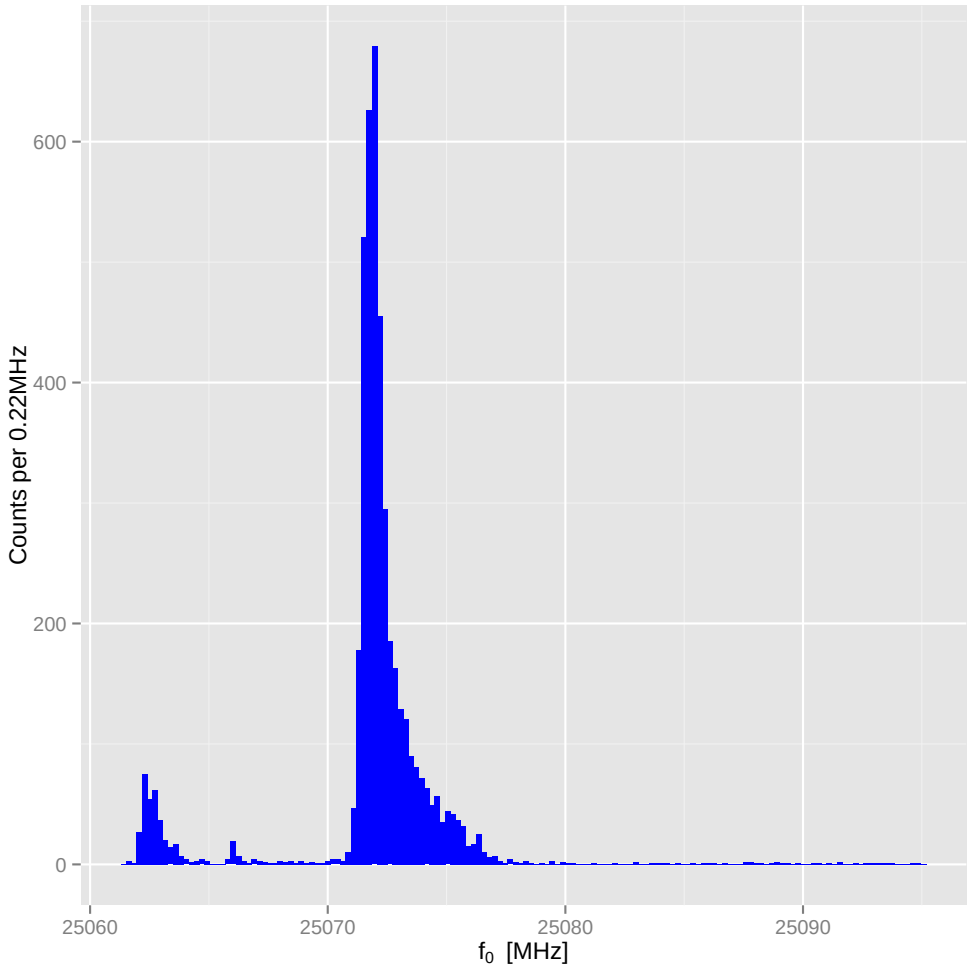

Figure 7.8: Initial frequency spectrum for M-shell and N-shell conversion electrons.

7.3.1 K-shell electrons

The reconstructed energy of the K-shell peak, $17816 \pm 25(\text{syst}) \pm 6(\text{stat})\,\text{eV}$, is in agreement with the expected value of $17\,823.64\,\text{eV}$ from combining X-ray studies with nuclear binding energy measurements[44]. In addition, the FWHM of the Lorentzian component of the fitted Voigt profile - $3.3 \pm 0.9\,\text{eV}$ is consistent with the measured natural linewidth of $2.83\,\text{eV}$, albeit with a somewhat large error.

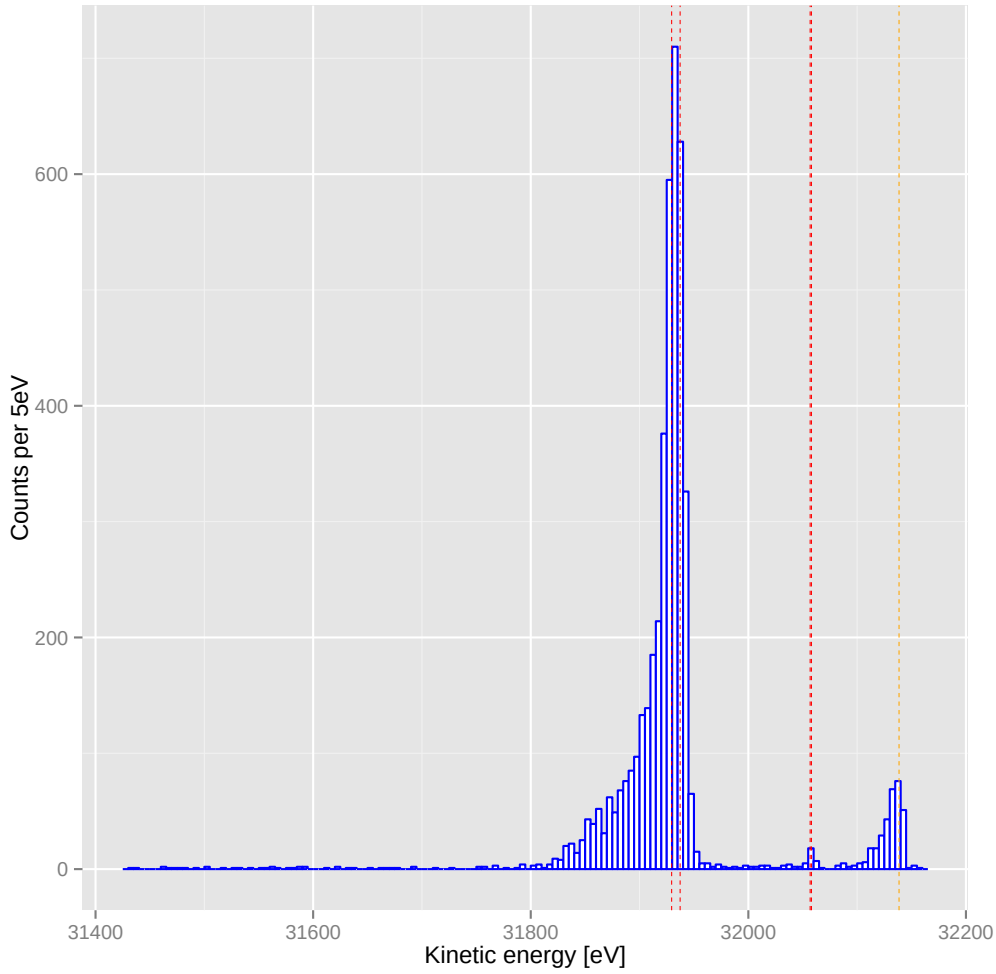

Figure 7.9: The measured energy spectrum for M-shell and N-shell conversion electrons. Expected energies of 31 929.5 eV(M_1), 31 937.3 eV(M_2), 32 056.8 eV(M_3), and 32 058 eV(M_4) are shown as dashed red lines.

Comparing the observed lineshape of the frequency spectrum to that calculated by monte carlo reveals a discrepancy in the shape as shown below in Figure 7.12. In particular, the shape of the frequency spectrum as observed is much sharper than predicted by monte carlo. Additionally, the simulation predicts the presence of a long, fat tail on the high frequency side of the peak which is not observed in real data. While a heavy tailed distribution is

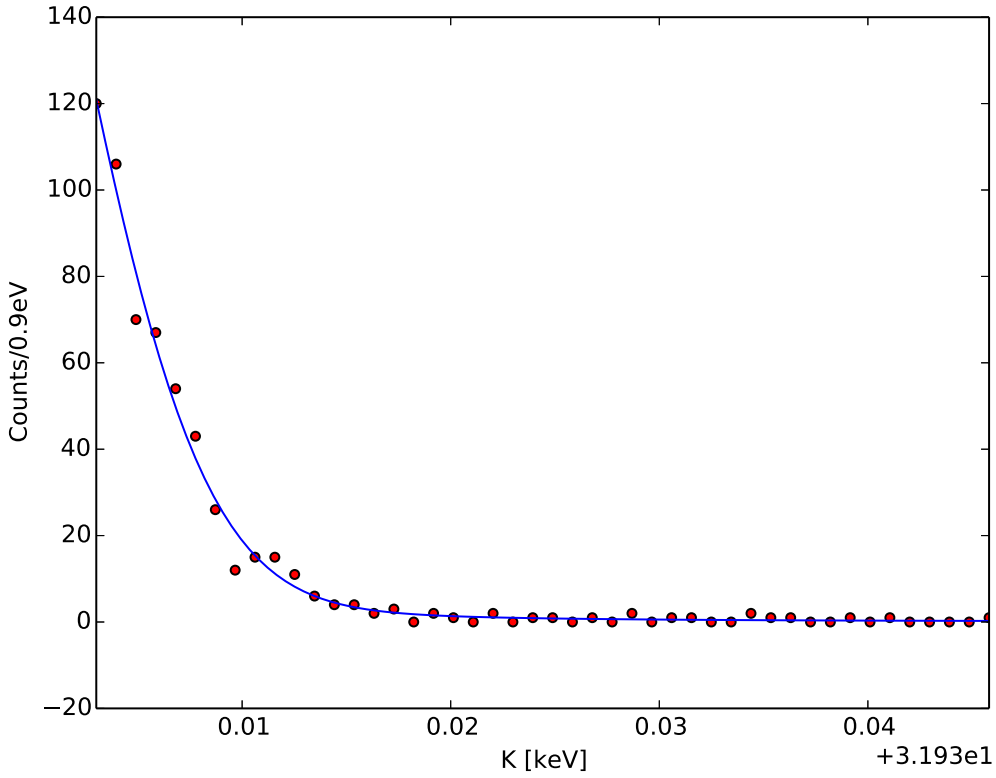

Figure 7.10: The Voigt profile fit to the high energy edge of the $M_{1,2}$ doublet is shown along with the data.

evident in the K-shell frequency spectrum (shown below), the peak-to-tail ratio is far less dramatic in the observed spectrum than it is in the predicted spectrum.

Ultimately these discrepancies must be caused by some physical effect which is not accounted for in the simulated data. Several effects have been so far considered:

- Radial field components may distort the observed spectrum by changing the initial frequency of the electron. This effect tends to lower the total field that is seen by the electron, and should move some events into the peak from the tail.

- Electrons born at large pitch angles away from $x = y = 0$ will describe a circular

Parameter	K	L_3	M_2
γ	$1.63 \pm 0.45(\text{stat})\,\text{eV}$	$0.5 \pm 0.4(\text{stat})\,\text{eV}$	$0.5 \pm 0.7(\text{stat})\,\text{eV}$
σ	$2.9 \pm 1.5(\text{stat})\,\text{eV}$	$2.0 \pm 0.6(\text{stat})\,\text{eV}$	$5.9 \pm 3.9(\text{stat})\,\text{eV}$
FWHM_L	$3.3 \pm 0.9(\text{stat})\,\text{eV}$	$1.1 \pm 0.7(\text{stat})\,\text{eV}$	$1.0 \pm 1.5(\text{stat})\,\text{eV}$
FWHM_G	$6.9 \pm 3.5(\text{stat})\,\text{eV}$	$4.7 \pm 1.5(\text{stat})\,\text{eV}$	$13.9 \pm 9.2(\text{stat})\,\text{eV}$
FWHM_V	$8.8 \pm 3.5(\text{stat})\,\text{eV}$	$5.3 \pm 1.5(\text{stat})\,\text{eV}$	$14.4 \pm 9.2(\text{stat})\,\text{eV}$
E_K	$17816 \pm 25(\text{syst}) \pm 6(\text{stat})\,\text{eV}$	$30468 \pm 25(\text{syst}) \pm 3.5(\text{stat})\,\text{eV}$	$31926 \pm 25(\text{syst}) \pm 16.9(\text{stat})\,\text{eV}$

Figure 7.11: Shown above are the tabulated results from fits to the spectral lineshape of the high energy edge of the K, L_3, and M_2 conversion electron lines. Agreement with all expected values is at the 1σ level. Full expectations can be seen in Appendix B.

path which orbits the geometric axis of the magnetic field. As the electrons move into the z-midplane of the trap, the decreasing field will tend to increase the radius of the orbit so as to conserve the total flux which is enclosed by the electron loop. As a consequence, large r electrons will be preferentially removed from the trap by collision with the wall. However, this effect is presumed to be at the 10^{-3} level, in accordance with the size of the magnetic inhomogenity and should not have a profound effect.

Further study must be done to reconcile the difference between the modeled lineshape and that which is observed.

7.3.2 The L_3 line

The reconstructed energy of the L_3 line, $30468 \pm 25(\text{syst}) \pm 3.5(\text{stat})\,\text{eV}$, is in good agreement with the previously measured value of 30 472.6 eV. The data in the high energy tail of the L_3 line exhibited an unusually high variance as compared to the K and M-shell edges, as evidenced by the narrower bin size (0.6 eV). One result of the finer binning was the resolution of more peak structure in the L-shell dataset - the edge fit clearly shows the peak maximum and some indication of the low energy structure. Notably, the error on the L_2 energy fit was the lowest among the datasets, and the gaussian contribution the smallest.

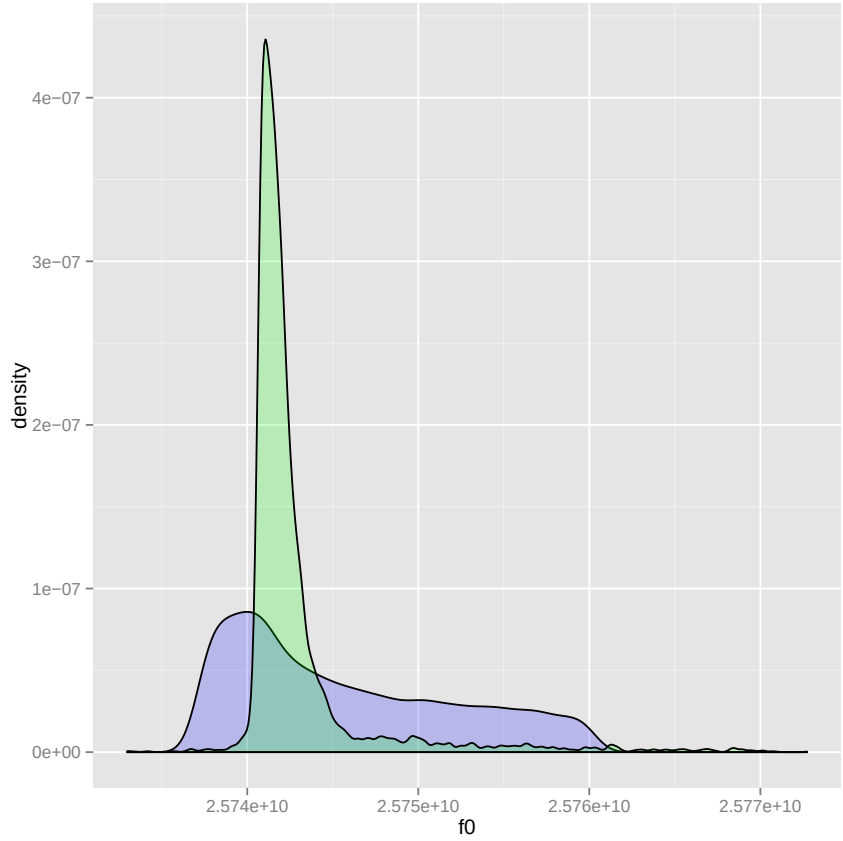

Figure 7.12: Kernel density estimates from observed data (in green) and simulated data (in blue) are shown here. Note that in particular, the heavy tail of the simulated data is not seen in the real data. In addition, the peak is much broader in simulation than in observation. Clearly there are subtleties of the motion that are not captured by the simulation.

The Lorentzian component linewidth from the fit, 1.1(7) eV is in agreement with the expected linewidth of 1.4 eV.

7.3.3 The M_3 line

The M_3 dataset presented more difficulty than the K and L-shells. While the reconstructed energy $31926 \pm 25(\text{syst}) \pm 16.9(\text{stat})$ eV is in agreement with the expected value of 31 937.3 eV, the discrepancy between the measured and expected values is the largest for

this dataset. Additionally, the statistical error is larger by almost a factor of 3 than that from the K-shell. To some extent this is expected: not only is the size of the dataset 2/3 that of the others, the intensity is shared among a larger number of spectral components. However, the M_3 line was specifically chosen as the target for fitting because of its prominence - the size of the histogram peak is on par with that from the other shells. The fit also behaved pathologically - the favored Lorentzian linewidth for some bootstrapped fits is less than zero, and in fact the best fit parameter is consistent with zero at 1σ. As a consequence it is difficult at best to trust the linewidth estimate from the fit, but it is nonetheless noted that the estimate of the Lorentzian linewidth of $1.0 \pm 1.5\,\mathrm{eV}$ is consistent with previous measurements of 1.66 eV.

7.3.4 In totality: broadening and some surprises

The underlying resolution of the detector, as measured by the FWHM of the reconstructed lines, is somewhere in the range 5.3 eV to 14.4 eV. The Lorentzian component of the lines, as measured, appears to be in agreement with the natural linewidths which are expected from the conversion electron spectrum detailed in Appendix B. Additionally, the reconstructed energy for the chosen lines is in agreement with previous measurement - although it is noteworthy that the best fit reconstructed energy of all three lines is below the expected value by several eV.

A few possible sources of line broadening (by no means an exhaustive list) are studied below, in an attempt to shed some light on what may be introducing the broad and variable Gaussian profile that is observed in addition to the Lorentzian component of the lines. However, at this point it should be noted that with our growing but fledgling understanding of the detector, the bulk of the broadening of the lines remains mysterious.

Finite observation time

The ultimate fate of a trapped electron is to scatter from gas that is in the trapping region, thereby leaving the phase space where it is trapped and disappearing from detection. This finite observation time (call it $\mathcal{T}_{\text{obs}}$) during which the electron signal may be recorded leads to a broadening of the observed signal. As calculated by Yadavalli[48] in 1963, the linewidth introduced by this finite observation time is given by

$$\delta f = \frac{k}{T_{\text{obs}}} \tag{7.2}$$

where k is determined via the autocorrelation of the (noisy) signal, and is defined as $k = \tan^{-1}(A/B)$, where A and B are the amplitudes of the $\sin()$ and $\cos()$ terms in the autocorrelation, respectively. Assuming i.i.d. noise with variance σ^2 and signal amplitude a, We can arrive at

$$\delta f = \frac{1}{\mathcal{T}_{\text{obs}}} \tan^{-1}\left(\frac{\sin(2\pi f \mathcal{T}_{\text{obs}})}{2\pi f \mathcal{T}_{\text{obs}}(\mathcal{S}+1) + \sin(2\pi f \mathcal{T}_{\text{obs}})\,\mathcal{S}}\right) \tag{7.3}$$

where $\mathcal{S}$ is defined as the r.m.s. signal-to-noise ratio $a^2/(2\sigma^2)$. If a typical value of $\mathcal{T}_{\text{obs}}$ is 100 µs, with a pessimistic time domain $\mathcal{S}$ of 1×10^{-3}, the calculated linewidth is roughly 5 Hz at a carrier frequency of 26 GHz, which corresponds to an energy width of about 1 µeV, a miniscule width that is negligible at this point.

Oscillator phase noise

The high frequency (f_o =24.2 GHz) oscillator is a phase locked dielectric resonant oscillator, and has an exceptionally low phase noise specification. The equivalent frequency space representation has a a Lorentzian FWHM of about 1 mHz, which is absurdly low compared to the precision of the energy reconstruction of Project 8 and is entirely negligible.

Track start time misidentification by binning

Because the STFT is discretized with respect to time, the exact start time of the electron track is also discretized. Unless the electron signal happens to appear precisely at a pixel

boundary, the pixel which contains the true "beginning" of the electron track will have an impoverished signal-to-noise ratio w.r.t. pixels after it due to the fact that the electron signal is only present for some fraction of the time that pixel represents. The sign of this error will always be in the direction of later identification of the first signal bin. Because the pixellation is an independent process done without regard to the signal, the true position of the beginning of the signal will be on average halfway through the first pixel in which the signal appears, and therefore a reasonable estimate of this effect is a single bin width late misidentification of the start time of the electron. If the pixels are of area $\delta f \times \delta t$, and the electron frequency is changing at a rate of $\dot{f}$, the expected frequency error in number of bins is

$$\langle \Delta f \rangle = \frac{\dot{f}}{2} \frac{\delta t}{\delta f} \tag{7.4}$$

Where the assumption has been made that the probability of a pixel exceeding the signal-to-noise threshold is proportional to the percent of time it is occupied by an electron signal. Using a frequency rate-of-change of $300\,\mathrm{MHz\,s^{-1}}$ and the pixel width $\delta f \times \delta t$ of $12.2\,\mathrm{kHz} \times 81.92\,\mu\mathrm{s}$, the expected number of bins in error is almost exactly 1.

Track start time misidentification by DBSCAN

Track identification in the time-frequency (TF) plane begins with a thresholding step in which all pixels below a certain threshold are rejected as not belonging to an electron track. However, there is a non-negligible probability for noise bins to exceed this threshold, and in the event that noise bins which are in proximity to signal bins are accepted, DBSCAN may erroneously include them as part of an electron track. Because the initial kinetic energy estimate is made by measuring the frequency of the first bin along an electron track, any error in correctly identifying this frequency propagates linearly to an error in frequency:

$$\begin{aligned} K - \delta K =& mc^2 \left(\frac{f_0}{f_c + \delta f} - 1 \right) \\ \approx& \gamma mc^2 \frac{\delta f}{f_0} \end{aligned} \tag{7.5}$$

Where terms of order $(\delta_f / f_0)^2$ and higher are extremely small corrections and have been neglected. As an example, if the size of the pixels in the TF plane is $\Delta\nu\Delta t$, then a misiden-

tification of the start pixel by a single bin for a K-shell electron corresponds to an error of 0.6 eV if $\Delta\nu = 30\,\mathrm{kHz}$.

To make this statement more precise, let us first consider the problem of misidentification when the analysis requires that bins above threshold be exactly adjacent in time and frequency. Take the position of the "true" first bin in the TF plane to be $p_0 = (t_0, f_0)$. The output from the reconstruction algorithm will be some point $\hat{p} = (t_k, f_k)$. Assume that the reconstruction algorithm has a false negative rate of exactly zero, so that p_0 is never rejected as noise. Then by design, $k < 0$, and what we seek is the distribution of $|k|$ for a given threshold so that we can calculate its moments.

The complex amplitude $a(t, f) = a\,(z_0 + iz_1)$ of a TF pixel derived from purely white noise has both real and imaginary parts drawn from i.i.d. $\mathcal{N}(0, \sigma)$. Therefore, the power in that pixel $P = |z_0 + iz_1|^2 = z_0^2 + z_1^2$ is a random variable which is distributed as a scaled χ_2^2, where the scaling factor is $\sigma^2 a^2$. Therefore, the probability to observe a pure noise bin with power P greater than some threshold $P_{\min}$ is simply a decaying exponential:

$$\mathcal{P}(P > P_{\min}) = e^{-\frac{1}{2}\frac{P}{\sigma^2 a^2}} \tag{7.6}$$

There is of course also a probability for multiple bins in a row to be noise bins which are above threshold. Because our algorithm requires adjacency, it is easy to extend this result to n bins, the probability of which is simply $\mathcal{P}^n$. The mean number of misidentified bins is therefore $\langle n \rangle = \sum_{i=1}^{\infty} n\mathcal{P}^n / \sum_{i=1}^{\infty} \mathcal{P}^n$, which is given in closed form by

$$\langle n \rangle = \frac{1}{e^{\frac{S}{2}} - 1} \tag{7.7}$$

The quantity $S = P_{\min}/(a^2\sigma^2)$ may be interpreted as a minimum signal-to-noise threshold in the presence of pure white noise. The mean number of misreconstructed noise bins as a function of this threshold is shown below in Figure 7.13.

The DBSCAN algorithm used for track reconstruction does not, in general, require that bins which are clustered together be adjacent. Instead, it requires only that bins appear

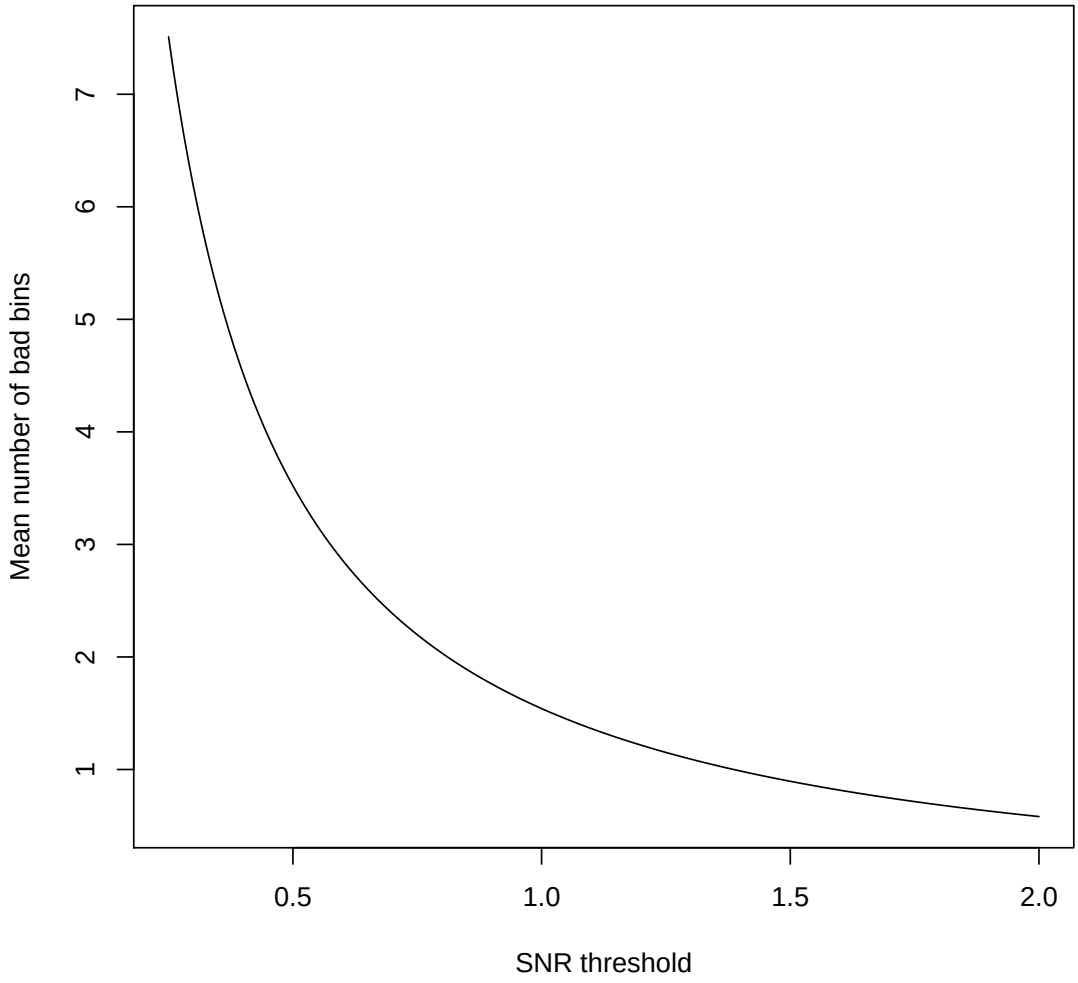

Figure 7.13: Misreconstructed number of bins vs chosen SNR threshold for adjacent bin track reconstruction.

within some distance ϵ of each other. This constraint, being more lax than exact adjacency, has somewhat worse performance with respect to including noise bins in tracks. Let us consider a case where the bins are required to be collinear, but may be separated by a distance no greater than $\epsilon = M\delta\nu$ in frequency (i.e. M pixels apart). Then the probability

that there will be at least one high bin due to noise among the M possibilities is simply the complement of the probability that none of them are high. For M bins and a signal-to-noise threshold of $\mathcal{S}$, the mean number of bins is:

$$\langle n \rangle = \left(1 - e^{-\frac{\mathcal{S}}{2}}\right)^M \left[1 - \left(1 - e^{-\frac{\mathcal{S}}{2}}\right)^M\right] \tag{7.8}$$

As shown below in Figure 7.14, there is a high probability to accept noise bins in the low signal-to-noise regime.

The SNR threshold used in the data shown below is $S = 6.5$, and the frequency radius was set to 150 kHz with an individual frequency bin width of $\delta\nu$ =12.2 kHz, which corresponds to a choice of $M = 12$. The expected mean number of noise bins is less than 1 for these parameters, so significant blurring from noisy data is not expected. However, the above analysis makes the assumption that all of the noisy data lies on a line. Because the linear reconstruction actually happens after the track clustering, it is possible for noise contamination to enter the process earlier and have an impact.

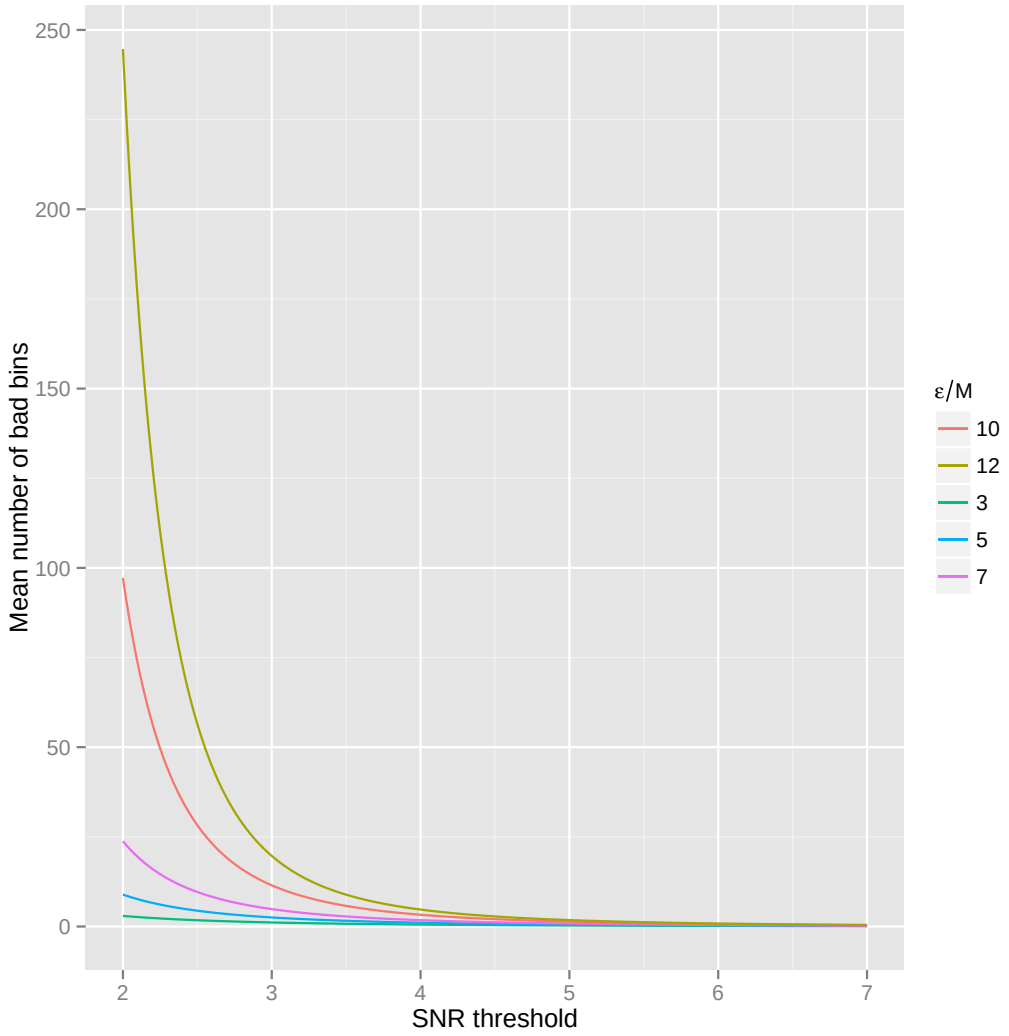

Figure 7.14: The permissive nature of a DBSCAN-type analysis is shown above for various configurations where the maximum distance from bin to bin is 3, 5, and 7 respectively. Note that for low SNR, the performance is terrible. Once the SNR has reached roughly 10, the probability to include noise bins is negligible.

Chapter 8

CONCLUDING REMARKS

The "Project 8" CRES demonstrator experiment has been a dramatic success. As a novel method for electron spectroscopy, the promise of CRES has been validated by a complete observation of the ^{83m}Kr conversion spectrum, spanning the K lines, the entire L and M series, and the N shell electrons. The resolving power of the detector, as measured by the FWHM of the reconstructed energy spectra, is at present approximately 10 eV. This is an order of magnitude larger than MAC-E spectrometers such as KATRIN, but there is ample reason for optimism that this figure could be improved to 1 eV.

8.1 Improvements in experimental design

It cannot be overemphasized that the state of the detector as described in this thesis is a prototype. Thoughtful modifications to the experimental design should yield improvements in signal-to-noise, frequency resolution, and luminosity.

8.1.1 Improving Signal to Noise Ratio

As treated in Chapter 5, the signal-to-noise ratio for electron signals is established by the input temperature to the receiver and (to a very good approximation) the performance of the first stage amplifiers in the receiver subsystem. Improvements in signal-to-noise ratio will have a dramatic impact on the achievable resolution of future CRES experiments as greater detail about the electron signals will become available.

At present, the understanding of the input noise temperature to the receiver is that there are two dominant contributions: a blackbody contribution from the waveguide components themselves, and the amplifier noise as reflected from the short and readmitted to the receiver: $T_{\text{in}} \approx bT_{\text{wg}} + aT_{\text{amp}}$, where a and b will be determined below. Because the

maximum signal-to-noise Σ which is achievable scales as the inverse of $T_{\rm in}$, reducing this temperature is an obvious target for improvement.

In the shorted configuration, the blackbody radiation from the waveguide is emitted in both directions, so that its contribution appears once directly into the input to the amplifier, and again reflected from the short but attenuated by a factor of its gain. Therefore the total contribution from the waveguide is

$$bT_{\rm wg} = T_{\rm wg} + G_{\rm wg}T_{\rm wg} = (1 + G_{\rm wg})T_{\rm wg}$$

so that $b = (1 + G_{\rm wg})$. The amplifier noise is emitted from the input of the amplifier, attenuated by the waveguide, reflected from the short, and re-attenuated, so that $a = G_{\rm wg}^2$. The maximum signal to noise achievable in the shorted configuration is therefore

$$\mathcal{S}_{\rm short} = \frac{P_c}{k\nu\left((1 + G_{\rm wg})T_{\rm wg} + G_{\rm wg}^2 T_{\rm amp}\right)} \tag{8.1}$$

If the waveguide short is replaced with a cold termination of temperature $T_{\rm term}$, the reflected amplifier noise can be eliminated completely at the cost of half of the signal power P_c. In this configuration, the maximum achievable signal-to-noise is

$$\mathcal{S}_{\rm term} = \frac{1}{2}\frac{P_c}{k\nu\left(T_{\rm term}G_{\rm wg} + T_{\rm wg}\right)} \tag{8.2}$$

Therefore, the expected improvement in SNR can be calculated by taking the ratio of these two:

$$\frac{\mathcal{S}_{\rm term}}{\mathcal{S}_{\rm short}} = \frac{1}{2}\frac{(1 + G_{\rm wg})T_{\rm wg} + G_{\rm wg}^2 T_{\rm amp}}{T_{\rm term}G_{\rm wg} + T_{\rm wg}} \tag{8.3}$$

This ratio exhibits a compex interplay between the various parameters of the model, but one limiting case is simple: if the waveguide is completely lossless, so that $G_{\rm wg} = 1$ and $T_{\rm wg} = 0$, then the requirement is simply that the terminator temperature must be less than half that of the amps: $T_{\rm term} < \frac{1}{2}T_{\rm amp}$.

In general, the ratio in Equation 8.3 is difficult to make greater than one. Unless a very low waveguide temperature can be achieved, the benefit of terminating the cell instead of shorting it will be very difficult to reap. As a consequence, the temperature of the

amplifiers and waveguide is a more sensible target for initial efforts at lowering the input noise temperature of the system, and only when they are as low as possible should the terminator be revisited[1].

8.1.2 Pitch angle reconstruction and lineshape determination

If the signal-to-noise ratio of the experiment is improved, it is possible that the axial harmonics which are present due to the z-axis motion of the electrons may be observed directly. The axial frequency of the electron should be related to its pitch angle - indeed, in the harmonic trap, the axial frequency is precisely $f_a = (2\pi)^{-1} a\beta \sin(\theta)$. Therefore, in the harmonic approximation, the factor of $\frac{1}{2}\cot^2(\theta)$ can be divided out of the observed cyclotron frequency, removing the dependence on pitch angle altogether and yielding perfect energy reconstruction.

Of course, the harmonic approximation is simply an approximation. In general, the pitch angle cannot be used to invert the relationship in the harmonic trap because as shown in Figure 6.5.2, electrons at all values of z contribute to the lineshape for a given value of θ. In fact, the lineshape which is observed (which is fit well by an exponentially modified gaussian) is dramatically different from both Monte Carlo predictions and direct transformation of the analytic calculation of the lineshape from first principles. Without this information, the inhomogeneity which is introduced by the magnetic confining potential effectively anonymizes the initial conditions of the electrons that it traps by marginalizing the observed frequency spectrum over their initial phase space configuration.

8.1.3 Magnetic bottle improvements: anything but harmonic

The broadening of the observed initial frequency spectrum can be interpreted simply as a consequence of the fact that electrons will be emitted uniformly with respect to the z-extent

[1]That said, the principle of operation of the terminator is that the distance to the termination from the decay position is a constant. If the cell or trap is lengthened significantly, the terminator should be revisited for that reason - but not as a strategy to lower the noise temperature.

of the trap, over which the magnetic field will vary by about 1%. If the bottom of the trap in which trapped electrons are initially created can be flattened out so that it is more spatially homogeneous, the resulting lineshape should be sharper.

Monte carlo studies of an alternative magnetic bottle have been performed: the bathtub trap, which consists of two short solenoids separated by a large distance and of the same field polarity as the main coil. This much flatter trapping field shows much improvement over the simple harmonic trap. However, it must be emphasized that without full dynamics simulations of trapped electrons, the relationship between the monte carlo spectrum as shown below and the observed spectrum will be unclear.

The bathtub trap

The bathtub trap is formed by two short solenoids of similar construction to the harmonic trap, albeit somewhat shorter (see Section 3.4 for details). Unlike the harmonic coil, the polarity of the trap coil fields is the same as the main coil, so that two "shoulders" are added to the main field, with a flatter region in between the two. The MC lineshape is shown below in Figure 8.1 The effect of the flat bathtub floor is dramatic on the expected lineshape. The source of the effect is illustrated in the trapped phase space as shown below in Figure 8.2. Unlike in the harmonic trap, electrons are much more likely to be born in a flat field region than in a distorted region.

The bathtub trap which is currently wound on the Project 8 demonstrator can be further flattened out by using the harmonic coil in the center to mitigate the quadratic component of the field near $z = 0$. For the as-built dimensions, this compensating current should be approximately $i_{harm} = 0.01 i_{bath}$, where i_{bath} is the current per bathtub coil.

8.1.4 Simultaneous comagnetometry

Consider the expression for kinetic energy in terms of cyclotron frequency f_c:

$$K = mc^2 \left(\frac{f_0}{f_c} - 1 \right) \tag{8.4}$$

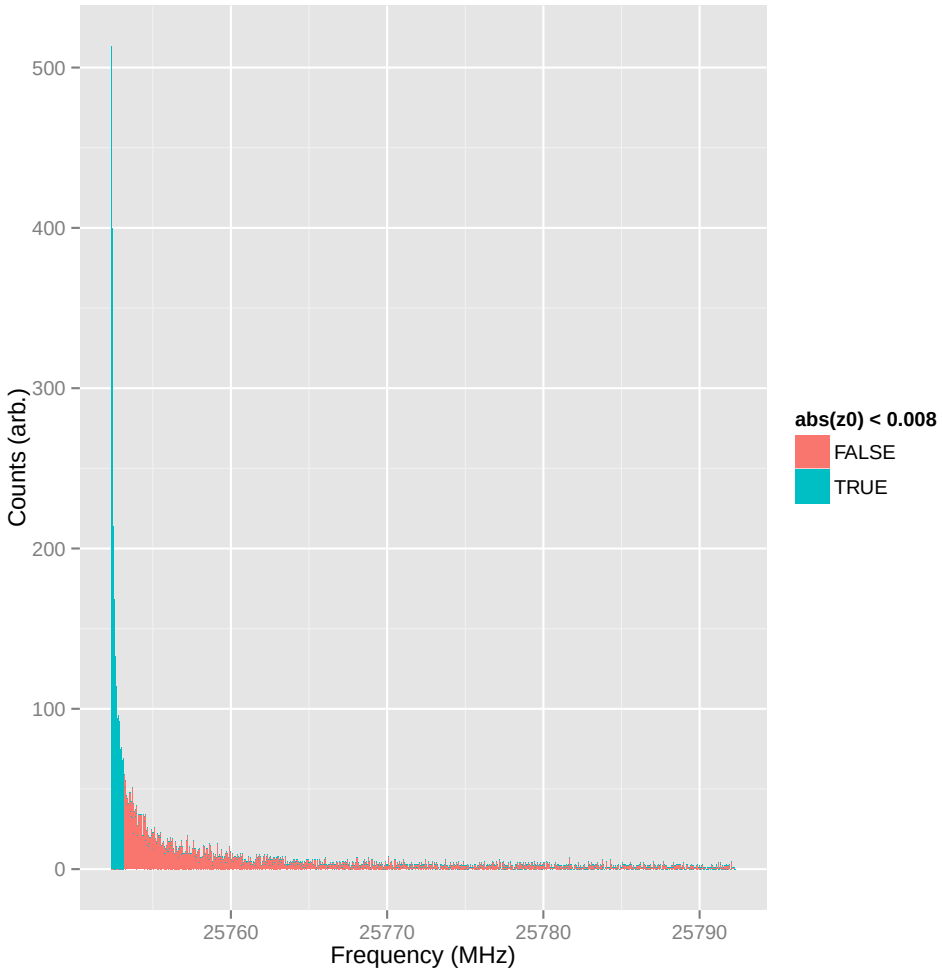

Figure 8.1: A Monte Carlo ($N = 10000$) lineshape calculation for the bathtub trap.

while this is a convenient parameterization if the magnetic field is known precisely, it may be inappropriate if in-situ measurements are unavailable or unreliable. In point of fact, f_0 - defined as the cyclotron frequency in the limit of zero energy - is but one choice of fixed points in a frequency spectrum. It is also possible to measure the energies of lines in a frequency spectrum relatively rather than absolutely. Begin with the observation that

$$\frac{f_{c,1}}{f_{c,2}} = \frac{eB}{m\gamma_1}\frac{m\gamma_2}{eB} = \frac{\gamma_2}{\gamma_1}$$

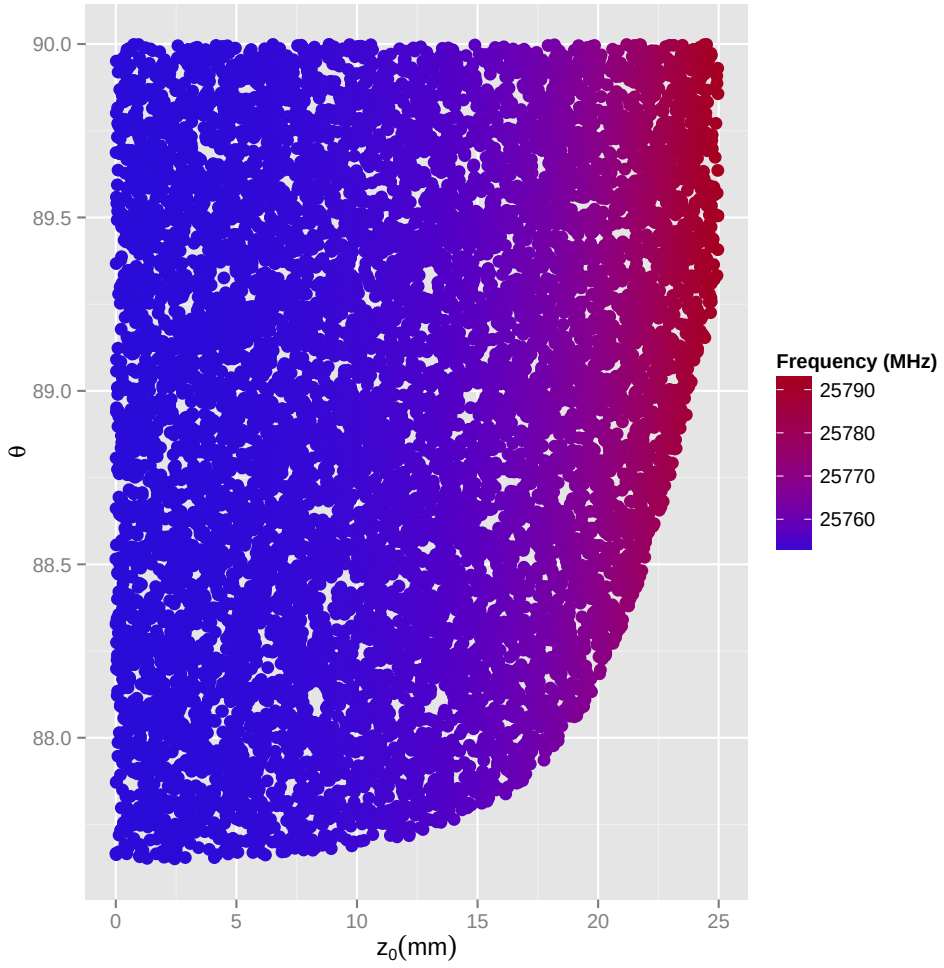

Figure 8.2: The trapped phase space in a bathtub trap.

and now, multiplying both sides by γ_1, we have

$$\gamma_2 = \gamma_1 \frac{f_{c,1}}{f_{c,2}}$$

So that by rewriting the l.h.s in terms of energy and rearranging to isolate the energy of the unknown line K_2:

$$K_2 = mc^2 \left(\gamma_1 \frac{f_{c,1}}{f_{c,2}} - 1 \right) \tag{8.5}$$

Which we can immediately recognize as a generalized version of our expression for kinetic energy in terms of cyclotron frequency, where both $f_{c,1}$ and $f_{c,2}$ are measured frequencies.

The implication of this is that if a single fixed point in the frequency spectrum is chosen and its energy is known precisely, the energy of any other point in the frequency spectrum may be inferred directly from it without recourse to the magnetic field of the experiment. Carrying this argument a little further, because of the linearity of the frequency measurements that characterize Project 8, it is possible to *simultaneously* measure two points in the frequency spectrum, and to measure the energy of one in terms of a frequency ratio.

This technique, here referred to as comagnetometry, offers a powerful alternative to direct measurements of the magnetic field. As an example, consider the following experimental setup. Two separate oscillators which are locked to a common frequency reference drive two separate but identical low frequency mixing stages. The RF input of those low frequency mixing stages should be the output from the high frequency heterodyne receiver, split so each low frequency receiver is fed an identical signal. Set the oscillator frequency of the first channel to be such that the N_{2+3} is centered in its bandwidth. The second channel can be freely adjusted to any frequency of interest, and the kinetic energy of an event in the second channel measured *without* knowledge of the magnetic field.

Such a scheme could also be used to e.g. measure the β-decay spectrum of a radioactive species which is co-resident in the gas phase with a small amount of $^{83\mathrm{m}}$Kr. Indeed, the possibilities for this technique are expansive, and may be important in reducing the dominant systematic error in the present measurement, which stems from uncertainty in the magnetic field.

Appendix A

SCATTERING

Initial assumptions about the probability that an initially trapped electron will stay trapped after a single scattering from gas were highly pessimistic. It was assumed that after a single scattering event the electron would leave the phase space in which it was trapped and become unobservable. However, differential cross section calculations for scattering of 1 keV electrons from molecular hydrogen [29] tell a different story. Even at these intermediate energies, the differential cross section is forward peaked, as shown below in Figure A

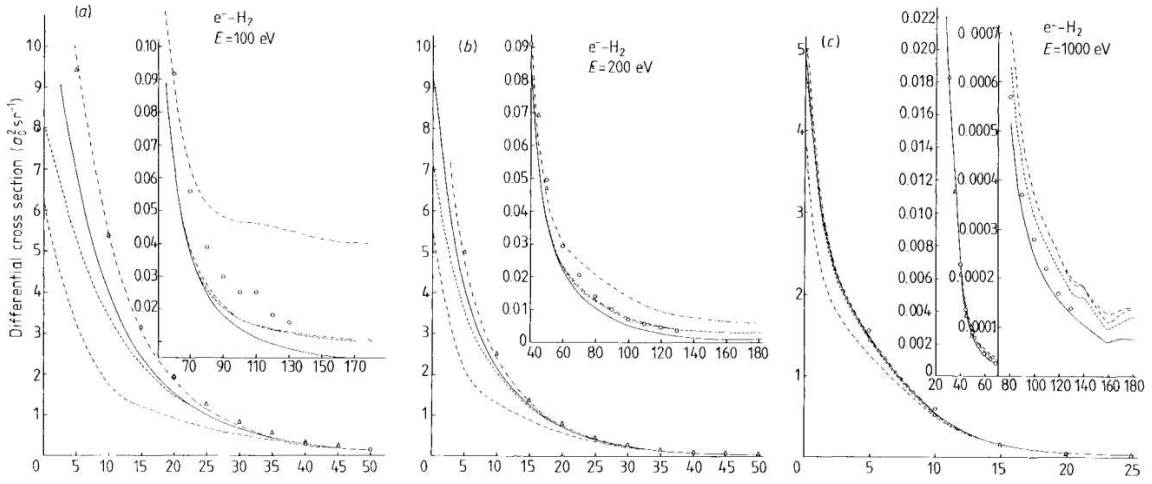

Figure A.1: The differential cross section for elastic electron scattering from the H_2 molecule at E_e =100 eV to 1000 eV. The y-axis is in units of $a_0^2 \mathrm{sr}^{-1}$, and the x axis is scattering angle in degrees [29]. Notably, the cross section "tightens up" toward very small angle scattering as electron energy increases.

The implication of the differential cross section being forward peaked is that electrons should in fact survive many scatterings from H_2 molecules before the pitch angle is changed

substantially enough to remove the electron from the trap. In addition, for higher kinetic energy the cross section is more and more peaked towards zero scattering angle - in principle this difference should be observable between the K shell and higher energy shells via the moments of the distribution that describes the number of scatterings as a function of electron energy.

The spectrogram of an electron that survives many scattering events is shown below in Figure A. Scattering events in which the final cyclotron frequency of the electron is smaller than the initial frequency are due to the fact that inelastic scattering may change both the energy and the pitch angle of a scattered electron.

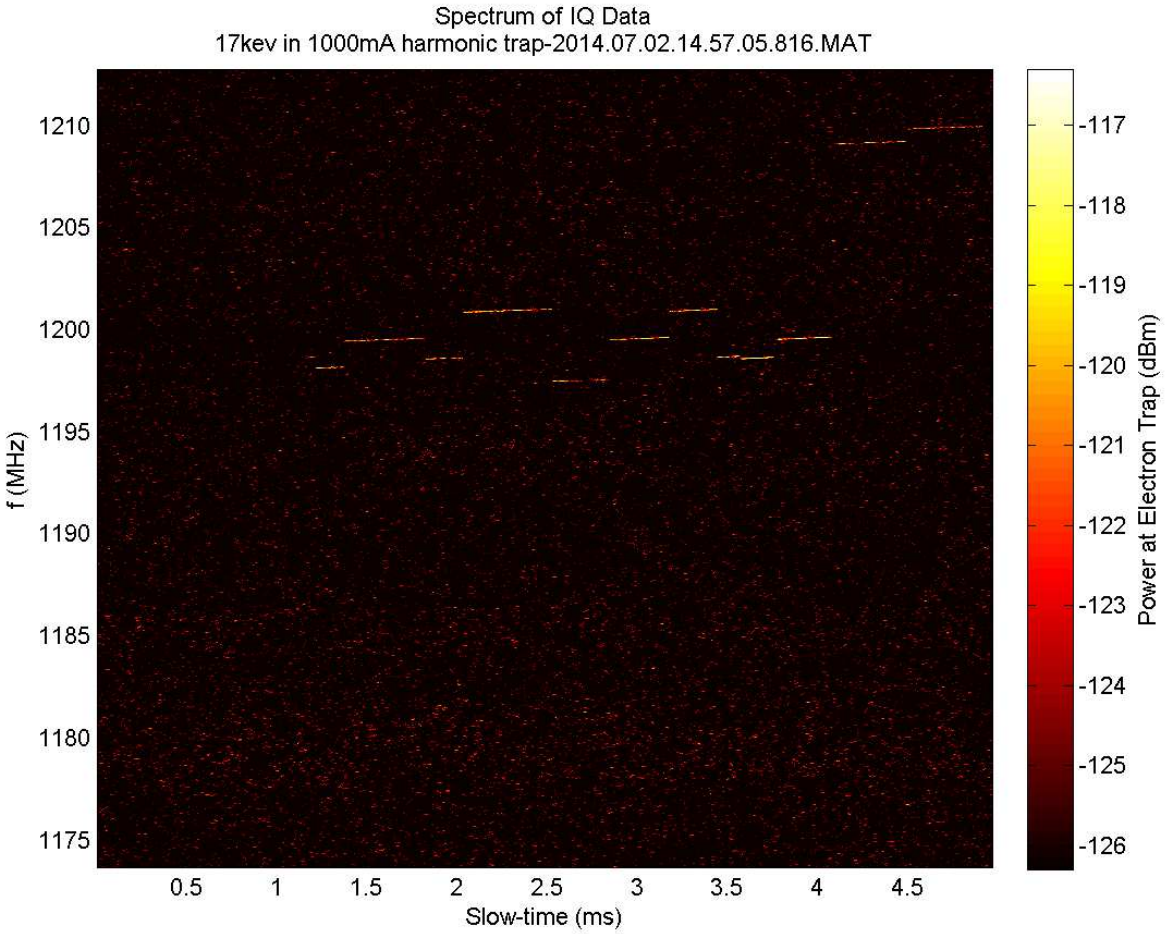

Figure A.2: The spectrogram of an electron which undergoes thirteen scatterings before leaving the trapped phase space.

Appendix B

DETAILS OF ^{83m}Kr: X-RAY BINDING ENERGIES AND CONVERSION ELECTRON SPECTRA

^{83m}Kr has been a subject of considerable study by the neutrino mass community for some time, and more recently by WIMP dark matter experiments as well, as a calibration standard. Not only is the K-shell conversion energy of 17 824.5(9) eV near the 18.6 keV β-decay endpoint of ^{3}H, but the availability of very narrow conversion lines across a broad energy range provides an excellent target for measuring the energy-dependent properties of a detector. The natural linewidth of the conversion lines is quite narrow, having a characteristic width of a few eV.

Data is tabulated below from two sources. First, Picard[5] et al. reported observation and measurement of the conversion spectrum of ^{83m}Kr using the Mainz MAC-E spectrometer. Their tabulation of the atomic binding energies and linewidths is used, along with the associated uncertainties. To calculate the expected conversion electron energy, these binding energies must be combined with the energy E_{nuc} of the ^{83m}Kr excited state. The Picard paper also contains a measurement $E_{\mathrm{nuc}} = 32151.5(11)$, but a more recent publication by Venos et al[44] contains a superior assessment of systematic error associated with the calibration sources used, and their value of E_{nuc}, 32 151.7(5) eV is used. Columns in which values are unavailable are marked with a †.

Shell	E_b	E_c (eV)	Γ_c (eV)
K	14 327.2(8) eV	17 824.5(9) eV	2.83(12) eV
L_1	1924.6(8) eV	30 227.1(9) eV	5.3(4) eV
L_2	1730.9(5) eV	30 420.8(7) eV	1.84(5) eV
L_3	1674.8(6) eV	30 476.9(8) eV	1.4(2) eV
M_1	292.8(3) eV	31 858.9(6) eV	4.27(5) eV
M_2	222.2(2) eV	31 929.5(5) eV	1.99(32) eV
M_3	214.4(2) eV	31 937.3(5) eV	1.66(8) eV
N_1	27.4(2) eV	32 124.3(5) eV	0.19(4) eV
N_2	14.65(0) eV†	32 137.1(5) eV	†
N_3	14(0) eV†	32 137.7(5) eV	†
$N_{2/3}$	14.08(0) eV†	32 137.62(5) eV	†

BIBLIOGRAPHY

[1] Material properties of kr gas.

[2] Semen Aleksandrovich Altshuler and Boris Mikhailovich Kozyrev. *Electron Paramagnetic Resonance: Transl. by Scripta Technica, inc. Transl. Ed.-Charles P. Poole.* Academic Press, 1964.

[3] VN Aseev, AI Belesev, AI Berlev, EV Geraskin, AA Golubev, NA Likhovid, VM Lobashev, AA Nozik, VS Pantuev, VI Parfenov, et al. Upper limit on the electron antineutrino mass from the troitsk experiment. *Physical Review D*, 84(11):112003, 2011.

[4] VN Aseev, AI Belesev, AI Berlev, EV Geraskin, OV Kazachenko, Yu E Kuznetsov, VM Lobashev, RP Ostroumov, NA Titov, SV Zadorozhny, et al. Energy loss of 18 kev electrons in gaseous t and quench condensed d films. *The European Physical Journal D-Atomic, Molecular, Optical and Plasma Physics*, 10(1):39–52, 2000.

[5] H Backe, H Barth, J Bonn, B Degen, L Fleischmann, JU Grooss, R Haid, A Hermann, G Kube, P Leiderer, et al. Precision measurements of the conversion electron spectrum of 83m kr. 1992.

[6] James Baker-Jarvis, Michael D Janezic, Bill Riddle, Christopher L Holloway, NG Paulter, and JE Blendell. Dielectric and conductor-loss characterization and measurements on electronic packaging materials. *NIST technical note*, (1520), 2001.

[7] Cristoforo Benvenuti and P Chiggiato. Pumping characteristics of the st707 nonevaporable getter (zr 70 v 24.6-fe 5.4 wt%). *Journal of Vacuum Science & Technology A*, 14(6):3278–3282, 1996.

[8] B Boashash. Time frequency signal analysis and processing: A comprehensive reference. 2003.

[9] Lowell S Brown and Gerald Gabrielse. Geonium theory: Physics of a single electron or ion in a penning trap. *Reviews of Modern Physics*, 58(1):233, 1986.

[10] Edgardo Browne, Richard B Firestone, and Virginia S Shirley. Table of radioactive isotopes. 1986.

[11] Bruker Spectrospin Magnet Division. *NMR Magnet System: 200 MHz, 52mm*, 1 1998.

[12] James Chadwick. Possible existence of a neutron. *Nature*, 129(3252):312, 1932.

[13] Frank Close. *Neutrino*. Oxford University Press, 2010.

[14] N Coursol, VM Gorozhankin, EA Yakushev, C Briançon, and Ts Vylov. Analysis of internal conversion coefficients. *Applied Radiation and Isotopes*, 52(3):557–567, 2000.

[15] Richard D Deslattes, Ernest G Kessler Jr, P Indelicato, L De Billy, E Lindroth, and J Anton. X-ray transition energies: new approach to a comprehensive evaluation. *Reviews of Modern Physics*, 75(1):35, 2003.

[16] L DeViveiros. Project 8 - trap scan of the 17.8 kev peak v2. September 2014.

[17] A. Domahidi, E. Chu, and S. Boyd. ECOS: An SOCP solver for embedded systems. In *European Control Conference (ECC)*, pages 3071–3076, 2013.

[18] G Drexlin, V Hannen, S Mertens, and C Weinheimer. Current direct neutrino mass experiments. *Advances in High Energy Physics*, 2013, 2013.

[19] Charles D Ellis and WA Wooster. The average energy of disintegration of radium e. *Proceedings of the Royal Society of London. Series A, Containing Papers of a Mathematical and Physical Character*, pages 109–123, 1927.

[20] Charles D Ellis and WA Wooster. The average energy of disintegration of radium e. *Proceedings of the Royal Society of London. Series A*, 117(776):109–123, 1927.

[21] Martin Ester, Hans-Peter Kriegel, Jörg Sander, and Xiaowei Xu. A density-based algorithm for discovering clusters in large spatial databases with noise. In *Kdd*, volume 96, pages 226–231, 1996.

[22] Bernard Fernandez and Georges Ripka. *Unravelling the Mystery of the Atomic Nucleus: A Sixty Year Journey 18961956*. Springer Science & Business Media, 2012.

[23] R. Flkiger, S. Y. Hariharan, R. Kntzler, H. L. Luo, F. Weiss, T. Wolf, and J. Q. Xu. *SpringerMaterials - The Landolt-Brnstein Database*.

[24] Dennis Gabor. Theory of communication. part 1: The analysis of information. *Journal of the Institution of Electrical Engineers-Part III: Radio and Communication Engineering*, 93(26):429–441, 1946.

[25] Elena Giusarma, Roland de Putter, Shirley Ho, and Olga Mena. Constraints on neutrino masses from planck and galaxy clustering data. *Physical Review D*, 88(6):063515, 2013.

[26] Maurice Goldhaber, L Grodzins, and AW Sunyar. Helicity of neutrinos. *Physical Review (US) Superseded in part by Phys. Rev. A, Phys. Rev. B: Solid State, Phys. Rev. C, and Phys. Rev. D*, 109, 1958.

[27] Oliver Heaviside. *Electromagnetic theory*, volume 3. Cosimo, Inc., 2008.

[28] John David Jackson. *Classical electrodynamics*, volume 3. Wiley New York etc., 1962.

[29] SP Khare and Kusum Lata. Elastic scattering of electrons and positrons by the helium atom and the hydrogen molecule at intermediate energies. *Journal of Physics B: Atomic and Molecular Physics*, 18(14):2941, 1985.

[30] Ch Kraus, B Bornschein, L Bornschein, J Bonn, B Flatt, A Kovalik, B Ostrick, EW Otten, JP Schall, Th Thümmler, et al. Final results from phase ii of the mainz neutrino mass search in tritium decay. *The European Physical Journal C-Particles and Fields*, 40(4):447–468, 2005.

[31] M Leber, G Rybka, and B Monreal. Project8 average power spectra. March 2012.

[32] Benjamin Monreal and Joseph A Formaggio. Relativistic cyclotron radiation detection of tritium decay electrons as a new technique for measuring the neutrino mass. *Physical Review D*, 80(5):051301, 2009.

[33] Kenzo Nakamura, Particle Data Group, et al. Review of particle physics. *Journal of Physics G: Nuclear and Particle Physics*, 37(7A):075021, 2010.

[34] Theodore G Northrop. Adiabatic charged-particle motion. *Reviews of Geophysics*, 1(3):283–304, 1963.

[35] JJ Olivero and RL Longbothum. Empirical fits to the voigt line width: a brief review. *Journal of Quantitative Spectroscopy and Radiative Transfer*, 17(2):233–236, 1977.

[36] Karle S Packard. The origin of waveguides: A case of multiple rediscovery. *IEEE Transactions on Microwave Theory and Techniques*, 32(9):961–969, 1984.

[37] W Pauli. Pauli's letter of december 1930. Technical report, CERN-ARCH-PLC Pauli letter collection: letter to Lise Meitner, 1930.

[38] David M Pozar. *Microwave engineering*. John Wiley & Sons, 2009.

[39] F Rasetti. Alternating intensities in the spectrum of nitrogen. *Nature*, 124:792–793, 1929.

[40] Lord Rayleigh. Xviii. on the passage of electric waves through tubes, or the vibrations of dielectric cylinders. *The London, Edinburgh, and Dublin Philosophical Magazine and Journal of Science*, 43(261):125–132, 1897.

[41] Metrolab Instruments S.A. *PT2025 Brochure*.

[42] P Swinbank and J Walker. The decay scheme of krypton-83. *Proceedings of the Physical Society. Section A*, 66(12):1093, 1953.

[43] Tektronix, Inc. *RSA5000 Series Datasheet*, 2015.

[44] D Vénos, O Dragoun, A Špalek, and M Vobeckỳ. Precise energy of the weak 32-kev gamma transition observed in ^{83m}Kr decay. *Nuclear Instruments and Methods in Physics Research Section A: Accelerators, Spectrometers, Detectors and Associated Equipment*, 560(2):352–359, 2006.

[45] D Vénos, A Špalek, O Lebeda, and M Fišer. ^{83m}Kr radioactive source based on ^{83}Rb trapped in cation-exchange paper or in zeolite. *Applied radiation and isotopes*, 63(3):323–327, 2005.

[46] Fred L Wilson. Fermis theory of beta decay. *American Journal of Physics*, 36(12):1150–1160, 1968.

[47] Joachim Wolf. The katrin neutrino mass experiment. *Nuclear Instruments and Methods in Physics Research Section A: Accelerators, Spectrometers, Detectors and Associated Equipment*, 623(1):442–444, 2010.

[48] SV Yadavalli. Detection of a sinusoid immersed in noise-finite integration time and linewidth. *Proceedings of the IEEE*, 51(5):865–865, 1963.